Complexity of Electron Transport in Nanoscale Molecular Junctions

Ornago, L.

DOI
10.4233/uuid:e6002163-58f0-48e1-bce2-02ac111a8adf

Publication date
2023

Document Version
Final published version

Citation (APA)
Ornago, L. (2023). *Complexity of Electron Transport in Nanoscale Molecular Junctions*. [Dissertation (TU Delft), Delft University of Technology]. https://doi.org/10.4233/uuid:e6002163-58f0-48e1-bce2-02ac111a8adf

COMPLEXITY OF ELECTRON TRANSPORT IN NANOSCALE MOLECULAR JUNCTIONS

COMPLEXITY OF ELECTRON TRANSPORT IN NANOSCALE MOLECULAR JUNCTIONS

Dissertation

for the purpose of obtaining the degree of doctor
at Delft University of Technology
by the authority of the Rector Magnificus prof. dr. ir. T.H.J.J. van der Hagen,
chair of the Board for Doctorates
to be defended publicly on
Wednesday 22 March 2023 at 12:30 o'clock

by

Luca ORNAGO

Master of Science in Materials Engineering and Nanotechnology,
Politecnico di Milano, Milan, Italy.
born in Bergamo, Italy.

This dissertation has been approved by the promotors.

Composition of the doctoral committee:

Rector Magnificus,	chairperson
Prof. dr. ir. H. S. J. van der Zant,	Delft University of Technology (promotor)
Prof. dr. F. C. Grozema,	Delft University of Technology (promotor)
Independent members:	
Prof. dr. J. M. Thijssen	Delft University of Technology
Prof. dr. C. A. Nijhuis	University of Twente
Prof. dr. I. Diéz-Peréz	King's College London, UK
Prof. dr. K. Moth-Pulsen	Chalmers University of Technology, Sweden
Dr. H. Sadeghi	Warwik University, UK
Prof. dr. Y. M. Blanter	Delft University of Technology (reserve)

Keywords: Single-molecule, Molecular electronics, Break Junction, Nanoscale Charge Transport, Molecule-Metal Interface, Nanotechnology

Printed by: Gildeprint-Enschede

Front & Back: Artistic Depiction of a nanoscale molecular junction. Image by Luca Ornago.

Delft University of Technology,
Faculty of Applied Sciences, Department of Quantum Nanoscience, van der Zant Lab

Casimir PhD Series, Delft-Leiden 2023-04

ISBN 978-90-8593-552-0

An electronic version of this dissertation is available at
http://repository.tudelft.nl/.
The associated experimental data and codes for this dissertation are available at
http://doi.org/10.4121/21725060.

To those who helped me

CONTENTS

SUMMARY

In this dissertation, we analyse the charge transport of nanoscale molecular junctions in mechanically controllable break junction (MCBJ) experiments. In particular, we focus on the characterization of molecular features going beyond the "single-peak" picture, that is, considering features in the measurements in addition to the most prominent one. To achieve this goal, we use a combination of improved experimental techniques and data analysis.

Chapter 1 introduces the field of molecular electronics. It provides a simple theoretical background to understand charge transport through metal-molecule-metal junctions. Lastly, it comments on several mechanisms that give rise to additional conductance features beyond the simple picture painted by the theoretical model.

In Ch. 2, we report the design of a low-noise logarithmic amplifier that allows to characterize molecular junctions in a greater current range. Then, we describe how machine learning based analysis can be used to classify break-junction measurements, helping in the distinction of different features in the conductance histograms.

In Ch. 3, we study a series of oligo(phenylene-ethynylene)s (OPE3s) where the central benzene ring has been replaced with acenes of increasing size. We compare their charge transport in junctions at two different scales: at the nanoscale (with the MCBJ technique), and in large-area contacts (with eutectic gallium-indium, EGaIn, measurements of self assempled monolayers, SAMs). In MCBJ, we observe a high-conductance plateau with increasing conductance value with increasing acene size. The trend corresponds to the transmission increase predicted through first-principle calculations for the sulfur-to-sulfur transport. Additionally, MCBJ measurements contain lower conductance features. In particular, the pentacene derivative exhibits low-conductance plateaus longer than the expected length of the molecule. When analysing the SAMs, we observe a similar conductance across the series of molecules, with the exception of the pentacene derivative, which exhibits suppression of conductance. We ascribe this difference to the inability of the latter molecule to form a monolayer without introducing significant intermolecular interactions.

Chapter 4 analyzes the presence of switching events in MCBJ measurements. First, we focus on OPE3 as a reference system and show that a significant fraction of the measured traces show switching behaviour for a variety of anchoring groups. Acetyl protected thiol (SAc) is an exception to this behaviour, as only a small percentage of traces displays switching when using it as an anchoring group. Furthermore, we identify two types of switching behaviour. "Plateau switching" corresponds to events in which the conductance of the junction changes between two values. "Tunnelling switching" happens after an exponential decay, at a well-defined displacement. This suggests the possibility that this behaviour originates from junctions that are formed after the rupture of the gold contact. We then turn our attention to alkane chains, for which we observe a high yield of

switching events even for SAc anchoring, hinting that conformational effects might be at play due to the flexible backbone.

In Ch. 5 we analyse the effect of side-group substitutions and torsional effects on charge transport through tolanes. We observe that the shift in frontier orbitals energy induced by electron-withdrawing or electron-donating substituents is not directly translated to changes in conductance. A novel theoretical approach was developed for first-principle calculations, which accounts for multiple contact geometries, non-equilibrium conformations, and fluctuations of energy level alignment. In this way, it is possible to more accurately predict the trends in conductance observed in the experiments.

In Ch. 6 we present the possibilities that using high-bias voltage introduces for characterizing and controlling the charge transport through molecular junctions. We apply the newly developed method to study possible quantum interference effects in macrocyclic molecules, and we present the characterization of two voltage-triggered molecular circuits. Although preliminary, these results illustrate how a voltage bias can be used as an additional tuning knob to gain more information on the charge transport of metal-molecule-metal junctions, or to control it.

Finally, in Ch. 7 we reflect on the findings reported in the dissertation, and we give an outlook on the research directions that span from them.

SAMENVATTING

In dit proefschrift analyseren we het ladingstransport van moleculaire juncties op nanoschaal in experimenten met mechanisch regelbare breekjuncties (MCBJ). In het bijzonder richten we ons op de karakterisering van moleculaire kenmerken die verder gaan dan het ënkele-piek-beeld, dat wil zeggen dat naast de meest prominente kenmerken in de metingen worden overwogen. Om dit doel te bereiken, gebruiken we een combinatie van verbeterde experimentele technieken en data-analyse.

Hoofdstuk 1 introduceert het gebied van moleculaire elektronica. Het biedt een eenvoudige theoretische achtergrond om ladingstransport door metaal-molecuul-metaal verbindingen te begrijpen. Ten slotte geeft het commentaar op verschillende mechanismen die aanleiding geven tot extra geleidingskenmerken die verder gaan dan het eenvoudige beeld dat door het theoretische model wordt geschetst.

In hoofdstuk 2 rapporteren we het ontwerp van een ruisarme logaritmische versterker die het mogelijk maakt om moleculaire overgangen in een groter stroombereik te karakteriseren. Vervolgens beschrijven we hoe analyse op basis van machine learning kan worden gebruikt om breek-junctie-metingen te classificeren, wat helpt bij het onderscheiden van verschillende kenmerken in de geleidingshistogrammen.

In hoofdstuk 3 bestuderen we een reeks oligo(fenyleen-ethynyleen)s (OPE3s) waarbij de centrale benzeenring is vervangen door acenen van toenemende grootte. We vergelijken hun ladingstransport in schakelingen op twee verschillende schalen: op nanoschaal (met de MCBJ-techniek) en in contacten met een groot oppervlak (met eutectisch gallium-indium, EGaIn, metingen van zelf-geassembleerde monolagen, SAM's). In MCBJ zien we een hooggeleidingsplateau met toenemende geleidingswaarde met toenemende aceengrootte. De trend komt overeen met de transmissietoename die wordt voorspeld door middel van eerste-principeberekeningen voor het zwavel-naar-zwaveltransport. Bovendien bevatten MCBJ-metingen lagere geleidingskenmerken. Met name het pentaceenderivaat vertoont laaggeleidende plateaus die langer zijn dan de verwachte lengte van het molecuul. Bij het analyseren van de SAM's zien we een vergelijkbare geleiding over de reeks moleculen, met uitzondering van het pentaceenderivaat, dat onderdrukking van geleiding vertoont. We schrijven dit verschil toe aan het onvermogen van het laatste molecuul om een monolaag te vormen zonder significante intermoleculaire interacties te introduceren.

Hoofdstuk 4 analyseert de aanwezigheid van schakelgebeurtenissen in MCBJ-metingen. Eerst richten we ons op OPE3 als referentiesysteem en laten we zien dat een aanzienlijk deel van de de meetreeks schakelgedrag vertoont voor verschillende verankeringsgroepen. Acetyl-beschermd thiol (SAc) is een uitzondering op dit gedrag, aangezien slechts een klein percentage van de sporen schakelen vertoont bij gebruik als verankeringsgroep. Verder onderscheiden we twee soorten schakelgedrag. "Plateau-omschakeling"komt overeen met gebeurtenissen waarbij de geleidbaarheid van het contact verandert tussen twee waarden. "Tunnelling"schakelen gebeurt na een exponentieel verval, bij een goed

gedefinieerde verplaatsing. Dit suggereert de mogelijkheid dat dit gedrag afkomstig is van knooppunten die zijn gevormd na het breken van het goudcontact. Vervolgens richten we onze aandacht op alkaanketens, waarvoor we een hoge opbrengst aan schakelgebeurtenissen waarnemen, zelfs voor SAc-verankering, wat erop wijst dat conformationele effecten een rol kunnen spelen vanwege de flexibele hoofdketen.

In hoofdstuk 5 analyseren we het effect van zijgroepsubstituties en torsie-effecten op ladingstransport door tolanen. We zien dat de verschuiving in de energie van de grensorbitalen die wordt veroorzaakt door elektronzuigend of elektronstuwend substituenten, niet direct wordt vertaald in veranderingen in geleiding. Er is een nieuwe theoretische benadering ontwikkeld voor ab-initio berekeningen, die rekening houden met meerdere contactgeometrieën, niet-evenwichtsconformaties en fluctuaties van energieniveauuitlijning. Op deze manier is het mogelijk om de trends in geleiding waargenomen in de experimenten nauwkeuriger te voorspellen.

In hoofdstuk 6 presenteren we de mogelijkheden die het gebruik van hoge voorspanning introduceert voor het karakteriseren en beheersen van het ladingstransport door moleculaire juncties. We passen de nieuw ontwikkelde methode toe om mogelijke kwantuminterferentie-effecten in macrocyclische moleculen te bestuderen, en we presenteren de karakterisering van twee door spanning getriggerde moleculaire circuits. Hoewel voorlopig, illustreren deze resultaten hoe een spanning kan worden gebruikt als een extra afstemknop om meer informatie te krijgen over het ladingstransport van metaal-molecuul-metaal junctie, of om het te regelen.

Tenslotte reflecteren we in hoofdstuk 7 op de bevindingen gerapporteerd in het proefschrift, en geven we een vooruitblik op de onderzoeksrichtingen die daaruit voortkomen.

1

INTRODUCTION

This chapter introduces the field of molecular electronics. Starting with an historical overview of the developments of the field, we briefly introduce some experimental methods used for the characterization of molecular junctions that will be relevant throughout the dissertation. Then, we introduce a simple theoretical background useful to understand charge transport through metal-molecule-metal junctions. Lastly, we discuss several mechanism that have to be considered when analysing an experimental measurement, adding complexity to the picture of nanoscale molecular junctions.

1

1.1. INTRODUCTION TO MOLECULAR ELECTRONICS

Molecular electronics is the field of science that studies electrical transport properties of molecules as individual components in circuits. The ultimate objective is to integrate them in electronic devices as, to name a few options, diodes, switches, transistors, or sensors. The first concept of molecular electronics dates back to 1956, when von Hippel [1] recognized the power of designing materials from their individual atoms to construct the functionality that is required by an engineering application. However, the modern concept of molecular electronics was born almost 20 years later, with the historical *molecular rectifier* proposed by Aviram and Ratner [2]. These authors proposed a molecular design with two units, an acceptor and a donor, separated by a tunnelling barrier. They predicted that the current of this molecule would show rectification, similarly to a traditional semiconductor p-n junction.

Experimental studies required more time to flourish, although Mann and Kuhn [3] were able to measure the conductance of a layer of fatty acids already in 1971. The interest in molecular electronics burst in the second half of the '90s. In 1995, Joachim *et al.* [4] reported on the electrical current flowing through a C_{60} molecule (more commonly known as "buckyball" or "fullerene") using a scanning tunnelling microscope (STM) tip to contact it. Two years later, Reed *et al.* [5] reported the conductance of a benzene-1,4-dithiol using the mechanically controllable break-junction (MCBJ). Other modern molecular electronics techniques began to develop in the years thereafter, following two main directions. One approach was to contact ensembles of molecules (mostly monolayers), using methods such as the formation of nanopores [6], interfacing with conducting polymers [7], or the formation of soft contacts using liquid metals (mercury, or eutectic gallium indium alloys) [8, 9]. The second strategy consisted in forming nanometric-scale contacts to connect to a limited number of molecules. Among these we remember the already cited MCBJ, the electromigrated break-junction (EMBJ) [10] and the STM break-junction (STMBJ) [11]. The latter study was of great importance for the field, as it first reported the conductance of a molecular junction as an *histogram*, not just as a single value, hinting at the intrinsic statistical nature of the formation of nanoscale molecular junctions.

Over the years, a wide variety of molecular electronic devices have been experimentally demonstrated: rectifiers [12–16], switches [17–24], sensors [25–27] and transistors [28, 29]. Molecular junctions have also been a rich source of fundamental studies. Peculiar quantum transport phenomena have been observed in molecular circuits, such as quantum interference [30–32], magnetic and spin effects [33–35], and thermoelectricity [36–38]. One can refer to Ref. [39–43] for exhaustive reviews of the achievements in the field of molecular electronics.

One of the major promises of molecular electronics has been to shrink the size of electronic components [44]. However, as time has passed, silicon technology has been able to reach dimensions comparable to individual molecules (<10 nm). It is legitimate to wonder whether there is still motivation in pursuing research in this field. However, the concept proposed by von Hippel is still applicable, and if molecules are no longer beyond the size limit of silicon technology, they are systems that can be tuned on an atomistic level through chemical synthesis to achieve functionalities that are out of reach

of traditional materials [45][1].

1.1.1. EXPERIMENTAL TECHNIQUES FOR MOLECULAR ELECTRONICS

In the previous section we mentioned several techniques that can be used to characterize the transport properties of molecules. In the following, we will briefly describe the three of them that will be mentioned in this dissertation: MCBJ, STMBJ, and eutectic gallium indium (EGaIn) measurements.

The mechanically controllable and the STM break junctions work on a very similar principle. A metallic "tip" is crushed into another metallic "lead", forming a connection. Then the two elements are pulled apart, thinning their connection. In this way, it is possible to define atomically sharp contacts [46], whose conductance is characterized by discrete values of multiples of the conductance quantum (around 77.5 μS, approximately 12.9 kΩ). After breaking this contact, if the electrodes are surrounded by molecules, they can bridge the tip and the lead, allowing to measure the current through them. In STMBJ, one electrode is the STM tip, while the other is an atomically flat substrate on which the molecules are deposited [11]. In MCBJ, both the "tip" and the "lead" are a wire of similar size [10], or they originate from the rapture a lithographically defined gold nanowire [47]. Since the MCBJ technique will be extensively used in this dissertation, we will give a more detailed description of it in Ch. 2. In both cases it is possible to measure the current continuously as the electrodes are separated, often referred to as the I(s) method, producing the so-called *breaking traces*. Additionally, they allow to perform two-terminal electrical characterization of the junction (e.g., current-voltage characteristics). The main feature of these measurements is the possibility to repeat the process thousands of times, obtaining large statistics on the junction formation.

EGaIn measurements exploit conical tips of this fluid metal to contact ensembles of molecules, in so-called "large-area" junctions. The first step of the approach is to deposit a self-assembled monolayer (SAM), i.e., a compact layer with thickness of only one molecule, on a flat gold substrate which constitutes one of the electrodes (details on how that is possible are described e.g. in Ref [48]). The second electrode is a tip of EGaIn, which is formed by depositing a droplet of EGaIn from a syringe. The latter is then raised, forming a conical connection between the needle and the droplet. Eventually, the connection breaks leaving a conical tip on the syringe needle [9]. This tip is then brought in contact with the molecular layer, allowing for electrical characterization of the current flowing through the SAM (usually in the form of current-voltage characteristics). This method allows to conduct multiple measurements on a single layer, causing little to no damage to it, and thus allows to gather a substantial statistics of formation of junctions [49]. However, this method does not allow to tune the electrode separation, as it is fixed by the thickness of the SAM.

1.1.2. THEORETICAL BACKGROUND

In this section, we will describe a simple model to understand the charge transport through molecular systems. The discussion is mainly based on Ref. [44], in which the reader can find more extensive derivations and explanations.

[1] Additionally, the transport properties of molecules are far from being well-understood, and there is still fundamental interest in researching them.

1

A molecule is characterized by a discrete set of energy levels. To each of these, a *molecular orbital* (MO) is associated, which describes the spatial wave-like behaviour of the electrons. Molecular orbitals and their energy can be calculated by solving Schrödinger equation. They are filled in order of increasing energy, according to the *Aufbau principle*. A maximum of two electrons can occupy one molecular orbital, with opposite spin, as stated by the Pauli *exclusion principle*. Lastly, Hund's rule specifies that in presence of multiple degenerate MOs, each one of them will be filled by one electron before a second electron occupies the same MO. Two particularly important orbitals for the molecular properties are the highest occupied molecular orbital (HOMO) and the lowest unoccupied molecular orbital (LUMO), which are often referred to as *frontier energy levels*[2], and their difference is known as HOMO-LUMO gap.

A scheme of the energy of the molecular orbitals and of the electrodes is shown in Figure 1.1a. Notably, in the electrodes, electrons occupy continuous bands of energy, rather than discrete values [50]. The probability of occupancy of an electron at energy E at temperature T is described by the Fermi-Dirac distribution[3]:

$$f_{\mathrm{FD}}(E,\mu,\mathrm{T}) = \frac{1}{1+e^{\frac{E-\mu}{k_B \mathrm{T}}}}, \tag{1.1}$$

where μ is the chemical potential of the electrons in the metal and k_B is the Boltzmann constant.

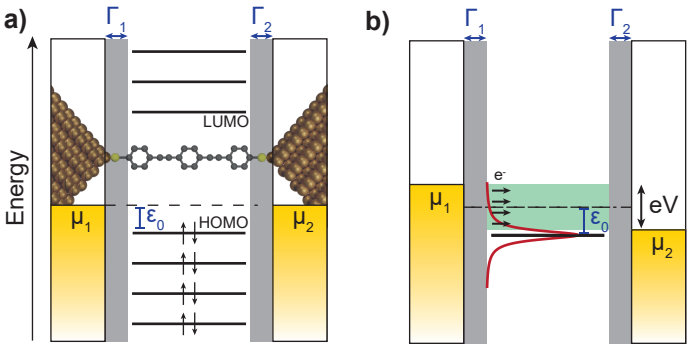

Figure 1.1: a) Schematic representation of a molecular junction, with the corresponding energy level diagram. b) Energy level diagram representing the single-level approximation.

When a molecule contacts the electrodes, the molecular orbitals hybridize with the metal, leading to significant changes of the electronic structure. More specifically, the energy levels of the molecule shift, and they are broadened by an amount proportional to the coupling strength to the metal [44, 51].

The next point is how to describe the charge flowing through a molecular junction. If the typical length scales of the system are smaller than the mean free path of electrons

[2] Often, "energy level" and "molecular orbital" are used interchangeably to indicate the state of an electron in the molecule, although the former refers to an energy value, and the latter to a orbital wave function.

[3] We will use the letter T with normal character to describe the temperature, while the italic T will be used for the transmission function.

and of the coherence length, i.e., the system is in the *quantum ballistic* transport regime, it is possible to describe transport through it with a scattering approach that yields the famous *Landauer formula* [44, 52, 53]:

$$G(E) = \frac{2e^2}{h} \sum_{n=1}^{N} T_n(E) = G_0 \sum_{n=1}^{N} T_n(E), \tag{1.2}$$

where e is the electron charge, h is the Planck constant and $G_0 = 2e^2 h^{-1}$ is the conductance quantum. $T_n(E)$, the transmission function of channel n, represents the probability that an electron with energy E passes through the scatterer. More generally, one can express the current flowing from one electrode to another, through a transmission $T(E)$, as [44]:

$$I = \frac{2e}{h} \int_{-\infty}^{+\infty} dE T(E) \left[f_{\mathrm{FD}}(\mathrm{E}, \mu_1) - f_{\mathrm{FD}}(\mathrm{E}, \mu_2) \right], \tag{1.3}$$

where $\mu_{1,2}$ are the chemical potential of the two electrodes[4]. If the bias voltage is symmetrically applied between the electrodes, the chemical potential of the electrodes can be written as:

$$\mu_1 = E_{\mathrm{F}} + eV/2, \quad \mu_2 = E_{\mathrm{F}} - eV/2, \tag{1.4}$$

where E_{F} is the Fermi energy of the electrodes. In general, the transmission function of a molecule cannot be represented by an analytical expression, and it is usually numerically calculated through a combination of density functional theory (DFT) and non-equilibrium Green's functions (NEGF) [54].

Let us consider a simple case, in which one single discrete level is coupled to the electrodes (the so-called *single-level model*, SLM). In this case, the transmission function can be expressed analytically by the Breigt-Wigner (BW) formula [44]:

$$T(E) = \frac{4\Gamma_1\Gamma_2}{(E-\epsilon)^2 + (\Gamma_1 + \Gamma_2)^2}, \tag{1.5}$$

where ϵ is approximately the energy of the single-level, and $\Gamma_{1,2}$ are related to how much the level broadens due to coupling with electrode 1,2. In the low-temperature limit, it is then possible to analytically solve the integral in Eq. 1.3 and obtain:

$$I = \frac{2e}{h} \frac{4\Gamma_1\Gamma_2}{\Gamma} \left[\arctan\left(\frac{\epsilon_0 + eV/2}{\Gamma} \right) - \arctan\left(\frac{\epsilon_0 - eV/2}{\Gamma} \right) \right], \tag{1.6}$$

where we defined $\epsilon_0 = E_{\mathrm{F}} - \epsilon$ and $\Gamma = \Gamma_1 + \Gamma_2$. It is important to mention the physical meaning of these parameters. As schematically illustrated in Fig. 1.1b, ϵ_0 represents the distance between the energy level and the Fermi energy of the electrodes and is thus called the *energy level alignment*, while $\hbar/\Gamma$ is the finite lifetime that the electrons on the molecule acquire due to the interaction with the leads. Alternatively, one can see $\Gamma_{1,2}/\hbar$ as the rates at which an electron is exchanged with electrode 1,2. Thus, the $\Gamma_{1,2}$ are often referred to as (electronic) *coupling strength*[5].

[4] We omitted the temperature from the Fermi-Dirac distribution variables to avoid confusion with the transmission. For the purpose of the chapter, it can be considered a set parameter.

[5] Not to be confused with the mechanical strength of the connection.

Figure 1.2a shows the current-voltage characteristic (the *IV*) resulting from Eq. 1.6, which displays the typical step-like shape. At low voltages ($eV \ll 2\epsilon_0$), the current is small. As the voltage approaches twice the energy level alignment ($eV \approx 2\epsilon_0$), the current sharply increases. For large voltages ($eV \gg 2\epsilon_0$), Eq. 1.6 reduces to $I = \frac{2\pi e}{h}\frac{4\Gamma_1\Gamma_2}{\Gamma}$: the current is constant and proportional to the coupling strength.

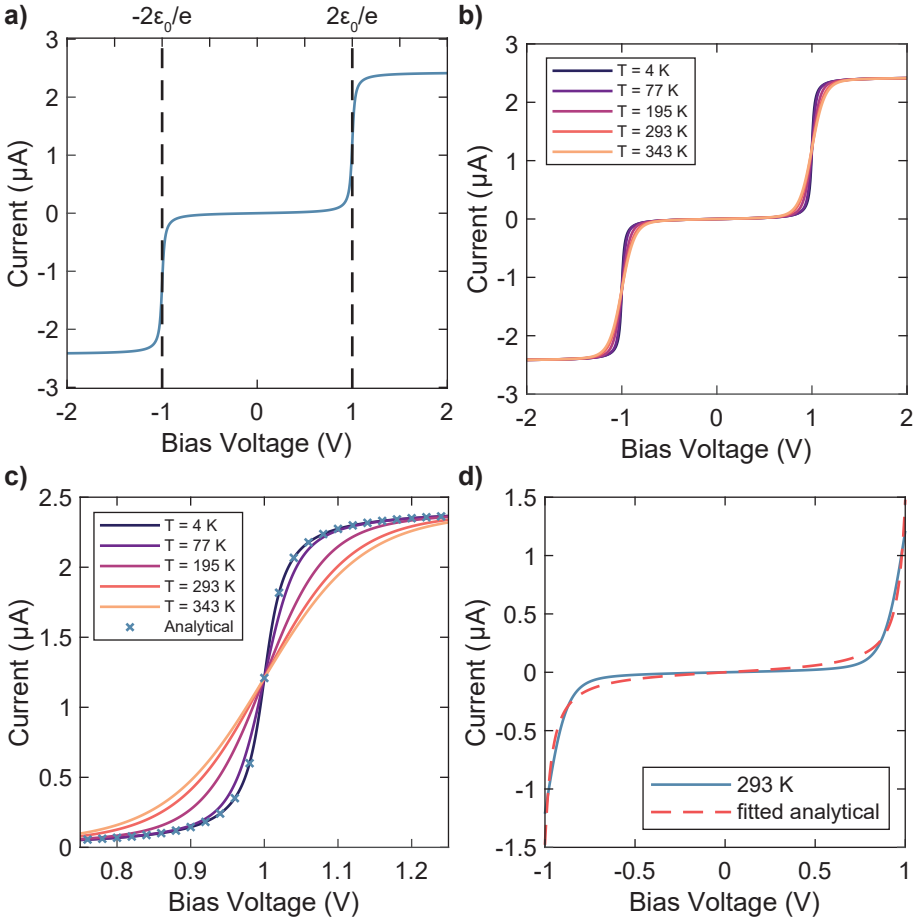

Figure 1.2: a) Current-voltage characteristic of the BW model in the low-temperature approximation, with ϵ_0 = 0.5 eV and $\Gamma_1 = \Gamma_2$ = 5 meV. b) Temperature dependence of the BW model using the same parameters. c) Zoom-in of the plot in b) showing the decrease of the slope close to resonance due to thermal broadening. d) Current-voltage characteristic calculated using ϵ_0 = 0.5 eV and $\Gamma_1 = \Gamma_2$ = 5 meV at room temperature (blue line), and one calculated using the low-temperature approximation with ϵ_0 = 0.5085 eV and $\Gamma_1 = \Gamma_2$ = 8.6 meV.

The single-level model has been shown to describe the shape of *IV*s of molecular junctions [55–57], despite the approximations that it requires. Molecules have multiples energy levels, all of which can contribute to transport. However, each one of them will give significant contribution to the current only as the voltage approaches (twice) its alignment. Typically, the HOMO-LUMO gap of molecules studied in molecular electronics

is of the order of one eV. Thus, it is difficult for several levels to contribute to the current, unless several Volts are applied betweent the electrodes. Secondly, electrons travelling through different levels can interfere with each other resulting in constructive/destructive interference in the transmission [58]. In particular, destructive interference leads to sharp anti-resonances in the transmission, which implicates that the SLM cannot correctly describe the situation. To summarize, as long as: 1) there is no significant interference between the levels, 2) one of the two frontier energy levels is closer to the Fermi energy than the other, 3) the involved level is not degenerate, and 4) the applied voltage is small with respect to the HOMO-LUMO gap, the single-level model describes the behaviour of a metal-molecule-metal junction quite well.

When fitting experimental data, the effect of temperature is often neglected, so that the analytical form of Eq. 1.6 can be used. One might question how acceptable this approximation is. Figure 1.2b shows the *IV*s calculated by numerically integrating Eq. 1.3, using the transmission of Eq. 1.5, for several temperatures. Both in the low- and high-bias regimes, the *IV*s are overlapping. However, they are different at $eV \approx 2\epsilon_0$, as it is more clearly illustrated in Fig. 1.2c. At 4 K (liquid helium temperature) the *IV* overlaps with the analytical solution. Even at 77 K (liquid nitrogen), the error committed by considering the analytical solution is small. However, as temperature increases, the current increase at $eV \approx 2\epsilon_0$ is broadened. At room temperature (293 K), this broadening is not negligible. Thus, one should not use Eq. 1.6 to fit data measured at room temperature.

However, what happens if we do so? For example, let us consider a set of data that would be described by Eq. 1.3 at room temperature, with the parameters $\epsilon_0 = 0.5$ eV and $\Gamma_1 = \Gamma_2 = 5$ meV, in the range [-1 V 1 V] (solid blue line in Figure 1.2d). The best fit of this curve using the analytical model yields the parameters $\epsilon_0 = 0.5085$ eV and $\Gamma_1 = \Gamma_2 = 8.6$ meV, leading to a 40% error in the estimation of the coupling strength (dashed red line in Figure 1.2d)[6]. In general, the error committed when using Eq. 1.6 to describe room temperature *IV*s will depend both on the exact parameters as well as on the voltage range that is considered. In particular, it is worth mentioning that in the limit $|V| \gg 2\epsilon_0/e$, one would retrieve the same parameters for the numerical solution and for Eq. 1.6, since the current saturates at the same value in both cases (assuming that the SLM still applies at these voltages).

The last step to this theoretical overview is to describe conductance histograms. The single-level model only gives one current value for each voltage, and thus the conductance would be described as a single value. However, experimental measurement are reported as histograms, often showing a log-normal peak shape [59]. Williams and Reuter [60] first tried to explain the origin of conductance histograms by applying probability theory, based on the single-level model. However, there is one difference that should be clarified before continuing. The starting point of their derivation is the transmission:

$$T(E) = \frac{4\Gamma_L\Gamma_R}{(4E-\epsilon)^2 + (\Gamma_L+\Gamma_R)^2}, \tag{1.7}$$

which seems different from Eq. 1.5. At a closer look, the two definitions are the same after the substitution $\Gamma_{L,R} = 2\Gamma_{1,2}$. In the following, we will continue using the definition of the

[6] One can notice a small difference between the two curves in Fig. 1.2d. However, that difference would not be visible in the case of real noisy data.

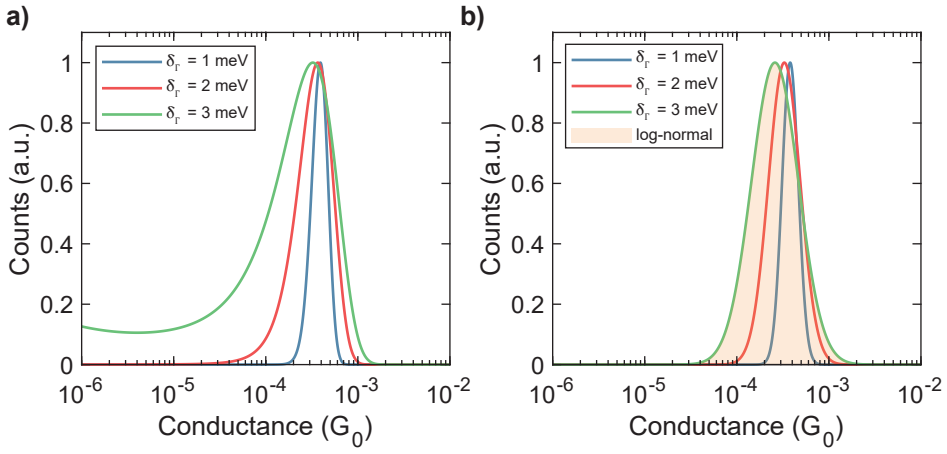

Figure 1.3: a) One-dimensional conductance histograms calculated using the analytical model form Williams & Reuter ($|E_F - \tilde{\epsilon}| = 0.5$ eV, $\tilde{\Gamma} = 10$ meV, and $\delta_\Gamma = 1$, 2, or 3 meV). b) Histograms calculated with the log-normal modified model, using the same parameters. The orange shaded area corresponds to a log-normal distribution fitted to the curve with $\delta_\Gamma = 3$ meV (green curve).

transmission as in Eq. 1.7, to be faithful to the derivations in Ref. [60]. However, the reader should remember to convert the coupling strength when comparing the two definitions of $T(E)$.

Williams and Reuter propose that the parameters in Eq. 1.7 for a molecular junction are not fixed values, but random variables, described by normal distributions. The average and standard deviations of energy level position are $\tilde{\epsilon}$ and δ_ϵ. Also, in the non-resonant tunnelling regime (i.e., $4(E_F - \tilde{\epsilon})^2 \gg (\Gamma_L + \Gamma_R)^2$), only the effective coupling $\Gamma_{eff} = \sqrt{\Gamma_L \Gamma_R}$ plays a role in the conductance, which is assumed to have a normal distribution with centre and standard deviation $\tilde{\Gamma}$ and δ_Γ. In this regime, they obtain that the histograms should have a shape described by:

$$P(g) = \frac{c}{\sqrt{8\pi g(1-g)^3}} \cdot \exp\left[-\frac{\left(c\sqrt{g} - d\sqrt{1-g}\right)^2}{2(1-g)}\right], \tag{1.8}$$

where $g = G/G_0$, $c = |E_F - \tilde{\epsilon}|/\delta_\Gamma$ and $d = \tilde{\Gamma}/\delta_\Gamma$. There are two assumptions necessary to obtain Eq. 1.8. First, since only positive Γ values make physical sense, we must have that $\tilde{\Gamma}/\delta_\Gamma \gg 0$ (in practice, the authors suggest $\tilde{\Gamma}/\delta_\Gamma > 4$). Second, it considers that any possible value in the distribution of the energy level position is far away from resonance, i.e., $|E_F - \tilde{\epsilon}| \gg \delta_\epsilon$.

While both assumptions seem physically sound, they pose strict restrictions on the width of the peak described by Eq. 1.8. To illustrate this, let us consider parameters analogous to the ones used for Fig. 1.2: $|E_F - \tilde{\epsilon}| = 0.5$ eV and $\tilde{\Gamma} = 10$ meV. Figure 1.3a displays the peaks obtained from Eq. 1.8 with the aforementioned parameters, when considering three possible values for δ_Γ, corresponding to $[c = 500\ d = 10]$, $[c = 250\ d = 5]$, and $[c = 167\ d = 3.33]$. It is clear that the peak width strongly depends on δ_Γ. More importantly, to obtain peak widths that are comparable to experiments one can get $d < 4$,

which as mentioned earlier is not physically sound. It is possible to improve on the model presented here by adding the background tunnelling current [61]. However, this is still not enough to fit experimental histograms under the restriction $d < 4$, even when classifying traces using machine learning algorithms [62].

We would like to end this discussion with a more speculative idea. One of the main limitations of the Williams and Reuter model is the assumption of a normal distribution of electrode coupling. Thus, one can think to change the distribution, for instance to a log-normal one. We apply this modification to the model in Ref. [60] and obtain:

$$P(g) = \frac{1}{4\pi\delta_\epsilon\delta_{LN}\sqrt{g\left(1-g\right)^3}} \times \int_{-\infty}^{+\infty} dE \frac{1}{\sqrt{\frac{g}{1-g}}} \exp\left[-\frac{(E-\tilde{\epsilon})^2}{2\delta_\epsilon^2} - \frac{\left(\ln\left(|E_\mathrm{F}-E|\sqrt{\frac{g}{1-g}}\right)-\tilde{\Gamma}_{LN}\right)^2}{2\delta_{LN}^2}\right], \quad (1.9)$$

where $\tilde{\Gamma}_{LN}$ and δ_{LN} are the mean and the standard deviation of the log-normal distribution respectively. We then numerically integrate Eq. 1.9, using a set of parameters comparable with the ones used for Fig. 1.3a. More precisely, we convert them as:

$$\tilde{\Gamma}_{LN} = \ln\left(\frac{\tilde{\Gamma}^2}{\sqrt{\tilde{\Gamma}^2+\delta_\Gamma^2}}\right), \quad \delta_{LN} = \sqrt{\ln\left(1+\frac{\delta_\Gamma^2}{\tilde{\Gamma}^2}\right)}. \quad (1.10)$$

The results are plotted in Fig. 1.3b. Interestingly, one retrieves an overall peak shape that is very reminiscent of a log-normal distribution (for example, see the orange area in Fig. 1.3b), a function that has been used for decades to fit break-junction histograms. The question on which distribution best describes the coupling of a real molecular junction, however, remains open, as well as the validity of the approach described above.

1.2. THE COMPLEXITY OF MOLECULAR CHARGE TRANSPORT AT THE NANOSCALE

The picture of a molecule connected to electrodes as presented in the previous section is an over-simplification of the nature of metal-molecule-metal junctions. The variability of conductance of these systems presents a richer behaviour than simply a random variation of energy level position and electrode couplings. Figure 1.4 illustrates the additional mechanisms that can contribute to the variance in conductance histograms, which will be discussed in this section. Already in 2001, Donhauser *et al.* [63] noticed that rod-like molecules undergo stochastic switching in STM measurements, likely because of conformational changes. The first observations of these fluctuations [63–65] inspired theorists to take into account different electrode geometries when calculating the conductance of molecular junctions [66]. This variability was shown to be present also in break-junction measurements, in the form of multiple peaks in the conductance histograms: a molecule binding on top of a gold atom would have a different conductance than one bound to a close-compact site [66–70], as illustrated in Fig. 1.4 (top-centre panel).

Studies on alkane chains brought a further complication of the picture: different conformers of the molecule (see Fig. 1.4, top-right panel for an example) could also cause the presence of multiple conductance peaks [71, 72]. However, break-junctions studies of conjugated molecules (that would have no conformers) also frequently showed multiple conductance peaks [73, 74], reinforcing the idea that different electrode shapes and binding configuration are at the origin of the complexity of charge transport at the nanoscale. With this picture in mind, combination of molecular dynamics simulations with transport calculations have been developed for understanding the conductance fluctuations in molecular junctions [75–79]. In particular, Li *et al.* [80] tackled the question of whether the conductance of a molecular junction would have narrow dispersion, under ideal conditions in which none of the above factors plays a role. However, these authors find that even in such a case conductance histograms have quite a large variance. They attribute the origin of the remaining variation to the mechanical manipulation during the stretching process, and to the intrinsic stochastic nature of break-junction rupture (Fig. 1.4, bottom-right panel).

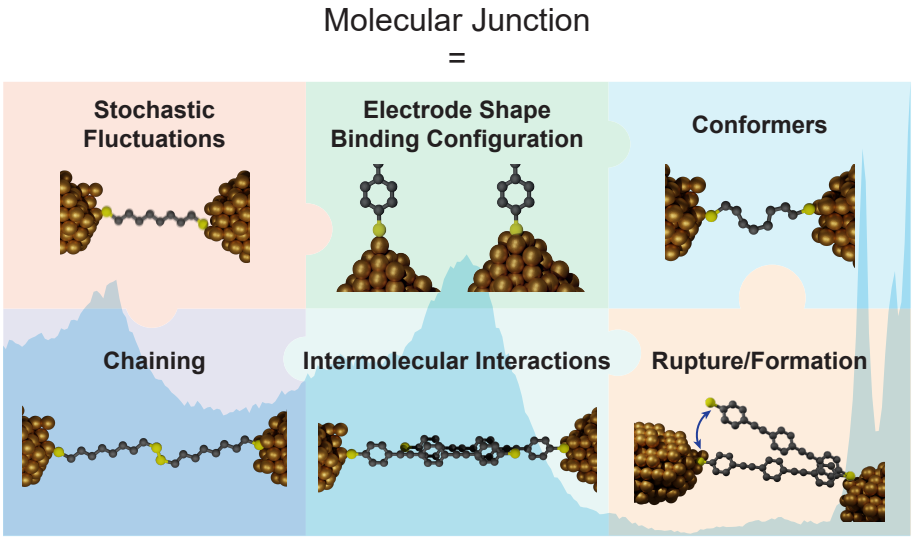

Figure 1.4: Schematic representations of the mechanisms that contribute to conductance histograms of break-junction measurements.

Intermolecular interactions are another piece that should be added to the puzzle. These are particularly relevant in conjugated molecules, in which the π orbitals of different molecules can couple "through-space", forming dimers or larger aggregates, as depicted in Fig. 1.4, bottom-centre. These π-coupled systems have been shown to produce conductance peaks in the 1D- and 2D-histograms at relatively low conductance values [81], which can also present quantum interference features [82]. The main challenge is to distinguish between charge transport through the molecular backbone ("through-bond"), and the one thorugh-space. In the aforementioned two studies, the distinction was possible because the molecules presented anchoring groups on only one side, excluding the former

mechanism. When two anchoring groups are used, through-space and through-bond effects can coexist, inducing multiple peaks in the conductance histograms [83]. Still, distinction between the two mechanism is possible through noise analysis [84]. Recently, it was suggested that the chaining of multiple molecules is also possible during a break-junction experiment [85, 86]. In this case, it is possible to identify features that have a length greater than twice the molecular length. Additionally, these first reports hint at the possibly that gold atoms are incorporated in the chain.

The advent of modern analysis methods based on machine learning enabled researchers to better classify the multitude of features that are found in break-junction measurements [87, 88]. In particular, Cabosart *et al.* [89] reported that, for a model compound like oligo(phenylene-ethynylene) (OPE3), the conductance variation between measured conductance values could be reduced by separating two types of features: shorter ones at higher conductance, and longer ones with lower conductance. Individually, these two groups of traces would report very similar conductance values across measurements, but with different yield (i.e., the amount of traces that show such feature, with respect to the total). Using a similar approach, Veen *et al.* [90] distinguished among different junction conformations in a series of alkanes chains, using the evolution of the molecular conductance as a function of stretching.

1.3. DISSERTATION OUTLINE

The complex picture of metal-molecule-metal junctions painted in the previous section, combined with the possibilities introduced by classification methods, is the context in which this dissertation starts. The main thread that will permeate through the dissertation is how we can make sense out of this complexity using the mechanically controllable break-junction technique. The reader already went through the first steps. In the previous sections of this chapter, after a brief introduction to the field of molecular electronics, we described the most simple picture, perhaps even naive, in which a molecular junction can be described: just a single-level. Then, we illustrated several mechanisms that add variance and complexity to the description of a metal-molecule-metal junction. Next, in Ch. 2, we will elaborate on the experimental and analysis methods used throughout this thesis. Then, Ch. 3 will tackle how charge transport scales from nanoscale to large-area junctions, with an eye on intermolecular interactions. In Ch. 4 we will address the presence of stochastic switching in MCBJ measurements, reporting on how it changes depending on the anchoring group and the molecular backbone. Additionally, we will hint that, in addition to the stochastic rupture of molecular junctions, one might need to also consider their formation dynamics. Chapter 5 will present the characterization of two series of tolane molecules: one exploring how substituents affect transport properties, the other exploring the effect of torsion angle. The chapter will also illustrate that, to properly predict the observed conductance trend, first-principle calculations need to take into account both different electrode configurations, non-equilibrium binding geometries and a wide range of energy level alignments. Lastly, in Ch. 6, we will discuss the possibility of characterizing molecules at high-bias to disentangle different physical phenomena. We will touch on the topic of quantum interference in macrocyclic molecular circuits, and we will consider the possibility of introducing changes in the molecule through the externally applied voltage, to induce switching in molecular junctions.

2

Experimental Techniques and Data Analysis

This chapter describes the mechanically controllable break junction (MCBJ) technique used to characterize nanoscale molecular junctions throughout the dissertation, including the characterization of a low-noise logarithmic amplifier. Then, the chapter illustrates the machine learning techniques that will be employed for the analysis of break-junction data.

2.1. MECHANICALLY CONTROLLABLE BREAK-JUNCTION

The mechanically controllable break junction (MCBJ) technique is an approach that allows to form nanoscale-sized electrodes, and to control the distance between them. This technique has been used since decades to study metallic point contacts [91] and metal-molecule-metal junctions [5]. More recently it was also proven to be a viable platform for the study of 2D-materials [92–94]. In this dissertation, the MCBJ technique was used to characterize nanoscale metal-molecule-metal junctions. This section briefly describes the working principle of the technique and the main changes that have been applied to the setup since its latest reported implementation. For a detailed description of the system used in this dissertation, see the two articles by Martin *et al.* [47, 95], as well as the PhD dissertations of Martin [96], Perrin [97], and Frisenda [98].

A scheme of the setup is shown in Fig. 2.1. The sample consists of a flexible phosphor bronze substrate, covered with a ≈6 μm layer of polyimide, with a 100 nm gold nanowire deposited on top of it (more details are presented in Sec. 2.4). The sample is mounted between two clamps in a three-point bending mechanism, which can be actuated by a stepper motor (Faulhaber), or by a piezoelectric actuator (PI-Ceramic). The stepper motor is used when a large displacement range is required, while the piezoelectric element is used for fast and precise control. As the substrate is bent, the gold nanowire increasingly streches, until it ruptures. In this way, two nanoscale-sized electrodes are formed. The geometry of the sample leads to a ratio between the vertical movement of the pushing rod and the horizontal displacement of the electrodes of the order of $5{\cdot}10^{-5}$. This allows for sub-nanometer control of the displacement between the electrodes and good mechanical stability.

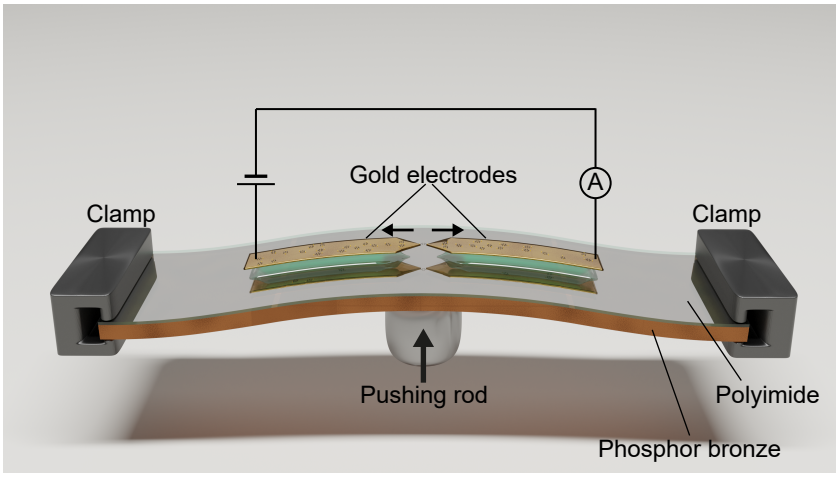

Figure 2.1: Schematic render of the mechanically controllable break junction (MCBJ) setup.

The most common measurement performed in the MCBJ technique consists of measuring the conductance of the sample at a fixed voltage bias (typically 0.1 V), while breaking and reforming the connection between the electrode. This results in a conductance versus displacement curve. The section of this curve measured during the

breaking portion of the cycle is called a "breaking trace", while the one measured during remaking of the connection is referred to as "making trace". This cycle can be repeated thousands of times consecutively. A trace starts when the electrodes are fully connected, at a conductance of 30 G_0. As the sample is bent, the conductance decreases. Below around 5 G_0 this decrease happens in discrete steps of about 1 G_0 (Fig. 2.2a), indicating the quantized nature of charge transport in the device. This step-wise decrease proceeds until a conductance of 1 G_0 is reached, corresponding to the formation of a single-atom connection [46]. Subsequently, the conductance sharply drops to values around 10^{-4} G_0 (Fig. 2.2b) because of the release of the stress accumulated during straining of the gold wire, causing a fast retraction of the electrodes' tips [99, 100]. When the electrodes displace further, the current decreases exponentially with displacement, as predicted by Simmons model [101], until the noise floor of the measurement electronics is reached. If a molecule is present, however, the current will remain constant for a range of displacement proportional to its length, producing a "molecular plateau".

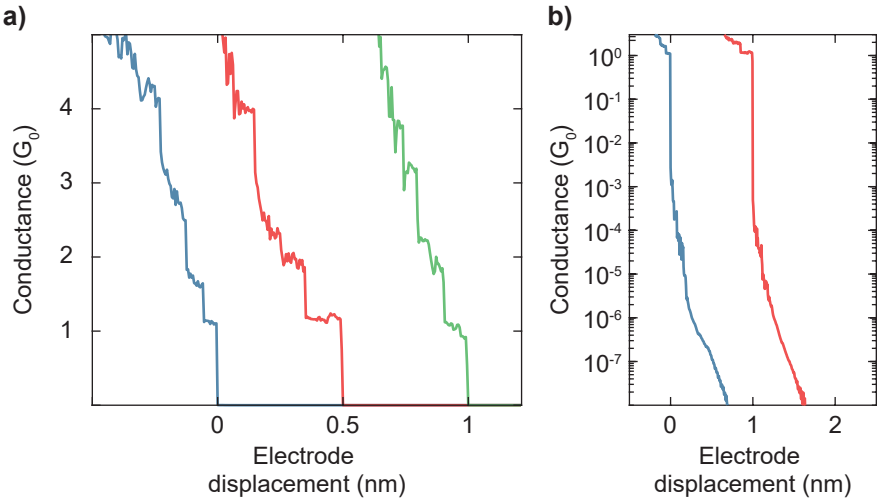

Figure 2.2: a) Examples of breaking traces showing quantized conductance steps, with a clear 1 G_0 plateau. b) Examples of breaking traces of an empty MCBJ device, showing the sharp conductance drop after rupture of the 1 G_0 plateau, followed by an exponential decay.

The first step in an MCBJ experiment consists of the characterization of the bare device, i.e., without introducing any molecule onto it. This has two purposes. On one hand, it allows to check whether the sample is clean, that is, no molecular plateau arises in the measurement. If some contamination is present, the sample is treated in an UV Ozone cleaner (Novascan PSD-UVT), as described by I.J. Olavarria Contreras [102]. Then, the characterization is repeated to ensure that the contamination was successfully removed. On the other hand, this step allows to calibrate the attenuation factor for the device, namely, to determine the ratio between the vertical displacement of the pushing rod and the separation of the electrodes (typical values are between $6{\cdot}10^{-5}$ and $8{\cdot}10^{-5}$). The procedure to do so is described in [98].

After the initial characterization, a droplet of a solution containing the desired compound is dropcast onto the device. After evaporation of the solvent, the measurement is started and thousands of consecutive traces are collected, using a fixed bias, and electrode speeds ranging from 1 to 5 nm s^{-1}. This measurement procedure is sometimes referred to as "fast-breaking".

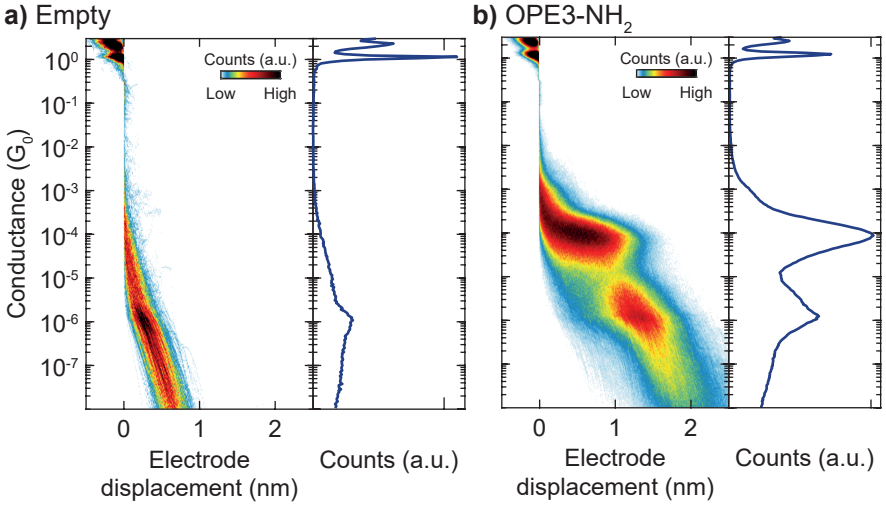

Figure 2.3: Two-dimensional conductance-displacement (left) and one-dimensional conductance histograms for a) an empty device and b) OPE3-NH_2 (see Ch. 4 for more details on the molecule).

Histograms are often employed to represent the statistical information arising from the thousands of traces collected in each measurement. The two most common types used for this purpose are one-dimensional (1D) conductance histograms and two- dimensional (2D) conductance-displacement histograms. Examples of these histograms are shown in Fig. 2.3a for an empty device, and in Fig. 2.3b for a device with OPE3-NH_2 (Oligo (phenylene ethynylene) with diamine anchoring groups, see Ch. 4 for more details on the molecule; here it serves only as an example). Notice, that for the empty device, the 1D-conductance histogram is almost featureless below 10^{-4} G_0. The corresponding 2D histogram shows counts only at short displacements, overall following the exponential trend of empty traces. The only deviation from the ideal behaviour is a small peak in the 1D-histogram at around $1{\cdot}10^{-6}$ G_0. However, there is no plateau in the 2D-histogram at the corresponding conductance, hinting that its source is not of molecular nature. The explanation of the origin of this peak can be found in Sec. 2.3.1. For now, it is enough to highlight that the lack of plateaus corresponding to the peak makes it trivial to distinguish between empty and molecular traces. In contrast with the empty device, in the 2D histogram of Fig. 2.3b there are counts at much greater displacements, and the high-count area defines a more or less flat region. This reflects the presence of a molecular plateau. Corresponding to this area, a prominent peak emerges in the 1D histogram, which approximately follows a Gaussian distribution when the histogram is binned in logarithmic scale. Hence, the peak is typically fitted with a Gaussian [59]:

$$N(g) = A \cdot e^{-\frac{(g-g_c)^2}{2w_g^2}} \tag{2.1}$$

where g is the base 10 logarithm of the conductance in G_0 units ($g = logG$). When considering the linear scale, this defines a log-normal distribution [59]:

$$N(G) \propto \frac{1}{G} e^{-\frac{(logG-g_c)^2}{2w_g^2}} \tag{2.2}$$

The centre of the distribution in Eq. 2.1 (g_c) defines the most-probable conductance of the molecule. This value is used to characterise different molecules and compare them. Throughout this dissertation, the most-probable conductance will often be referred to in short as the "conductance" of the molecule. The width of the peak (w_g) is also an useful parameter to characterise the behaviour of the molecule, allowing to discern between well-defined flat plateaus and slanted or ill-defined ones.

2.2. MACHINE LEARNING FOR DATA ANALYSIS

The analysis and interpretation of break-junction measurements is often not as straightforward as described in the previous section. In many cases, more than one plateau is present (a scrupulous reader might already have noticed it in Fig. 2.3b). For instance, alkanes [71, 72, 80, 90] and OPE3s [89, 103–106] are notorious for showing multiple conductance plateaus. As a further example, chaining of multiple units is possible in case the molecule bond to the surface is strong enough [85, 86], leading to multiple steps in molecular traces.

A modern approach of tackling this problem is to use machine learning to classify the datasets measured with mechanical break-junctions. These algorithms can be broadly classified[1] as "supervised" or "unsupervised" [107]. Supervised learning consists in training the algorithm on a labelled set of data, i.e., data whose output is already known. This approach has been applied to break-junction data to separate traces coming from different molecules in a dataset measured from a solution containing two different compounds and to track the presence of different conformers in a solution over time [108]. Although very accurate, this approach is hindered by the requirement of a set with known labels, which is seldom the case in molecular-scale electronics.

Unsupervised learning, instead, aims at extracting useful information from a set of data based only on its properties. The typical problem in this category is clustering, i.e., the classification of a set of data in subsets, called clusters, such that any element in the dataset belongs to one of them, and one only [109]. This approach gained great success in the molecular electronics community to classify break-junction data [87–89, 110, 111].

2.2.1. CLUSTERING ANALYSIS FOR THE CLASSIFICATION OF MCBJ TRACES

The typical clustering process consists of two main steps (Fig. 2.4). Firstly, the elements of the unclassified set need to be converted to points in a M-dimensional space, known as the "feature space". Secondly, a clustering algorithm is used to classify the points in

[1] There is also the "reinforced" category. However, it is not discussed here as it is not useful for the classification of break-junction data.

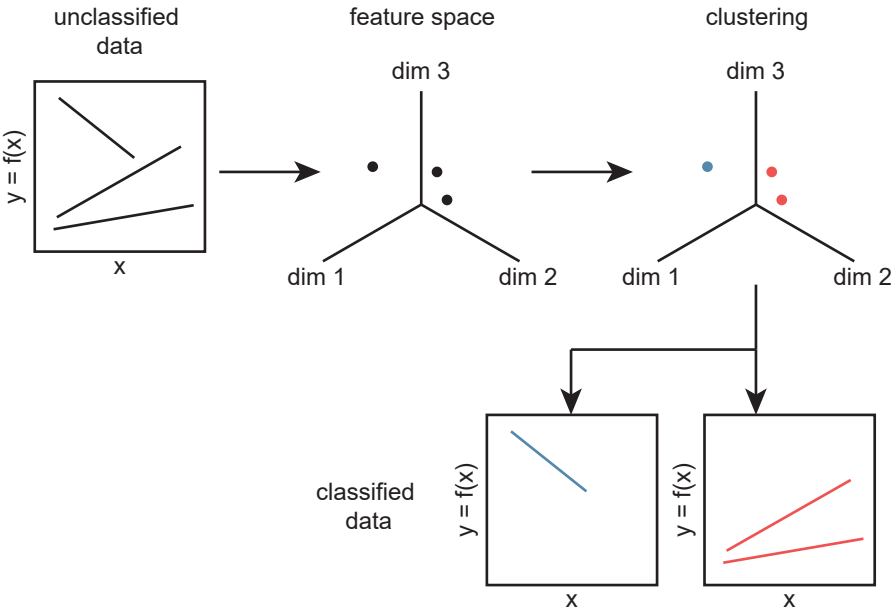

Figure 2.4: Typical flowchart for clustering of a dataset. The data is converted into points in the feature space. Then, a clustering algoritm is used to classify them. Lastly, the data can be divided into groups corresponding to the clusters identified in the previous step.

different groups. Lastly, the original elements are split according to such separation. The main differences between different clustering approaches are either in the preparation of the feature space, or in the clustering algorithm that is employed [88].

One of the first successful approaches to break-junction data classification was proposed by Lemmer *et al.* [87]. It considers every trace as a vector, and then computes their distance, the angle, and the Hamming distance[2] with respect to a reference one, defining a three dimensional feature space. In this case, a trace showing the exponential decay of an empty junction was chosen as reference. However, this process introduces one additional degree of freedom (the reference vector) that can change the outcome of the classification. For this reason, Cabosart *et al.* [89] developed an alternative approach. Their method considers the 2D histogram of each trace as the element that needs to be classified. Then, the *k-means*++ algorithm is used to cluster the dataset. As this approach has been used throughout this dissertation, it is instructive to discuss the working principle of this algorithm.

First, let us describe the working principle of *k-means*. The goal of the algorithm is to find the partition of the data which minimizes the within-cluster variance [113]. The procedure starts by defining the number of clusters k, which is set by the user. The centers of the clusters are then initialized, for instance by randomly choosing k points within the dataset [113]. Then, the following two steps are repeated until convergence [114]:

[2] The Hamming distance of two vectors is the number of components at which the two are different [112].

- *assignment step*: assign each point to the cluster that has the closest centre;
- *update step*: the new cluster centres are computed as the average of the observations in each cluster;

In general, it is not guaranteed that this procedure converges to the global minimum, and thus the algorithm has to be repeated several times to avoid local minima [113]. The *k-means*++ algorithm differs from *k-means* in its initialization, resulting in improvements in both accuracy and speed of the algorithm [115]. The modified procedure works as follows.

1. Choose the first cluster center c_1 uniformly at random within the dataset X.
2. Choose the next centre within the dataset, weighting each point by the distance from the closest of previously chosen centers. Formally, if $D(x)$ is the distance of point x from the closest (already chosen) centre, the probability of choosing x' as the next cluster centre is $\frac{D(x')^2}{\sum_{x \in X} D(x)^2}$.
3. Repeat step 2 until k cluster centres are chosen.
4. Proceed as in the standard *k-means* algorithm.

The next issue to tackle is the evaluation of the clustering results, and more specifically, the choice of the number of clusters. In fact, several algorithms, including *k-means*, require it as an input. So far, the problem has been mainly tackled by using Clustering Validation Indexes (CVIs) [116]. These are scalar values that evaluate a clustering classification either based on the comparison with a correct partition, or on the their compactness and separation. The second category is more appropriate for break-junction data, as there is no correct separation known *a priori*. For example Lin *et al.* [111] used a few indexes to evaluate the performance for clustering based on 1D histograms of the traces split with the spectral clustering algorithm. On a set of simulated data, they found that only the Calinski-Harabasz index would retrieve the correct number of clusters. However, as noted by the authors themselves, real data is more complex than a simulated set of data. A more systematic approach was proposed by El Abbassi *et al.* [88], in which 29 CVIs are computed for the classification, and the "best" result is defined as the one scoring the optimum for the most CVIs. The latter approach is promising to evaluate clustering of break-junction data. Lastly, it is important to remember that: (i) CVIs performance is lower when noise and cluster overlap are present [109], which is generally the case in break-junction data; (ii) it is not generally true that all clusters generated by the algorithm bear useful or physical information, thus even the "best" classification according to CVIs might still hide useful information.

In this last paragraph, the workflow used for clustering in this dissertation is described, exemplifying some of the issues described above. As mentioned, it is based on the approach by Cabosart *et al.* [89]. The first step is to create a 2D histogram for each trace. The parameters used to build these histograms are one of the most critical settings for obtaining a good clustering separation. The exact values for each study in this dissertation will be reported in the corresponding chapter. Then, each row in the histogram is appended to the previous one, forming an high-dimensional vector. The set of vectors built for all

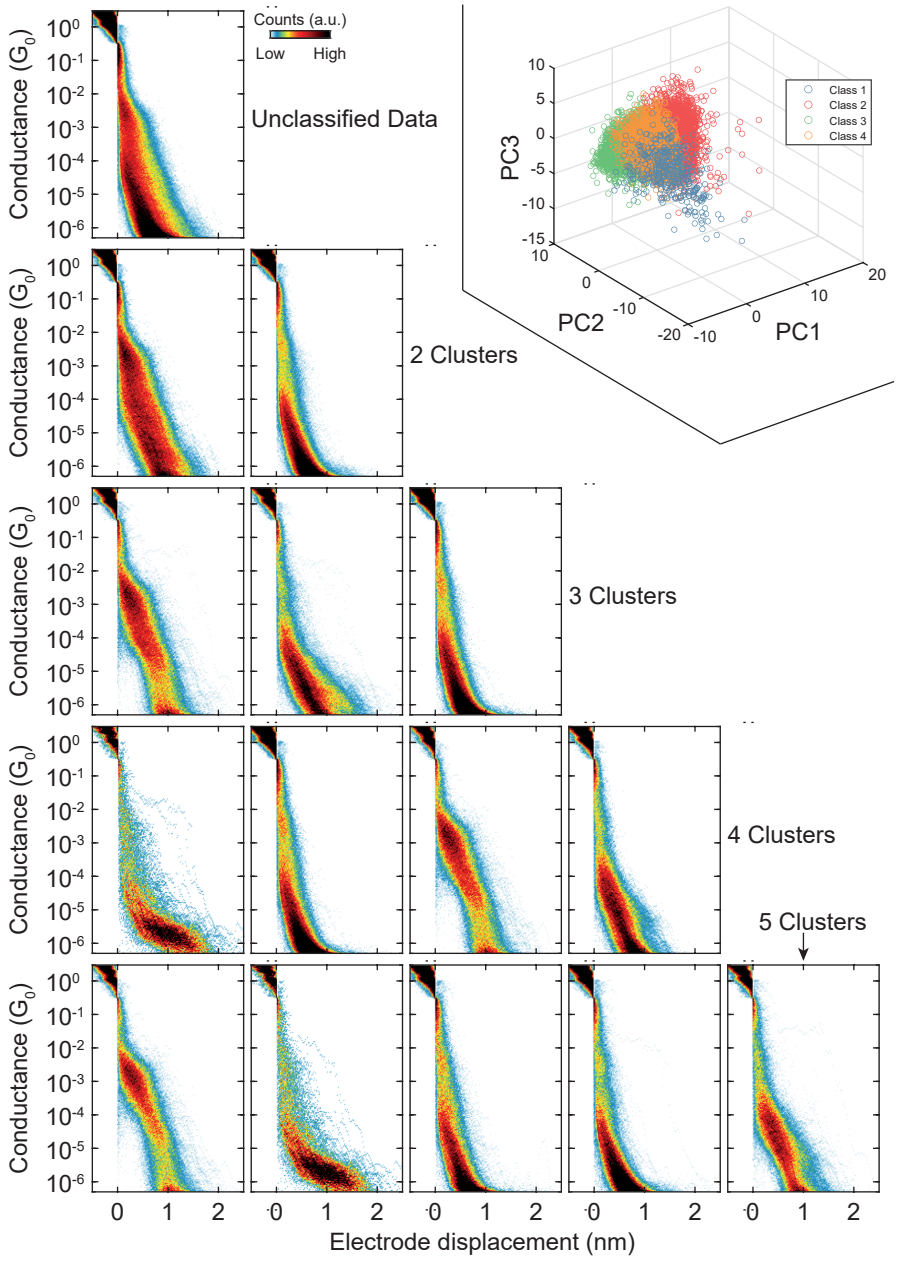

Figure 2.5: Two-dimensional conductance-displacement histograms built from an unclassified measurement of OPE2-SAc (see Ch. 5), and for the clusters obtained by splitting it in 2 to 6 total classes. The inset shows a representation of the feature space built using principal component analysis.

traces is then split using *k-means*++. Lastly, histograms corresponding to each cluster are generated. As explained above, this procedure is repeated for several total number of clusters. Figure 2.5 shows an example of the 2D histograms resulting from an OPE2-SAc measurement (see Ch. 5). Differently from Fig. 2.3, there is not a clear plateau visible in the unclassified data. Splitting the dataset in 2 allows to separate most of the empty traces, but still does not yield any plateau. Only with 4 clusters a plateau at $\approx 10^{-3} G_0$ and one at $\approx 10^{-6} G_0$ become visible. The other two clusters contain mostly empty traces, but the last one seem to hide even a different behaviour. In fact, when splitting in 5 clusters, an additional slanted plateau at $\approx 10^{-5} G_0$ is isolated. In this case, we obtain 3 clusters containing molecular plateaus and 2 having empty traces. It makes sense to group the latter in just one plot, and to reference them as a single one. A similar approach will be often used throughout the dissertation, in particular when dealing with clusters showing empty traces. The following nomenclature will be used to avoid confusion: "cluster" refers to the group of traces as identified by a clustering algorithm; "class" is a group of traces showing the same behaviour. For example, the five-fold classification in Fig. 2.5 has 5 clusters, and 4 classes (3 showing molecular plateaus, and 1 with empty traces).

2.2.2. SUPERVISED LEARNING STRATEGIES FOR EMPTY TRACE DETECTION

Isolating molecular traces in a break-junction measurement is a crucial step in the analysis of the acquired datasets. In fact, the presence of empty traces with exponential decay can influence both the position and shape of the conductance histograms [117]. Although one can correct for this effect by subtracting the background signal [59], or by adding its contribution to the fitting functions [61], it is desirable to exclude the presence of such traces all together. It is possible to use simple criteria, such as considering the fact that empty traces have a lower number of counts in the measurement range with respect to traces showing a plateau [118]. However, this does not always lead to a very accurate classification. Alternatively, neural network based classification can be used for the task. A few network designs have been reported in literature, showing promising accuracy [119, 120].

In the following, a neural network structure for the classification between empty and molecular MCBJ traces is described. This is based on the work in the MSc thesis of van Veen [121], where it is possible to find an in-depth description of the network design, training process, and validation of the classification results. The first step is to define the input of the neural network. Analogously to the clustering analysis, a combination of the 2D- and the 1D-histogram is chosen. The 2D-histogram of the trace is computed in the range -0.5 to 3 nm in displacement and -0.5 to -6 $\log(G/G_0)$ in conductance, using a 25×32 bins grid. The 1D-histograms is calculated using 100 bins and 1 to -6 $\log(G/G_0)$ limits. In total, this procedure yields a 900 dimensional input for the neural network. The network structure consists of a fully connected network with an input layer of 900 nodes, matching the input. Then, two hidden layers are present: the first with 128 nodes, the second with 64 nodes. Lastly, a 2 nodes output layer is used, representing the desired classification in "empty" and "molecular" traces. The network was trained using a set of around 200.000 pre-classified traces, containing similar amounts of empty and molecular traces. For this purpose, a set of alkanes of different lengths (propane, hexane, and octane) was used, as these molecules show plateaus at different lengths and conductance values,

as well as traces containing multiple steps [90]. A 4:1 validation ratio is used during the training process. The complete description of the neural network, its training, and its validation will be further discussed in an upcoming publication.

2.3. LOW-NOISE LOGARITHMIC AMPLIFIER

This section describes the design and implementation of a logarithmic transconductance amplifier[3] that was added to the MCBJ setup, modifying the one reported by Martin *et al.* [47, 95, 96]. The main goals of this upgrade were to enhance the detection limit and to lower the noise of the electronics, and to decrease its response time. These was achieved by moving from the amplifier from a module in the rack[4], to a printed circuit board (PCB) located close to the sample. For this reason we will refer to this electronic device as "PCB-amplifier".

The circuit diagram of the PCB-amplifier is presented in Fig. 2.6. The voltage bias (with respect to ground) is provided on the left, where it is divided by half by a voltage divider (R12 and R15). Thus, the provided bias has to be twice the desired voltage at the junction. From now on, when referring to "bias", we will refer to the voltage drop at the junction[5]. The voltage source will apply twice that value in order to achieve the desired bias. Then, a multiplexer (MUX V-source) allows to apply it to one of 8 channels. Three calibration resistors (R10, R11, R14, with resistances of 1 kΩ, 10 MΩ, and 10 GΩ) are placed in channels 0, 1, and 2. Channel 3 is empty, and channels 4 to 7 direct the bias to a junction on the MCBJ sample. Each channel has a 1 MΩ resistor connected in parallel to it, before the load (R16 to R23). The combination of these resistors with the voltage divider allows to avoid large fluctuations of the load, as seen by the bias source. This is critical, as in a typical MCBJ measurement the resistance of the junction can change from 1 k Ω to 1 TΩ in less than a second. With this scheme, the voltage source experiences a change in load impedance from ≈400 Ω to only ≈440 Ω for the same fluctuation of junction resistance.

After the sample/load resistor, the circuit has a second multiplexer (MUX I-meas) that allows to select the channel to which the amplification circuit is connected. The latter consists of an operational amplifier (82VD LMC6081AIM, Texas Instruments), to which a negative feedback is provided by two sets of diodes (BAS416, Nexperia). These are connected in opposite polarities, and they are responsible for the logarithmic current-to-voltage conversion [122].

The connection between the PCB-amplifier and the setup is realised through a ribbon cable, which is then wired to a rack-mounted matrix of MCX connectors (Matrix Module). The latter allows for the modular connection to the rest of the measurement electronics. The measurement is controlled by an ADwin Gold II (Jäger Computergesteuerte Messtechnik GmbH), connected to a computer through Ethernet. This unit combines a real-time processor with analog and digital inputs and outputs. The 16 bits digital-to-analog converter (DAC) has a ±10 V range, and it is used to control the bias applied to the junction. The 18 bits analog-to-digital converter is used to measure the output

[3] Design and fabrication of the amplifier were performed by Hans van der Does (TU Delft DEMO) and Raymond Schouten (TU Delft). Further support was provided by Berend Otto (TU Delft DEMO).

[4] IVVI-rack, home-made module based measurement unit, developed by Raymond Schouten, TU Delft

[5] This is not a proper assumption for resistances close to the series resistance, as explained later in the section.

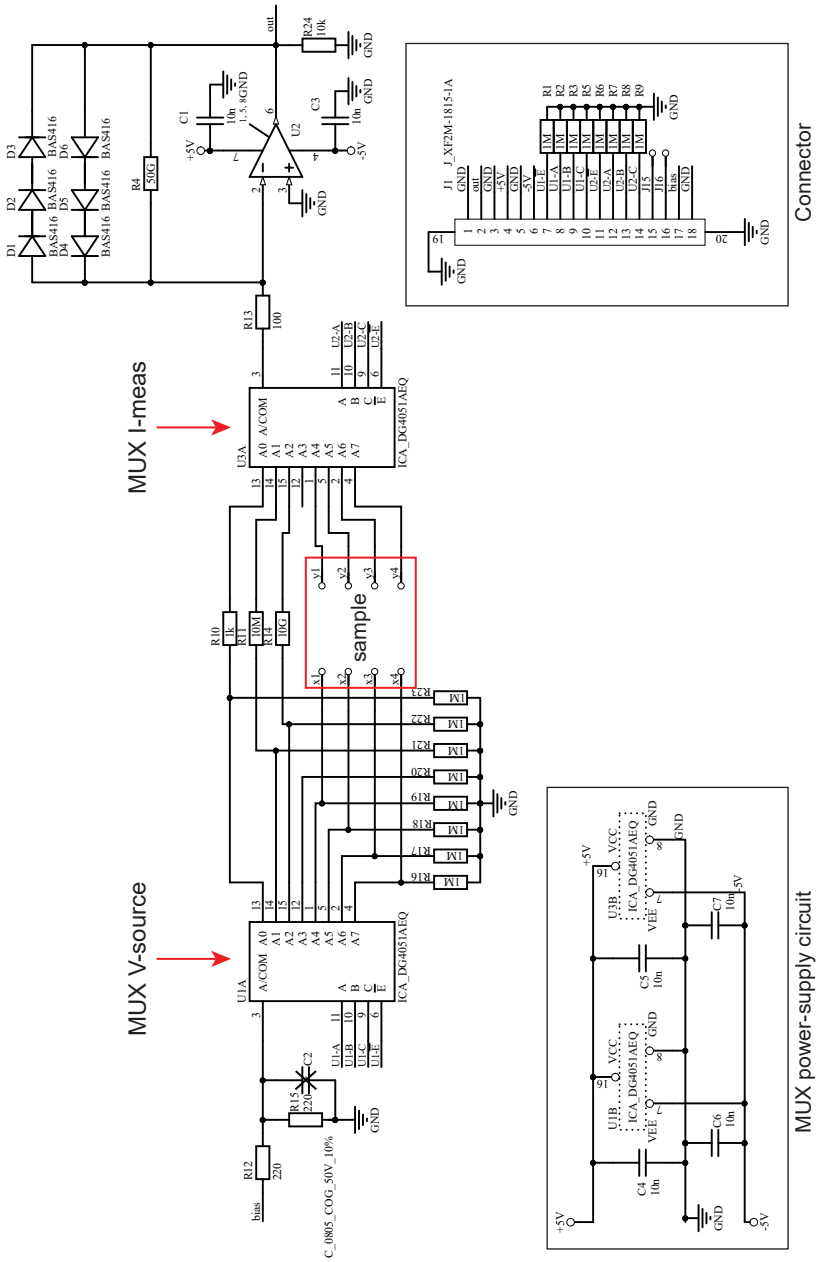

Figure 2.6: Circuit diagram of the PCB logarithmic amplifier, with the multiplexers (MUX) to switch among junctions on the sample, or calibration resistors on the board. The two insets illustrate the circuit diagram of the connector on the PCB, and of the power-supply section of the multiplexers. The serial number of the U2 op-amp is 82VD LMC6081AIM (Texas Instruments). Capacitor C2 was not mounted in the final PCB design. Adapted from the circuit diagram drawing by Hans van der Does (TU-DELFT-DEMO).

of the amplifier. It operates in the range ±2.5 V, with a maximum theoretical sampling rate of 500 kHz (in practice, if the measurement routine is complex, this is reduced to 100-300 kHz). Lastly, the digital input/output section of ADwin is used to control the switching of the multiplexer.

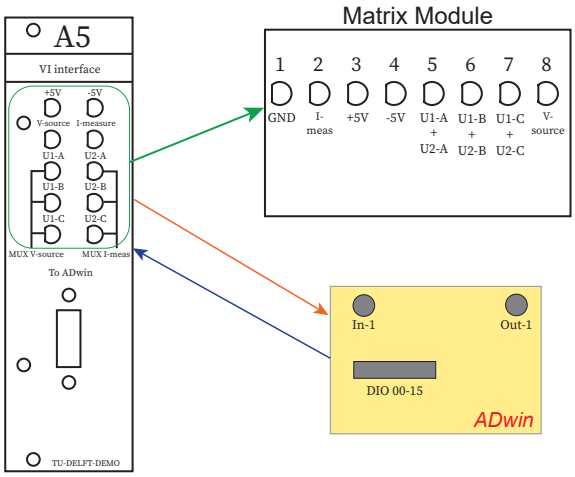

Figure 2.7: Schematic illustration of the connection of the PCB amplifier to the measurement system. The ADwin Gold II system is used to control the the voltage bias sent to the PCB through its internal DAC (Out-1), and the multiplexers using the digital input-output connector (DIO 00-15). The output voltage of the amplifier is read through ADwin's ADC (In-1). The connection between the ADwin system and the control computer is sustained by Ethernet.

A specific interface module (A5) was designed[6] to facilitate the connection process. Figure 2.7 shows a simplified scheme of the connections. BNC cables are used to connect ADwin's analog input and output to the rack, which connects them to the A5 module. A DB25 to DB9 cable is used to connect the digital I/O to the A5 module. Notice, internally only 6 wires in this cable are connected, 3 controlling the binary input to MUX V-source, and 3 for MUX I-meas. Additionally, the module provides access to ±5 V rails to power the op-amp and the multiplexers on the PCB. Lastly, the A5 module is connected to the matrix module through MCX cables.

2.3.1. PCB-AMPLIFIER CHARACTERIZATION

The amplification design presented here is quite simple with respect to some of the designs present in literature[123, 124], yet, it is surprisingly effective. The time-domain response was tested using square voltage steps. Figure 2.8a shows the response of the amplifier when a bias step from 100 mV to 10 mV is applied at time t = 0 s. The output voltage approaches the final value following a curve of the form $-e^{-\beta t}$, and it takes

[6] design and realization by Hans van der Does

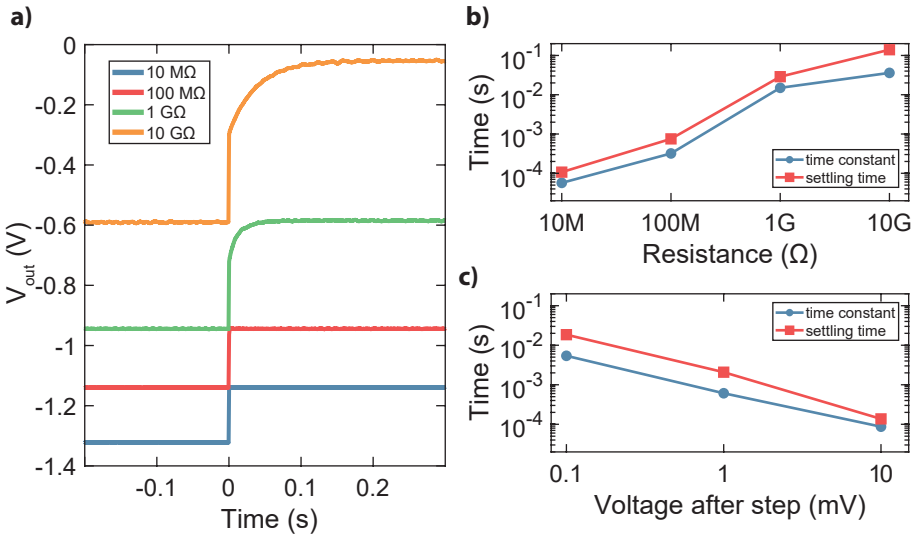

Figure 2.8: a) Voltage output of the logarithmic amplifier as a function of time, upon the application of a bias voltage step from 100 mV to 10 mV, using load resistors of 10 MΩ, 100 MΩ, 1 GΩ, and 10 GΩ. The horizontal axis origin is set to the instant the voltage is stepped to the lower value. b) Time constant and settling time as a function of load resistance. c) Time constant and settling time as a function of the voltage after the step. The voltage before the step has been set as 10 times the end value.

longer to do so with increasing load resistance. This behaviour closely resembles the charging of an RC circuit. Thus, the output voltage was fitted with with the function $log(|V - V_\infty|) = A + t/\tau$ where τ is the RC time constant. The resulting time constants are plotted in Fig. 2.8b, along with the settling time (defined as the time required for the output to be within 5% variation of the final value). For resistances up to 100 MΩ, the amplifier responds in less than a millisecond, but for resistances of 10 GΩ and greater, 100 ms or greater are required. This is still enough for performing a break-junction measurement, with some restrictions. We will further discuss the implications of this limit later in the section. Lastly, notice that the response time decreases with increasing voltage (Fig. 2.8c). This means that the voltage step used for the characterization in Fig. 2.8a-b is a worst-case scenario with respect to the measurements performed in the setup, which in any case use a bias greater than 10 mV.

The last step before using the PCB-amplifier for break-junction measurements is to calibrate its response. That is, to assign the relationship between the current through the channel, and the voltage at the output of the amplifier. Thus, resistors ranging from 10 Ω to 10 GΩ to the amplifier were connected to the amplifier, simulating a sample. For each of them, the bias voltage was swept from -1 V to +1 V while recording the output voltage of the amplifier. The resulting curves are shown in Fig. 2.9a.

The amplifier response follows the ideal logarithmic response from 1 mA to just over 10 pA, indicated by the linear dependence of current (in logarithmic scale) vs. output voltage in Fig. 2.9a. At smaller currents, the response deviates from the ideal behaviour,

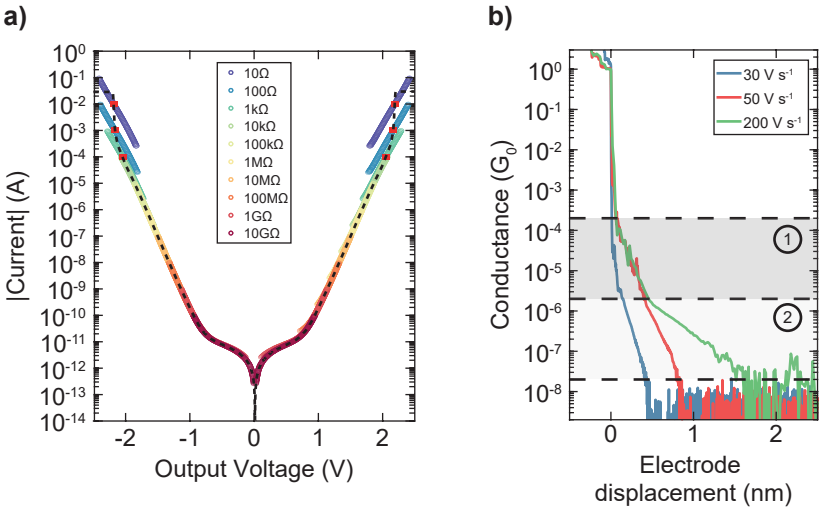

Figure 2.9: a) Current through the junction versus the corresponding amplifier output, measured using load resistors of 10 Ω, 100 Ω, 1 kΩ, 10 kΩ, 100 kΩ, 1 MΩ, 10 MΩ, 100 MΩ, 1 GΩ, and 10 GΩ. The square red dots correspond to the amplifier output at 0.1 V bias for the 10 Ω, 100 Ω, and 1 kΩ resistors. The dashed black line corresponds to the final calibration curve. b) Empty breaking traces measured with the PCB amplifier at different breaking speeds.

but it can be calibrated down to about 0.2 pA. This corresponds to almost two orders of magnitude improvement over the previous amplifier [47, 95, 98].

A significant deviation from the ideal response can also be observed for high resistances (10 Ω and 100 Ω). This is linked to the deviation from the ideal beahviour of the voltage divider. The voltage drop across the load will be half of the applied bias only if the load is much greater than the series resistance. That is, if it is much greater than 220 Ω (neglecting the multiplexers and the PCB tracks resistances). This is always satisfied in the range of interest for break-junction measurements (>10 kΩ, or <1.3 G_0), making this calibration procedure accurate for that interval.

However, it is useful to measure down to, and below, 1 kΩ as the making cycle of a trace reaches about 430 Ω (30 G_0). To calibrate the amplifier to a wider current range, only the points at a fixed bias of 100 mV (the typical bias used in the measurement) for 10, 100, and 1k Ω are considered (shown as red squares in Fig. 2.9a). Then, the response is interpolated to smoothly join these three points to the exponential response measured with the 1 kΩ and 10 kΩ resistors. The resulting curve is plotted as a dashed black line in Fig. 2.9a, and it corresponds to the calibration curve for the amplifier. Notice that this procedure has a main drawback: the applied bias has to be 100 mV when the resistance is equal to 1 kΩ or smaller, otherwise the measured value will not be calibrated correctly. However, it is possible to work around this limitation by first bringing the junction to a high-enough resistance using 100 mV bias, and then ramp the voltage to the desired value. This still allows to measure the molecular conductance at any reasonable bias. Additionally, due to the presence of 1 kΩ, 10 MΩ, and 10 GΩ resistors on the PCB, it is

possible to automatically adjust the calibration in case it drifts (e.g. due to temperature changes). However, the 10 Ω and 100 Ω are still left to manual calibration.

Finally, when measuring an empty MCBJ device, the traces seem different depending on the breaking speed. Examples of breaking traces measured with the new amplifier at different breaking speeds are shown in Fig. 2.9b. It is possible to identify two regions of interest. The first, labelled as 1 and shaded in gray, falls between $2{\cdot}10^{-4}$ G_0 and $2{\cdot}10^{-6}$ G_0. The second, labelled as 2, extends from $2{\cdot}10^{-6}$ G_0 to the noise level ($2{\cdot}10^{-8}$ G_0). Considering first the trace at a breaking speed of 200 V s^{-1} (≈4 nm s^{-1}, in green), it follows an exponential decay compatible with the empty device in region 1. However, in region two the slope changes to a smaller one (as if the conductance decays more slowly with displacement). When slowing down the measurement to 50 V s^{-1} (≈1 nm s^{-1}, in red), the breaking trace overlaps with the previous one in region 1. However, in region 2 the trace maintains the same slope as in region 1. Lastly, using a speed of 30 V s^{-1} (≈0.6 nm s^{-1}, in blue), the trace shows an almost vertical decay in region 1, while in region 2 it follows a slope similar to the trace at 50 V s^{-1}. These observations can be explained by considering that the limit between region 1 and 2 corresponds to a resistance of about 5 GΩ. As observed in Sec. 2.3.1, the response of the amplifier becomes considerably slower in this range. Thus, the smaller slope in region 2 at 200 V s^{-1} is due to the lag in the amplifier response to the rapidly changing displacement. Decreasing the speed to 50 V s^{-1} is enough to meet the condition such that the change in displacement is slow enough that the amplifier can follow it. Despite this, there is still a residual feature of the change of the amplifier response: the small peak at $\approx 10^{-6}$ G_0 in the 1D histogram mentioned in the discussion of Fig. 2.3a. However, the measurement speed cannot be decreased indefinitely, since that will cause the 1 G_0 plateau to self-break [125, 126], similarly to what happens at 30 V s^{-1}. Notice, at 200 V s^{-1} the response of the amplifier is still fast enough to retrieve the correct conductance value until $2{\cdot}10^{-6}$ G_0. Thus, it is still possible to measure at high speed, as long as the measured molecular features have higher conductance than this threshold.

Notably, the conductance threshold at which the trace transitions from region 1 to region 2 decreases with increasing bias voltage. More specifically, this shift always happens around a current value of ≈8 pA. This will be evident in Ch. 6, in particular in the 2D-histograms reported for bias dependence in the appendices 6.A and 6.B. This behaviour allows to distinguish between artefact peaks in the 1D-histograms, whose conductance decays with $1/V_{bias}$, and molecular peaks, which show a different dependence.

2.4. FABRICATION OF MCBJ DEVICES

The fabrication process to make MCBJ devices is based on the one developed by Martin [96] and adapted by Perrin [97]. The description of each step can be found in Sec. 2.A.1. We note that the main difference lies in the reactive ion etching step, now performed in pure oxygen plasma, in a different etcher. Figure 2.10a shows a scanning electron microscope (SEM) picture of a standard device, illustrating two suspended gold wires.

In addition to the standard fabrication recipe, additional approaches have been explored with the goal of obtaining devices which can be used to measure in liquid. The objective is to control the charge transport in molecules by changing its surrounding environment [127–129], and to implement an electrochemical gate in the MCBJ setup [130–

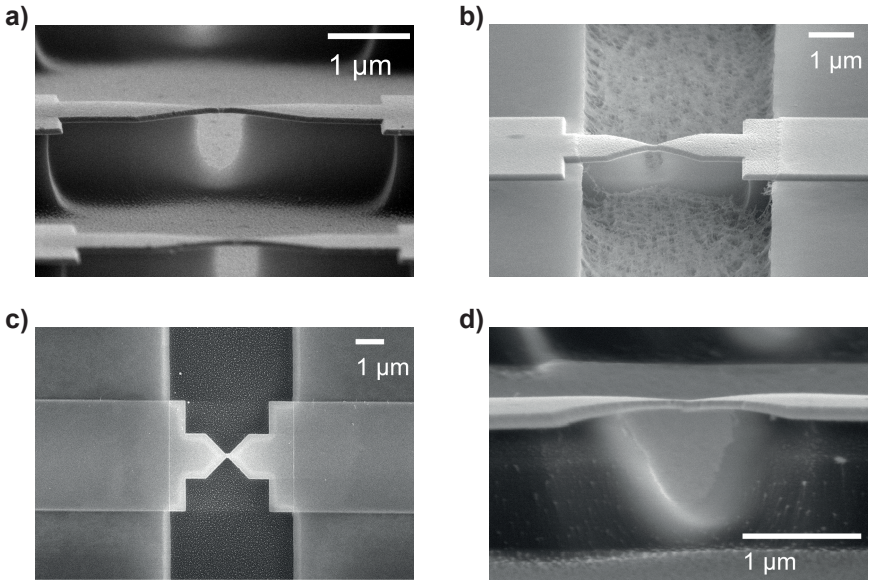

Figure 2.10: Scanning electron microscpe (SEM) micrographs of a) the standard MCBJ device, b) passivated devices with window patterned by Ar milling, c) top-view and d) cross-section of passivated devices patterned by lift-off. Before imaging, 5 nm of gold have been sputtered on the device, to avoid imaging artefacts. The small white dots visible especially in c) are a result of this step, and are not present in devices used in measurements.

132]. However, to measure in a (conductive) liquid it is necessary to passivate the electrodes, i.e., to reduce their surface area exposed to the solution. In fact, when the gold electrode are immersed in a conductive liquid, parasitic currents can flow through it, increasing the noise floor of the measurement. In a STMBJ, this can be achieved by insulating the gold tip with a layer of insulating polymer [133, 134]. However, this approach is not feasible for the lithographic process of our MCBJ devices. Although it is possible to isotropically cover the electrodes using atomic layer deposition [135], the yield of the process is low. Additionally, the small surface area exposed to the liquid on one side decreases the noise floor, but on the other side it decreases the available sites to which molecules can bind. Thus, it is desirable to develop passivated devices that have a larger exposed area for binding to the molecules. In the following, two approaches to obtain this are described. Both follow the same principle: pattern a $\approx$5 μm window in an oxide layer that exposes the bridge of the MCBJ devices, but cover the vast majority of the leads. The fabrication procedures are reported in the appendix (Sec. 2.A.1).

The first approach consists of first depositing an oxide layer (in this case aluminium oxide, AlO_x), and then pattern the window by argon milling. A resulting device is shown in Fig. 2.10b. The etched polyimide surrounding the undercut displays a peculiar "fur-like" texture, i.e., a rough surface composed of thin fibers. This feature arises from the combination of the roughness generated during ion-milling, followed by oxygen etching [136]. This factor, in addition to the increase in roughness of the gold layer, led us to exclude this approach for the passivation of the devices.

The second approach shifts the patterning technique to lift-off. Additionally, hafnia (hafnium dioxide, HfO_X) is used as passivation material due to its superior stability in high and low pH environments with respect to aluminium oxide [137, 138]. Figure 2.10c and d display a top-view and a side-view of a device fabricated using this procedure. There are a few differences worth highlighting. First, the fur-like structure in the polyimide is not present with this procedure. Second, the undercut of the gold bridge is not as well-defined as in the non-passivated samples (compare the smooth profiles in Fig. 2.10a with the irregular ones in Fig. 2.10d). However, the undercut fully develops to around the same size in both cases. Thus, no major differences in the device operation are expected.

We tested the hafnia passivated device performance. Figure 2.11a displays the 2D-histograms of one of such devices, measured in air, without addition of any molecular solution. The passivated device shows a tail of counts extending from 1 to 10^{-3} G_0, and diplacement up to around 0.3 nm, in contrast with the standard device, which shows an abrupt transition to an exponential decay (compare to Fig. 2.3a). This behaviour is unlikely linked to simple contamination of the devices. In fact, cleaning the devices either with an ozone treatment or by immersion in hot-acetone did not yield any improvement. However, since the unexpected behaviour is limited to low displacements, we can still observe molecular features of longer compounds. Thus, we performed a test measurement in liquid by using a solution of a hydroxyphenalenone compound in methanol [7] [139]. However, the measurement did not allow to gather a large dataset of traces, and no clear molecular feature was detected, as shown in Fig. 2.11b. On the positive side, the passivation procedure allowed to keep the noise floor of the measurement below 10^{-7} G_0. Thus, the patterning of the window covers the electrodes more than sufficiently to allow for measurements of metal-molecule-metal nanoscale junctions. However, the process needs to be refined to obtain a cleaner breaking of the device. The most straightforward option would be to deposit the gold bridge after the patterning of the passivation layer.

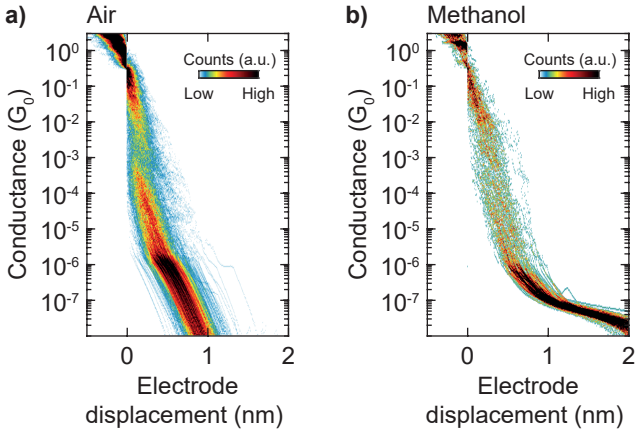

Figure 2.11: 2D conductance-displacement histograms for a device passivated with HfO_X in a) air (1000 traces) and b) methanol (100 traces).

[7] Synthesis by D. Vogel, in the group of M. Mayor, Basel University).

2.A. APPENDIX

2.A.1. NANOFABRICATION PROCEDURES FOR MCBJ DEVICES

All spin-coating steps mentioned in the following recipes consist of a 5 s ramp step followed by 55 s step at the target speed.

STANDARD MCBJ RECIPE

- Substrate Preparation
    1. Starting from a 50 × 50 × 0.5 mm phosphor bronze substrate.
    2. Cleaning 10 minutes sonication in acetone, followed by 10 minutes sonication in isopropanol.
- Deposition of the polyimide layer
    1. Heat the clean wafers on a hot-plate at 120°C for 60 s.
    2. Dropcast the adhesion promoter (VM651, HD Microsystems, diluted at 0.1 % v/v in isopropanol) and soak for 30 s.
    3. Spincoat at 3000 rpm.
    4. Bake on a hot-plate at 120°C for 60 s.
    5. Spincoat with polyimide (PI2610, HD Microsystems) at 800 rpm, taking care that the polyimide is at room temperature before starting the process.
    6. Hard-bake the substrate in a vacuum oven at 300°C for 30 min.
- e-beam resist deposition
    1. Spincoat the substrate with a 8% methylmethacrylate-methacrylic solution in ethyl lactate [MMA(8.5)-MAA EL8], at 3000 rpm.
    2. Bake on a hot-plate at 185°C for 7 min.
    3. Spincoat the substrate with a 4% Poly(methyl methacrylate) 950k solution in anisole (PMMA 950K A4), at 6000 rpm.
    4. Bake on a hot-plate at 185°C for 7 min.
- e-beam lithography
    1. Exposure in en electron-beam pattern generator (Raith EPBG5000 Plus HS 20bit B017. The contact pads are exposed with a dose of 750 μC cm^{-2}, using the largest available beam size; the central bridge is written with a dose between 1000 and 1300 μC cm^{-2}. The exact dose depends on the beam size and current, and was chosen according to a dose test performed at every filament change.
    2. Develop the pattern in a methyl-isobutylketone (MIBK) - isopropanol (IPA) mixture (1:3 v/v), followed by 30 s rinse in IPA.
- Gold film deposition

1. Deposition of 3 nm (0.5 Å s^{-1}) of titanium as adhesion layer, followed by 80 nm of gold (1 Å s^{-1}) (using an electron-beam evaporator Temescal FC-2000).
2. Lift-off in acetone (overnight at room temperature, or 1-2 h at 50°C).
3. Rinse in acetone and IPA.

- Protection layer deposition

  1. Spincoat the substrate with a 3% Poly(methyl methacrylate) 495k solution in anisole (PMMA 950K A4), at 2000 rpm.
  2. Bake on a hot-plate at 185°C for 1 min.
  3. The substrate is then hand-cut to separate the individual samples using a metal cutting guillotine.

- Suspension of the MCBJ bridge

  1. Remove the protection layer in acetone at 50°C, for at least 15 min.
  2. Reactive ion etching (RIE) of the polyimide layer (Sentech RIE plasma etcher Etchlab 200), using a flow of oxygen at 50 sccm at a pressure of 200 μbar, and an RF bias of -81 V, corresponding to roughly 32 W power. The thickness of the etched polyimide is monitored in-situ using a built in laser interferometer. The process is stopped after five and a half oscillations of the interferometer signal, corresponding to the removal of around 1 μM of polyimide.

PASSIVATION USING AN ALUMINA LAYER PATTERNED BY ION MILLING

These steps are performed after following the standard recipe until and including the gold deposition step.

- Deposit 20 nm of aluminium oxide by ALD at 300°C (Oxford instruments Flexal ALD).

- Resist deposition and exposure

  1. Spincoat the S1813 (Microposit) UV resist at 3000 rpm.
  2. Bake on an hot-plate at 120°C for 2 min.
  3. Expose the pattern in a NUV photolitography mask aligner (EVgroup EVG620). The dose is around 53 mJ cm^{-2}.
  4. Develop the pattern in MF321 (Microposit) for 60 s. Follow by rinsing for 30 s in DI water. Then rinse again in DI water.

- Argon mill the oxide layer using an ion mill (SCIA ion mill 150, using 250 W power and 600 V acceleration voltage). The process was monitored using a in-situ secondary ion mass spectrometer (Hiden SIMS End Point Detector). Once no more Aluminium was detected, the process was stopped.

After these steps, the standard recipe for the protective layer and for etching is followed. Notice that the pattern in the oxide includes windows to access the polyimide with the laser interferometer.

PASSIVATION USING AN HAFNIA LAYER PATTERNED BY LIFT-OFF

These steps are performed after following the standard recipe until and including the gold deposition step.

- Resist deposition
  1. Bake the substrate on a hot-plate at 185°C for 15 min. This step is crucial to obtain good resist adhesion.
  2. Spincoat a layer of ma-N 1410 resist (Micro resist technology) at 3000 rpm.
  3. Bake on an hot-plate at 120°C for 2 min. This results in a layer thickness of around 1 μm.
- Exposure and development
  1. Expose the pattern using a Heidelberg μMLA Laserwriter, with a dose of 180 mJ cm^{-2}.
  2. Develop in ma-D 533/S (Micro resist technology) for 100 s, then rinse in DI-water for 30s. Follow with a second rinse in DI-water. Gently blow-dry the excess water from the substrate. This results in a negative pattern with a wide undercut.
  3. Bake on an hot-plate at 120°C for 2 min.
  4. Flood exposure of the pattern in a NUV photolitography mask aligner (EV-group EVG620) for 60 s. This step is necessary to increase the cross-linking of the resist, which improves its thermal stability.
- Hafnia layer deposition
  1. Sputter HfO_x with an RF magnetron sputterer (Alliance Concept AC450), using a pressure of 1.5 μbar of Argon for 280 s, resulting in around 60 nm of thickness.
  2. Lift-off in acetone using mild sonication.

After these steps, the standard recipe for the protective layer and for etching is followed. Notice that the pattern in the oxide includes windows to access the polyimide with the laser interferometer.

3

Charge Transport in Acene-substituted OPE3s: from Nanoscale to Large-Area Junctions

In this chapter we describe the charge transport properties of a series of molecules with increasing intermolecular interactions. The focus is on the similarities and differences when characterising the compounds at the nanoscale, using the mechanically controllable break-junction (MCBJ) technique, or in large-area junctions, with the eutectic Gallium Indium (EGaIn) technique. MCBJ experiments show multiple conductance plateaus. The high-conductance plateau, shows an increase of conductance as a function of acene length, in good agreement with theoretical predictions. In large-area junctions, the pentacene derivative has suppressed conductance. We ascribe this to its inability to form a monolayer without introducing significant low-conductance paths due to intermolecular effects. This hypothesis is supported by the MCBJ data and theoretical calculations. These results highlight the role of intermolecular effects and junction geometries in the observed fluctuations of conductance values between single-molecule and ensemble junctions, and the importance of studying molecules in both platforms.

Parts of this chapter have been published in The Journal of Physical Chemistry C **124**, 22776-22783 (2020).

The Self-Assembled Monolayer characterization and the theoretical calculations presented in this chapter have been performed by Y. Liu , M. Carlotti , Y. Ai, S. Soni, and R.C. Chiechi (University of Groningen). Synchrotron XPS measurements were performed by A. Asyuda and M. Zharnikov (Universität Heidelberg).

3.1. INTRODUCTION

Molecular electronics aims at controlling the conduction properties of molecules, and implementing their intrinsic functionalities in electronic devices [140]. Different methods are available to characterize molecular systems. These can be classified in two categories [141]: "single-molecule" junctions, in which the contact electrodes have atomic-nanometric size [41, 142], and "molecular array" junctions, in which the electrodes can vary from hundreds of nanometers to millimiters [7, 143]. Ideally, in both approaches, the molecules are anchored to one electrode on each side, so that the full molecular backbone contributes to charge transport. Despite this, the environment that the molecules experiences are different. In the "array" approaches a large number of neighbours are present, while in "single-molecule" techniques molecules are more isolated. This can lead to drastically different surface electrostatics [144], and suppression of current per individual wire [145].

In this chapter, we investigate how the charge transport properties of a series of oligo(phenylene-ethynylene) (OPE3) compounds change from the nanoscale to large-area junctions, using the mechanically controllable break-junction (MCBJ) and eutectic Gallium Indium (EGaIn) on self-assembled monolayers (SAMs) techniques respectively. OPE3s are a good choice as a model compounds for this study, as they have been widely characterized in literature with both techniques [89, 104, 118, 146–149]. For this study, as shown in Fig. 3.1a, the central benzene ring of OPE3 has been replaced with a series of oligoacenes: naphtalene (NP), antracene (9,10-AC), tetracene (TC), and pentacene (PC). This approach extends the π-conjugation perpendicular to the molecular backbone. However, the linear conjugation between the two sulfurs is unchanged across the series. Thus, the effect of intermolecular interactions can be investigated without changes in tunnelling barrier length, which would intrinsically affect the molecular conductance [146]. We find that the MCBJ measurements show multiple conductance plateaus. The high-conductance one follows the trend predicted by first-principle calculations. EGaIn measurements do not follow the same trend. In particular, PC shows a conductance suppression of two orders of magnitude with respect to the other compounds. We propose that this reduction arises from the stronger intermolecular interactions in PC. This hypothesis is supported by the MCBJ data and theoretical calculations.

3.2. BREAK-JUNCTION MEASUREMENTS

The nanoscale charge transport properties of the five molecules were characterized using the mechanically controllable break-junction (MCBJ) technique. Around 0.5 μL of a 0.1 mM solution of the desired compound were drop-cast on the junction (with the addition of 0.5 mM of tetrabutylammonium hydroxide, to favour the separation of the acetyl groups from the sulfur). After solvent evaporation, we performed fast-breaking measurements with a voltage bias of 0.1 V and a piezo actuation speed of 200 V s^{-1}. The histograms built from one such measurements of OPE3 are shown in Fig. 3.1b. The one-dimensional conductance histogram shows a clear peak at $6.3 \cdot 10^{-5} G_0$, corresponding to a plateau in the two-dimensional conductance-displacement histogram with a length of about ≈1.5 nm. These values are consistent with previous measurements reported in literature [57, 104, 118, 148], although the conductance value is slightly lower. We will

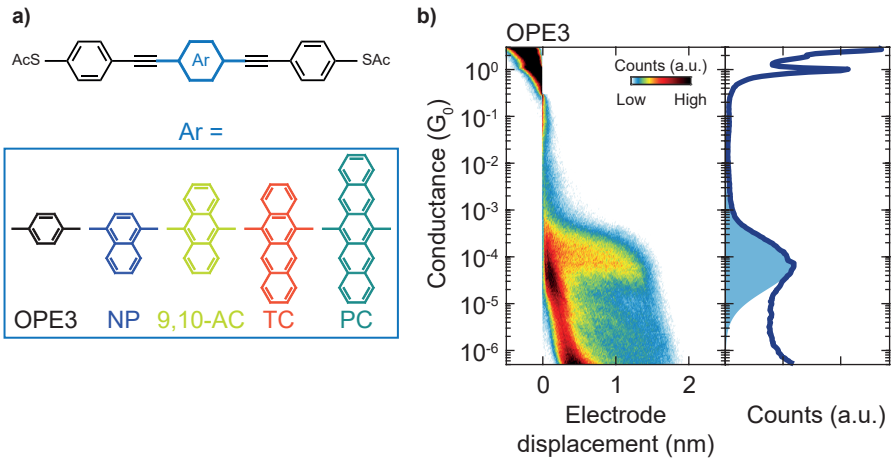

Figure 3.1: a) Molecular structures of the compounds in this study. b) Two-dimensional conductance-displacement histogram (left) and one-dimensional conductance histogram (right) of the raw data of an OPE3 measurement. The light blue area is the log-normal fit to the peak in the 1D-conductance histogram.

comment on the latter aspect in section 3.2.1. All the studied molecules show a similar plateau, whose most probable conductance follows the trend: OPE3<NP<AC≈TC<PC (Tab. 3.A1). In addition, low-conductance features are observed in all the molecules. However, they are not as evident in the full dataset as the high-conductance plateau.

3.2.1. CLUSTERING ANALYSIS

We performed clustering analysis on the datasets to isolate the different features in the measurement. We used a reference-free clustering method detailed in previous work [89] and in Sec. 3.2.1. In this work, the feature space was defined as follows. We used a 25x32 pixels image of the 2D-histogram, with displacement range from −0.5 nm to 3 nm, and the conductance range from −0.5 to −6 $\log(G/G_0)$. Additionally, the 1D conductance histogram, with 100 bins, was appended to the feature vector created from the image. As for the number of classes, we considered the minimum number that would allow for the isolation of the high-conductance plateau. Figure 3.2 shows the results of the clustering analysis performed on the OPE3 measurement shown in Fig. 3.1b. In addition to the high-conductance class, we obtain one class containing low-conductance features, and one class containing empty traces. It is possible to isolate these classes in each molecule.

The high-conductance classes all consist of a plateau around 1.5 nm long and with a conductance in the $10^{-4}G_0$ range. An example of a 2D-histogram for each molecule is shown in Fig. 3.4. To compare the shape and position of the high-conductance peaks, we also build 1D-histograms including all measurements of the corresponding molecule. Then, the histograms are rescaled by peak-height. Figure 3.3 shows the result of such an analysis. All molecules show a similar peak, with the exception of PC which has a slightly broader one. The conductance of this plateau follows the same trend found for the raw data: OPE3<NP<AC≈TC<PC (Tab. 3.A2). Notice that the OPE3 conductance values extracted from the clustered datasets are now the same as the values previously reported

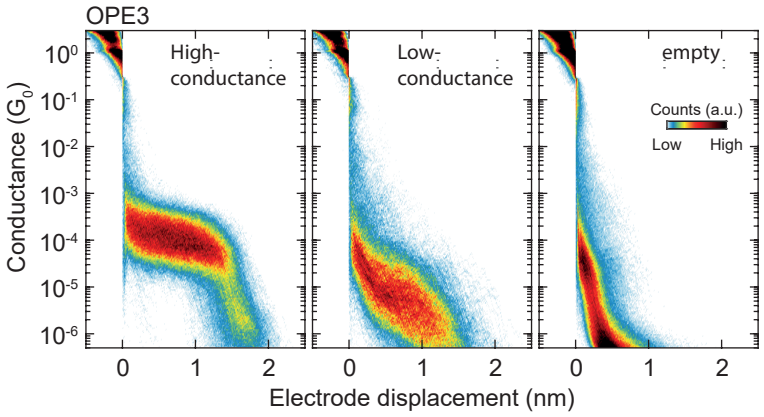

Figure 3.2: Two-dimensional conductance-displacement histograms of the high-conductance class (left), low-conductance class (centre), and empty traces obtained for the OPE3 measurement shown in Fig. 3.1.

in literature [57, 104, 118, 148]. The reason is that the 1D histograms of the clustered data yield more prominent and narrower peaks than the unfiltered data, due to the removal of the "background" of low-conductance and empty traces.

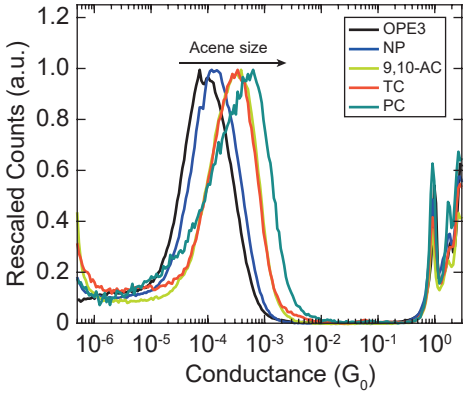

Figure 3.3: One-dimensional conductance histograms of the high-conductance class for OPE3, NP, 9,10-AC, TC, and PC. Each histogram includes the traces from all measurements from the corresponding molecule. Counts are rescaled by peak height.

Low-conductance classes show a more complex behaviour. The 2D-histogram of one measurement for each molecule is reported in Fig. 3.5. OPE3 exhibits a slanted plateau at conductance lower than $10^{-5}G_0$. NP and 9,10-AC have two clear peaks: one at $3 \cdot 10^{-5}G_0$, and another one at $2.2 \cdot 10^{-6}G_0$ (for NP) and $1.5 \cdot 10^{-6}G_0$ (for 9,10-AC). TC has a short plateau at $3.6 \cdot 10^{-5}G_0$, while PC shows a plateau longer than 2 nm at $8 \cdot 10^{-6}G_0$ (see Tab. 3.A3 for the fit results for each measurement).

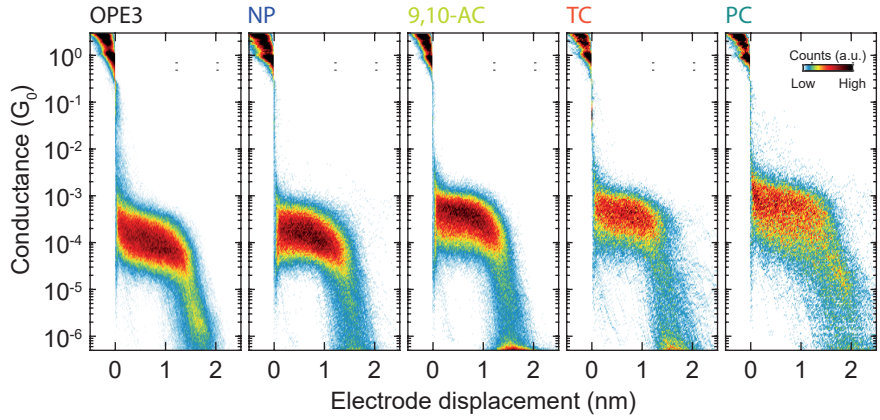

Figure 3.4: Two-dimensional conductance-displacement histograms of the high-conductance class obtained from one measurement of (from the left): OPE3, NP, 9,10-AC, TC, and PC.

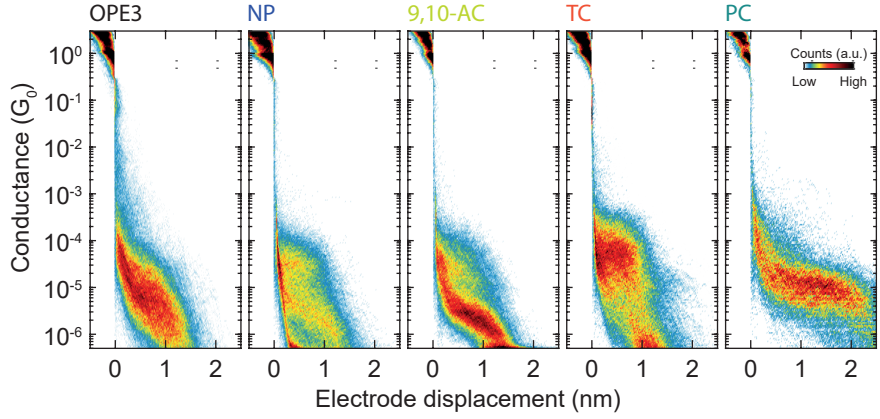

Figure 3.5: Two-dimensional conductance-displacement histograms of the low-conductance class obtained from one measurement of (from the left): OPE3, NP, 9,10-AC, TC, and PC.

3.3. SELF-ASSEMBLED MONOLAYER EXPERIMENTAL RESULTS

We measured the charge transport properties of the series in large-area junctions using the eutectic Gallium Indium (EGaIn) technique. In this approach, one electrode consists of a tip of liquid EGaIn which makes conformal contact with the SAM. The second electrode is the gold surface on which the SAM is grown onto. The result is a two terminal junction whose contact area is of the order of thousands of μm^2. For an in-depth description of the EGaIn technique we refer to [150]; for the details of SAM growth see the Theoretical Methods of the publication this chapter is based on [106].

Figure 3.6a shows the current-density vs. voltage (J/V) curves measured for each of

the compounds in this study. OPE3, NP, 9,10-AC, and TC have similar behaviour, with the current-density slightly decreasing as the size of the central aromatic unit increases. PC has a different behaviour: the current-density at low bias is two orders of magnitude lower than for the other compounds, corresponding to an equally lower conductance (Fig. 3.6b). Additionally, J rapidly increases as the voltage increases, resulting in a V-shaped J/V characteristic.

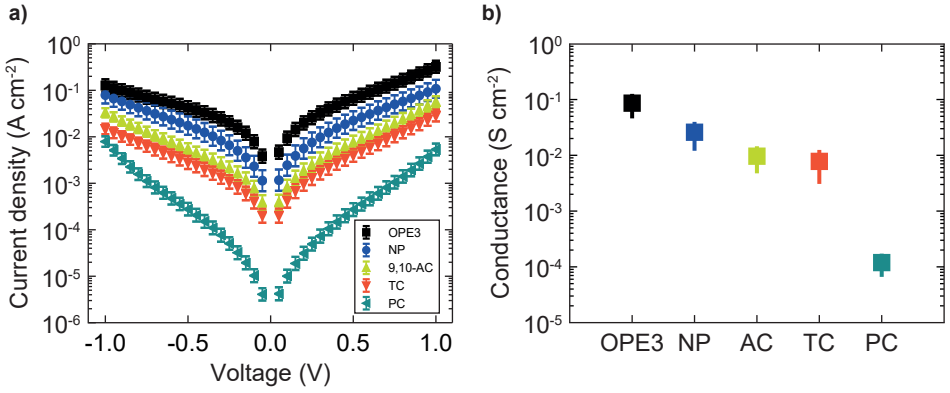

Figure 3.6: a) Absolute value of current-density versus bias voltage for each molecule in the series. Each data point is the mean from a Gaussian fit to a histogram of log |J|. b) Conductances of SAMs of the acence series, extracted from the J/V traces of EGaIn data in panel a).

The simplest reason for such a drastic conductance decrease would be a poor quality SAM. To rule out this option, we performed structural characterization of the monolayers grown in this study using x-ray photoelectron spectroscopy (XPS). Angle-resolved XPS measurements were performed with an home-built setup at the Univeristy of Groningen [151]. Additionally, Synchrotron-based X-ray photoelectron spectroscopy (XPS) measurements were performed at the HE-SGM beamline (bending magnet) of the German synchrotron radiation facility BESSY II in Berlin using a custom-designed experimental station [152]. For a full description of the methodology, see [106]. Table 3.A5 reports the resulting SAM thickness and packing density of the molecules in this study, together with a octadecanethiol (SC18) reference [153]. The packing densities of OPE3, NP, 9,10-AC, and TC are similar, although slightly decreasing. This is congruent with the measured conductance of such films. Notice that PC has a similar packing density and thickness to the other compounds. Thus, the quality of the SAM cannot be the reason for the low conductivity of PC.

3.4. THEORETICAL CALCULATIONS AND DISCUSSION

We performed first-principle calculations to gain further insight on the dependence of the conductance on the size of the acene unit. The molecular geometry was first optimized in gas phase, using the ORCA 4.10 software package [154, 155]. The energy levels were computed after attaching the compound to gold clusters through its terminal sulfur atoms. Lastly, the transmission curves were computed with the ARTAIOS package [156, 157]. For

the full details of the calculations, we refer to the Theoretical Methods of the publication this chapter is based on [106].

Figure 3.7a shows the transmission curves computed for each of the molecules in this study. The frontier energy level gap (E_g) decreases as the size of the central acene increases from OPE3 to PC. This is in good agreement with the well-known decrease in HOMO-LUMO gap observed in polyacenes of increasing size [158, 159]. The resonances thus move towards the Fermi level. In the region close to the Fermi level the transmission moderately and continuously increases, reflecting the change of the frontier energy levels. Overall, a five-fold increase in conductance is predicted from OPE3 to PC.

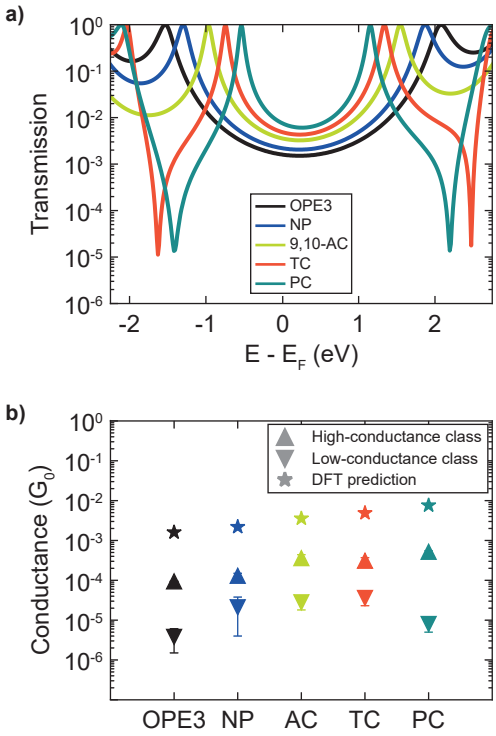

Figure 3.7: a) Transmission spectra calculated for the molecules in this study. The energy is referenced to an estimated Fermi level of -4.3 eV, which is common for EGaIn junctions [160]. b) Conductance values of high- (upwards triangles) and low-conductance (downwards triangles) classes measured with MCBJ, compared to the values predicted from the transmission spectra (stars). The conductance value has been estimated as $G = G_0 \cdot T(0)$.

We note that the energy axis has been referenced to a Fermi level position of -4.3 eV, which is common for EGaIn junctions. The reader may question whether this is an appropriate choice for describing gold-based junctions. For pure gold in vacuum, the work function is known to be -5.1 eV; however, this values shifts to -4.4 eV to -4.2 eV when the surface is covered by a SAM [161–163]. In the case of MCBJ junctions, the situation is intermediate between these two: the gold surface is covered in molecules, but those are

not as densly packed as in a self-assembled monolayer. Hence a Fermi level of -4.3 eV is too high to best predict the properties of gold junctions. However, notice that a negative shift of the Fermi level of about 0.5 eV does not change the trend in the prediction from the DFT calculations. Thus, all the qualitative considerations made in this section still hold, and a quantitative agreement with experiments is not expected from these calculations.

The trend predicted through first-principle calculations matches well the trend observed for the high-conductance class of MCBJ measurements. This is consistent with the interpretation of such plateau corresponding to tunnelling through the molecule when it is anchored through sulfur on both sides [57, 81, 104, 148]. The low-conductance class and EGaIn measuremets do not follow this trend. This suggests that there are additional effects present in these cases. There are two main interpretations in literature for secondary peaks in break-junction OPE3 measurements: changes in the surface coordination of the sulfur-gold bond [104], or the formation of π-stacked dimers in the junction [81, 82]. We did not perform detailed calculations of each possible configuration and binding geometry to determine the origin of each feature in the low-conductance class, as a detailed description of those is outside the scope of this study. However, we can comment on it based on the measurements presented in Fig. 3.5, Tab.3.A3, and Tab.3.A4. For all molecules, with the exception of PC, the low-conductance class shows plateaus shorter than, or with comparable length to, the high-conductance plateau. Only in the case of PC we observe long traces with relatively high yield. This could imply that in nanoscale junctions the formation of π-stacked dimers is statistically significant only for the largest acene core, for which intermolecular interactions are the most intense of the series.

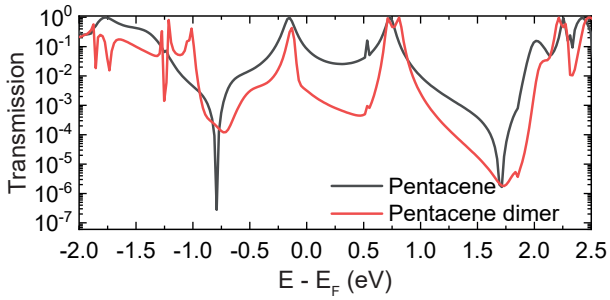

Figure 3.8: Transmission spectra calculated for PC (black line) and a PC dimer (red line).

In light of this marked difference of PC, we performed an additional simulation on a metal-dimer-metal junction, consisting of two molecules of PC stacked on top of each other, and connected to the electrodes so that neither of them bridges both electrodes. This calculation was performed using the BAND module of Amsterdam Density Functional (ADF) quantum chemistry program [164–167]. The resulting transmission curve is shown in Fig. 3.8 (red line), together with a reference calculation of a single PC molecule (black line). The dimer configuration has up to two orders of magnitude lower transmission in the range of energies in-between the HOPS and LUPS. This indicates that the π-stacked configuration has lower conductance than the non-interacting case, which is in good agreement with the MCBJ experiments.

Ensemble EGaIn measurements have a surprisingly similar behaviour to MCBJ ones. The conductance of the system is similar across the series, with the exception of PC. Thus, we hypothesise that, as the size of the central acene increases, intermolecular interactions in the SAMs become increasingly more important, introducing more and more "low-conductance" molecular configurations in the ensemble. However, as long as even a small fraction of molecules is left in the "high-conductance" state the observed conductance drop would not be substantial [168–170]. Hence the intermolecular interactions in PC are strong enough that the molecules in the junction no longer behave as independent tunnelling paths, showing suppression of the conductance.

3.5. CONCLUSION

In this chapter, we characterised the charge transport properties of a series of acene-substituted OPE3s with increasing π surface area, using the MCBJ and the EGaIn techniques. MCBJ measurements show the presence of a high-conductance plateau and of low-conductance features. The high-conductance plateau follows the same trend as DFT+NEGF calculations in the metal-molecule-metal geometry. Regarding the low-conductance features, only in the case of PC traces longer than the high-conductance plateau are observed. In EGaIn junctions, PC shows a significant suppression of conductance compared to the other compounds. This behaviour cannot be explained by bond topology or formation of multilayers. We suggest that, in analogy to the MCBJ case, strong intermolecular interactions in PC lead to the suppression of conductance.

To conclude, MCBJ nanoscale junctions allow to measure and isolate both isolated molecules and interacting dimers. In EGaIn measurements of SAMs, where molecules seek a thermodynamic-minimum packing, only the overall behaviour can be observed. When intermolecular interactions are strong enough, in the case of acene-substituted OPE3s, this results in a suppression of conductance.

3.A. APPENDIX - TABLES SUMMARIZING THE EXPERIMENTS AND FITTING RESULTS

Table 3.A1: Conductance values and full-width half-maximum (FWHM) extracted from fitting the raw data of each measurement, and total number of traces .

Molecule	Measurement	Conductance (G_0)	FWHM (decades)	N° traces
OPE3	1	$6.3 \cdot 10^{-5}$	1.4	10000
	2	$8.9 \cdot 10^{-5}$	1.2	10000
NP	1	$1.0 \cdot 10^{-4}$	1.2	10000
	2	$1.4 \cdot 10^{-4}$	1.1	10000
	3	$9.7 \cdot 10^{-5}$	1.2	10000
9,10-AC	1	$3.7 \cdot 10^{-4}$	0.8	10000
	2	$3.9 \cdot 10^{-4}$	1.0	10000
	3	$1.6 \cdot 10^{-4}$	1.2	10000
	4	$3.0 \cdot 10^{-4}$	1.0	10000
TC	1	$2.5 \cdot 10^{-4}$	1.0	10000
	2	$2.4 \cdot 10^{-4}$	1.1	10000
	3	$1.4 \cdot 10^{-4}$	1.3	10000
PC	1	$4.0 \cdot 10^{-4}$	1.1	7324
	2	$3.0 \cdot 10^{-4}$	1.5	7182

Table 3.A2: Conductance values and full-width half-maximum (FWHM) extracted from fitting the high-conductance class for each measurement. The yield is the percentage of traces classified in this class with respect to the total number of traces.

Molecule	Measurement	Conductance (G_0)	FWHM (decades)	Yield (%)
OPE3	1	$9.4 \cdot 10^{-5}$	1.1	22
	2	$9.5 \cdot 10^{-5}$	1.2	17
NP	1	$1.2 \cdot 10^{-4}$	1.1	22
	2	$1.5 \cdot 10^{-4}$	1.1	26
	3	$1.3 \cdot 10^{-4}$	1.0	21
9,10-AC	1	$4.1 \cdot 10^{-4}$	0.8	20
	2	$3.6 \cdot 10^{-4}$	1.1	23
	3	$2.4 \cdot 10^{-4}$	1.0	3
	4	$4.3 \cdot 10^{-4}$	0.7	15
TC	1	$3.7 \cdot 10^{-4}$	0.9	6
	2	$2.8 \cdot 10^{-4}$	0.9	14
	3	$2.8 \cdot 10^{-4}$	1.0	6
PC	1	$5.5 \cdot 10^{-4}$	1.0	6
	2	$5.0 \cdot 10^{-4}$	1.0	6

Table 3.A3: Conductance values and full-width half-maximum (FWHM) extracted from fitting the low-conductance class for each measurement. Conductance 1/FWHM 1 refer to $\approx 10^{-5}$ peaks, Conductance 2/FWHM 2 to $\approx 10^{-6}$ ones. The yield is the percentage of traces classified in this class with respect to the total number of traces. *Measurement 3 of AC had too few low conductance molecular traces. Fitting was not possible.

Molecule	Measure-ment	Conduc-tance 1 (G_0)	FWHM 1 (decades)	Conduc-tance 2 (G_0)	FWHM 2 (decades)	Yield (%)
OPE3	1			$5.4 \cdot 10^{-6}$	1.9	16
	2			$2.2 \cdot 10^{-6}$	1.7	17
NP	1	$3.5 \cdot 10^{-5}$	0.8	$2.2 \cdot 10^{-6}$	2.8	33
	2			$1.6 \cdot 10^{-6}$	1.9	20
	3	$2.7 \cdot 10^{-5}$	1.0	$2.8 \cdot 10^{-6}$	3.0	25
9,10-AC	1	$2.4 \cdot 10^{-5}$	1.2	$2.0 \cdot 10^{-6}$	2.4	19
	2	$2.2 \cdot 10^{-5}$	1.4	$9.4 \cdot 10^{-7}$	3.7	30
	3					*
	4	$4.0 \cdot 10^{-5}$	1.3			28
TC	1	$4.3 \cdot 10^{-5}$	1.3			20
	2	$2.1 \cdot 10^{-5}$	1.7			18
	3	$4.5 \cdot 10^{-5}$	1.3			11
PC	1			$1.0 \cdot 10^{-5}$	1.0	7
	2			$5.6 \cdot 10^{-6}$	2.4	13

Table 3.A4: Length values extracted for all measurement in this study. HC refers to the high-conductance class, LC 1 refers to $\approx 10^{-5}$ peaks, LC 2 to $\approx 10^{-6}$ ones. *Measurement 3 of AC had too few low conductance molecular traces. Fitting was not possible.

Molecule	Measurement	Length HC (nm)	Length LC 1 (nm)	Length LC 2 (nm)
OPE3	1	1.4		1.2
	2	1.5		1.1
NP	1	1.4	0.3	0.7
	2	1.3		1.1
	3	1.4	0.8	0.7
9,10-AC	1	1.0	1.3	1.0
	2	1.4	0.8	0.7
	3	1.3	*	*
	4	1.0		1.2
TC	1	1.1	1.1	
	2	1.3	0.8	
	3	1.3	1.2	
PC	1	1.4		2.1
	2	1.5		1.5

Table 3.A5: Effective thickness of SAMs of acene molecules on Au surface by angle-resolved XPS, and packing density estimated from synchrotron XPS measurements. * This value is from earlier work in reference [149].

Molecule	Thickness(Å)	Packing density (molecules cm^{-2})±10%
SC18	20.9 ± 0.2	$4.63 \cdot 10^{14}$
OPE3	24.8 ± 2.3	$3.5 \cdot 10^{14}$*
NP	21.0 ± 1.7	$3.0 \cdot 10^{14}$
9,10-AC	34.9 ± 4.5	$2.9 \cdot 10^{14}$
TC	26.4 ± 1.9	$2.2 \cdot 10^{14}$
PC	26.8 ± 2.1	$2.9 \cdot 10^{14}$

4

CONTACT-DEPENDENT SWITCHING IN NANOSCALE MOLECULAR JUNCTIONS

Inducing switching, i.e., a sudden change in conductance, upon application of an external stimulus, has been a successful strategy to realise molecular electronic devices. This is often achieved by introducing elements in the molecule that change its conjugation path or its conformation. However, switching behaviour can also be observed in molecular junctions without any of these elements. In this chapter, we analyse the switching events in molecules where this behaviour is not introduced by chemical design: Oligo(phenylene-ethynylene)s (OPE3), having a rigid conjugated backbone, and alkanes, with a flexible structure. We systematically observe switching events in these molecules, involving two types of switching events: "plateau" and "tunnelling" switches. We propose that the former correspond to junctions created after rupture of the gold atomic point contact, while the latter can be related to a change in the contact geometry of the junction.

Part of the measurements shown in this chapter, and the switch identification script were performed by J. Kamer (TU Delft) during his MSc project. The alkane measurements were performed by M. El Abbassi (TU Delft).
Parts of this chapter have been published in The Journal of Physical Chemistry C **126**, 19843-19848 (2022).

4.1. INTRODUCTION

Nanoscale molecular junctions have been investigated for decades to use molecules as building blocks in electronic devices [40]. Charge transport properties of such structures are often investigated using break-junctions techniques [41]. Among these, stretching based methods (such as Scanning Tunnelling Microscope Break Junctions (STMBJ) and Mechanically Controllable Break Junctions (MCBJ)) have been widely employed because of the possibility of acquiring large statistical sets of data [171], which are then used to build one- and two-dimensional conductance histograms, as discussed in Sec. 2.1. This statistical analysis, however, hides information that can be obtained from individual breaking traces. For instance, spring-like molecules can show mechanosensitivity (i.e., conductance variations as a function of displacement), which gets smeared out when averaged in a histogram [172]. Another class of features that can be hidden by histograms is switching events, i.e., sudden changes of current flowing through the junction.

Switching behaviour has been observed in multiple instances, even in absence of external stimuli. For instance, unconventional increases of conductance during stretching have been linked to deprotonation of the anchoring group in a pyrazolyl terminated molecule [173]. Another proposed mechanism of switching consists of flipping between conformations in crank-like molecules [174]. Furthermore, González *et al.* [175] analysed the elongation behaviour of a diamine terminated oligo(phenylene-ethynylene) (OPE3-NH_2). In this study, they indicate that the presence of traces with switching events is linked to the formation of single-molecule junctions, where the bonding to the gold electrode is broken and reformed multiple times. Instead, traces showing no switching originate from junctions where multiple molecules bridge the nanogap. A more recent study by Chen *et al.* [176] analysed the presence of switching events in diamine- and dithiol-terminated alkanes using a novel technique, based on break-junction but using low breaking speed. They found good agreement with previously proposed explanations of multiple conductance states in alkanes [71]. Thus, the presence of switching events is a frequent feature in STMBJ and MCBJ measurements. It is observed both in conjugated and non-conjugated molecules, in molecules whose backbone is not changing upon external stimuli, and it can also be related to the nature of the anchoring group.

In this chapter, we systematically analyse the effect of both the anchoring group and the molecular backbone on the switching behaviour in MCBJ traces. For this reason, we characterise oligo(phenylene-ethynylene) derivatives with three benzene rings (OPE3), and in two alkanes (hexane and octane). Both systems are well-studied benchmark molecules in molecular electronics, the former having a rigid conjugated backbone [57, 59, 81, 104, 177, 178], the latter having a flexible, non-conjugated one [68, 71, 72, 80, 90, 179, 180]. Additionally, we consider different anchoring groups for each molecule. For OPE3, we use amino (-NH_2), pyridine (-Pyr), thiomethil (-SMe), and acetate protected thiol (-SAc). For alkanes, we opt for diamino (-NH_2) and dithiol (-SH) termination. This selection allows to explore strong covalent binding to the electrodes (-SAc and -SH), as well as the weaker dative one (-NH_2, -Pyr, and -SMe). The use of these backbones and anchors will constitute a solid foundation for future studies on switching in metal-molecule-metal junctions.

4.2. METHODS

OPE3-SAc, hexanedithiol, hexanediamine, octanedithiol, and octanediamine were purchased from Sigma-Aldrich and used without further purification. OPE3-NH_2, OPE3-Pyr, and OPE3-SMe were obtained as described in Ref. [57]. The chemical structure of the compounds analysed in this study is shown in Fig. 4.1. The conductance of the molecules was characterized using the MCBJ technique. Details of the method can be found in previous work [95], as described in Sec. 2.1. After checking for the cleanliness of the sample, about 5 μL of the molecular solution, in dichloromethane (Sigma-Aldrich), was dropcast on the device. The concentration of the solution used for the measurements is reported in Tab. 4.A1. After solvent evaporation, thousands of consecutive breaking traces were recorded on each device, using a constant bias voltage of 0.1 V and actuation speeds of either 50 or 200 V s^{-1}. The corresponding electrodes' speed ranges between 1 and 5 nm s^{-1}. An overview of the measurements can be found in Sec. 4.A.2.

4

4.3. RESULTS AND DISCUSSION

We first analyse the unsorted data of a typical measurement of this set of molecules, to characterize its most prominent features. The two-dimensional conductance vs. electrode displacement histogram of OPE3-NH_2 is shown in Fig. 4.2a and displays two plateaus. Log-normal distributions are fitted to the corresponding peaks in the one-dimensional histograms (shaded blue and green areas in Fig. 4.2a): a high-conductance one at $4.5 \cdot 10^{-5}$ G_0 and a low-conductance one at $1.0 \cdot 10^{-6}$ G_0. The presence of multiple plateau-like features in MCBJ measurements of OPE3 has been widely discussed in literature. Plateaus with a conductance around 10^{-6} G_0 are attributed either to the presence of π-stacked dimers, or to presence of multiple binding configurations [81, 104]. Notice that the measurement also show a peak at higher conductance than the $4.5 \cdot 10^{-5}$ G_0 one. Plateaus at conductance higher than the prevalent one have been observed before for OPE3-SAc [88, 89]. In particular, its intensity correlates with the molecular yield, i.e., the number of traces showing a plateau with respect to the total number of traces and it can be observed in OPE3 with different anchoring groups, albeit with varying intensity across measurements. Its origin is at present not fully understood; a detailed analysis of this aspect lies outside the scope of this chapter. When inspecting individual traces, most show a continuous plateau until the junction ruptures (blue curves in Fig. 4.2b), but not all of them. Breaking traces can exhibit switching, either after an exponential decay (red curves in Fig. 4.2b), or after a plateau with a different conductance (green curves in

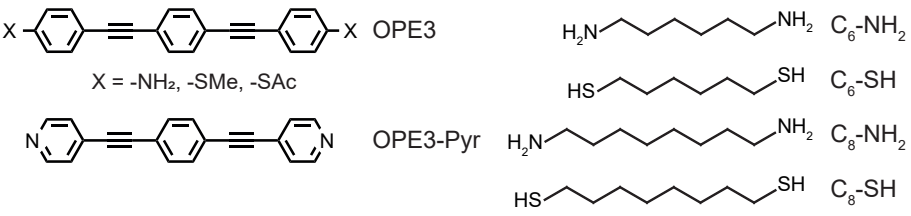

Figure 4.1: Chemical structures of the compounds analysed in this study

Fig. 4.2b). The same behaviours have been reported by others [90, 173, 175].

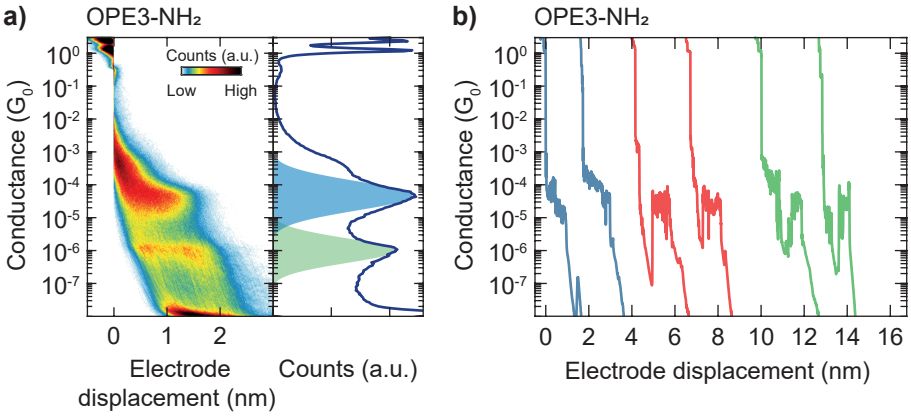

Figure 4.2: a) Two-dimensional conductance-displacement histogram (left) and the corresponding one-dimensional conductance histogram (right) of OPE3-NH_2. The light blue and green shaded areas are the fits to the high- and low-conductance plateau respectively. b) Examples of individual traces showing different behaviours: stable plateau (blue), switching between tunnelling and a molecular plateau (red), and switching between two molecular plateaus (green). Curves are displaced in the x-direction for better visibility.

4.3.1. SWITCHING TRACES CLASSIFICATION

In order to quantify the presence of such switching events, we developed an algorithm that works as follows: the derivative of the conductance is computed in a defined region of interest, and its peaks were identified as possible locations for switching events. Going in order of decreasing peak height, each peak was further analysed by checking the difference in conductance before and after the switch. This was done to avoid noise spikes being detected as switches in conductance. If the difference clears the set threshold, the trace is marked as having a switch, and the displacement at which the peak appears is saved. An example of how the algorithm operates is shown in Fig. 4.3a. For further details on the algorithm we refer to the appendix, Sec. 4.A.1. Notice that we restrict this analysis to the first switch found in each trace. Additionally, in some cases, the conductance switches downwards right before the end of the trace. We exclude this event from our analysis because first it is well discussed in literature [71, 104], and second, we want to focus on the cases in which the conductance is able to switch back to a higher value.

Focusing first on the OPE3-NH_2 measurement shown in Fig. 4.2a, the algorithm found switching events in 22% of molecular traces. Figure 4.3b displays the histograms obtained using only switching traces. The high-conductance plateau built from those has a most probable conductance of $3.9 \cdot 10^{-5}$ G_0. Instead, when considering only traces showing no switch the most-probable conductance is $4.5 \cdot 10^{-5}$ G_0, higher than the one containing the switching traces. This trend is consistent across measurements (Table 4.A2), and with the previous observations by González *et al.* [175].

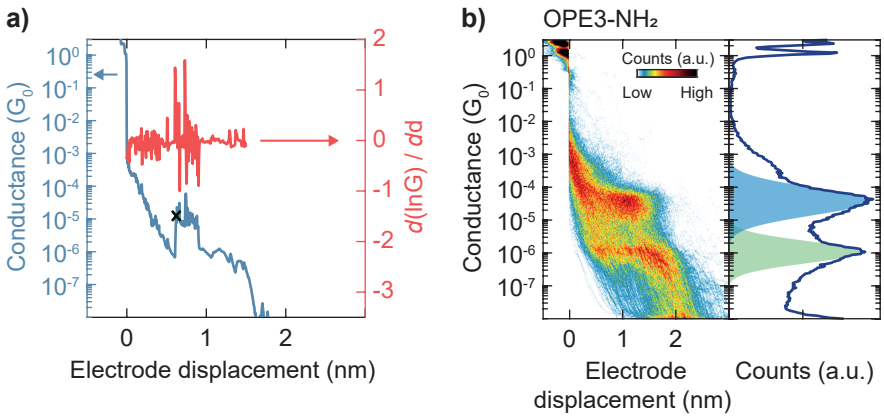

Figure 4.3: a) Illustration of the classification procedure used to separate traces containing switches: in blue, an example of a molecular trace showing a switch, and in red the corresponding derivative used to identify jumps. The black cross identifies the average conductance identified after the jump. b) Two-dimensional conductance-displacement histogram (left) and one-dimensional conductance histogram (right) constructed using only traces that show jumps obtained from the same OPE3-NH_2 measurement shown in Fig. 4.2a.

4.3.2. EFFECT OF THE ANCHORING GROUP

Switching events can be detected across the OPE3s with different anchoring groups, as shown in Fig. 4.4. OPE3-SMe presents a similar behaviour to OPE3-NH_2, meaning that the 2D-histograms built from switching traces are similar to the ones built from raw data. OPE3-Pyr exhibits a different behaviour: the conductance switch happens after an exponential decay, at a well-defined displacement. This is emphasised when considering the master trace, i.e., the trace built using the most probable conductance at each displacement in the 2D-histogram (black lines in Fig. 4.4). The yield of molecular traces with respect to the number of molecular traces is similar among different anchoring groups, with the exception of -SAc anchoring. The latter has a drastically lower probability of showing switching events (Tables 4.A1). The origin of this difference is likely the stronger covalent bonds formed by the thiol groups upon deprotection [48, 57]. Additionally, we observe a large variation of switching probabilities across different measurements of the same molecule. For example, for OPE3-NH_2 this probability ranges from 13% to 52% of molecular traces (Tab. 4.A1).

Traces without switching show a plateau with a higher most-probable conductance than the corresponding one in switching traces: the peak position in the 1D-conductance histogram is 24% higher for OPE3-Pyr, 30% for OPE3-NH_2, 42% for OPE3-SAc, and 59% for OPE3-SMe (Tab. 4.A2). Notice that traces without switching usually have comparable conductance to the raw data. This can be explained by considering that if a trace is switching, it will have fewer counts at the plateau conductance. Hence, in the raw data, the most-probable conductance value will be mostly determined by non-switching traces.

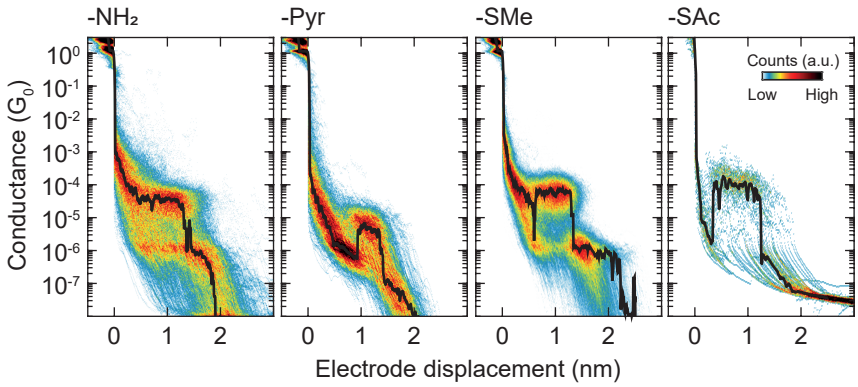

Figure 4.4: Two-dimensional conductance-displacement histograms of OPE3-NH_2, OPE3-Pyr, OPE3-SMe, and OPE3-SAc built using only traces that show switching. The master trace (black line) is superimposed on the corresponding histogram. The yield of switching events is 27% for OPE3-NH_2, 41% for OPE3-Pyr, 16% for OPE3-SMe, and 3% for OPE3-SAc. These values are obtained as average of the most probable conductance value of the measurements at 50 V s^{-1} reported in Tab. 4.A1.

4.3.3. TYPES OF SWITCHING EVENTS

It is possible to distinguish between two types of switching events, as hinted in the previous section: the ones occurring after a steep exponential decay ("tunnelling" switch), and the ones that occur between two different plateaus ("plateau" switch). To better characterize the presence of these types of events in the measurements, we further filter the switching traces by considering the slope of the trace before the switch. In a measurement showing no molecular plateaus, traces with a slope greater than -3 decades nm^{-1} are not expected. Thus, if a molecular trace shows a slope smaller than this value before switching, it is labelled as a tunnelling switch. If the slope is greater, it is considered to be from a plateau.

This procedure allows to track the presence of both types of events in OPE3-SMe (Fig. 4.5a) and OPE3-NH_2 (Tab. 4.A3). Tunnelling switches occur after a defined displacement, which is reflected by the isolated cloud of counts between 0.8 nm and 1.4 nm in Fig. 4.5a (left). This type of behaviour closely resembles that of OPE3-Pyr (Fig. 4.4). On the contrary, the histograms built with plateau switches do not show this cloud-like feature. This hints an interesting behaviour: the junctions first show the slope typical of empty traces. Then, they switch to the molecular feature at a consistent displacement. Because of this, the area in the 2D-histogram corresponding to the plateau appears isolated from the rest.

Increasing the breaking speed from 1 nm s^{-1} to 4 nm s^{-1} does not influence the presence of either type of switching event, nor does it change the displacement at which the switch happens in the tunnelling events (see Fig. 4.5b). This implies that, in the explored stretching rate range, tunnelling switches are not related to time-dependent phenomena, such as thermal adsorption/desorption of the molecule from the electrode. We note that according to previous reports [126] these effects start to be dominant only at stretching rates below 1 nm s^{-1}, or that they are not relevant at all [175].

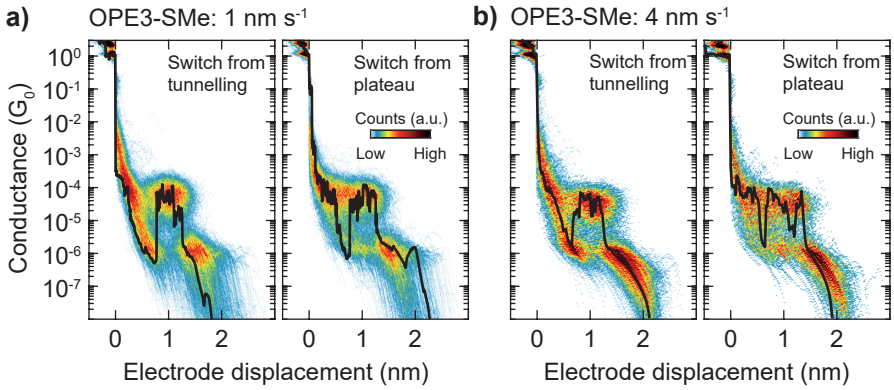

Figure 4.5: Two-dimensional conductance-displacement histograms of switching traces in OPE3-SMe at a) 1 nm s^{-1} and b) 4 nm s^{-1}, divided in traces that show switching starting from tunnelling (left) and ones that show switching starting from a plateau (right). An example trace (black line) of each kind of switching event is superimposed to the corresponding histogram.

A possible explanation for the tunnelling switching is that these are due to a junction forming while separating the electrodes, with molecules initially anchored to only one of them, as illustrated in Fig. 4.6a. Since in the experiments the switch occurs at a well-defined displacement, one can conceive that after this critical displacement is reached, the dangling side of the molecule "snaps" to connect to the other electrode. In this picture, the threshold should correspond to the minimum distance between the free anchoring group of the molecule and the apex of the electrode (i.e., the site at which the driving force for binding is the largest). This is, in principle, a similar mechanism to what drives AFM or STM tips functionalization procedures [181]. However, this explanation is in contrast with a previously reported study in STMBJ [182], where it is found that junction formation happens before rupture of the gold contact. However, it is important to highlight that in this study the measurements were performed in solution. Additionally, the tip-substrate geometry of the STM setup is different from the MCBJ lithographically defined nanowire. These differences could be at the origin of the contrasting results.

Plateau switching suggests that the junction is changing between different configurations. Since there are no intrinsic molecular switching mechanisms in the rigid OPE3 backbone, the most likely explanation is that the contact configuration with the gold surface is changing, as illustrated in Fig. 4.6b, similarly suggested by Kaliginedi *et al.* [104]. We therefore examined the length of the segments in which the junction remains in the low-conductance state, as described in Sec. 4.A.4. Examples of the resulting histograms are shown in Fig. 4.A4. We find that OPE3-NH_2 and OPE3-SMe have a prominent narrow peak at a length of 0.1 ± 0.02 nm and 0.1 ± 0.04 nm respectively. In addition, we also observe broader peaks at 0.3 ± 0.06 nm and 0.3 ± 0.04 nm respectively (Tab. 4.A4). As a first estimate, these values can be compared to the distance between different sites on the gold surface. Considering an Au(111) surface with an interatomic distance of 0.2884 nm [183], there are three types of adsorption sites: on-top, bridge (in-between

two gold atoms), and close packed (surrounded by 3 atoms) [184]. The distance that a molecule needs to cover to move from an on-top site to a bridge one is 0.14 nm or 0.25 nm depending on the direction, while moving to a close packed site requires 0.17 nm.

An alternative explanation for plateau switching is the disconnection (and subsequent reconnection) of one side of a molecule in a π-stacked dimer (see Fig. 4.6b). We cannot exclude this mechanism, however, it is unlikely that an event that causes the rupture of the gold-molecule contact would still preserve the intermolecular geometry. Theoretical studies combining molecular dynamics with transport calculation are needed to reveal the details of the junction evolution.

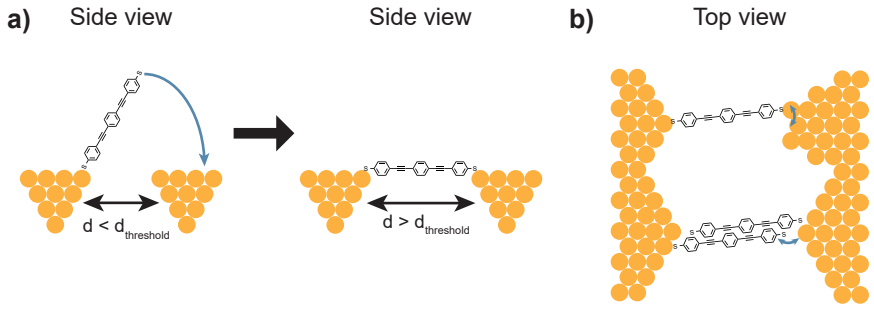

Figure 4.6: a) Illustration of the interpretation for tunnel switching events: the molecule starts only attached on one side, and connects only when a critical displacement is reached. b) Illustration for plateau switching. Either the molecule change binding sites on the surface (top), or one molecule in a π-stacked dimer repeatedly connects and disconnects.

4.3.4. SWITCHING IN ALKANES MOLECULAR JUNCTIONS

We also analysed a set of MCBJ measurements on alkanes previously published by our group [90]. Similar switching behaviour is present in breaking traces of these molecules, albeit they show a much smaller difference between the conductance states before and after the switch compared to OPE3. This is evident from the 2D-histograms shown in Fig. 4.7. The other striking difference between alkanes and OPE3 is that in the former the amount of switching events for the (-SH) terminated compounds is higher than for (-NH_2) (Tab. 4.A1). However, alkanediamines show much clearer switching behaviour in their histograms (Fig. 4.7a and 4.7b). This can have different explanations. Firstly, dithiol-alkanes were measured without the use of a deprotecting agent. This could lead to the presence of weaker bonds to the gold surface [48]. However, this is unlikely to be the only cause. In fact, when measuring OPE3-SAc without deprotecting agent, we find a slight increase of switching events (Tab. 4.A1), but the value is not close to the one observed for OPE3-NH_2. Another explanation stems from the several junction configurations that alkanes are expected to form when bound to gold, such as gauche conformations [71], or chaining of multiple units [85]. This leads to more mechanisms through which the conductance can switch, thus increasing the yield of such events.

The analysed alkane measurements show mostly tunnelling type switching, although the classification is less clear than for OPE3s (see Sec. 4.A.3, and compare Fig. 4.A2 to Fig. 4.A3). The origin of this observation could be purely technical: since hexane and

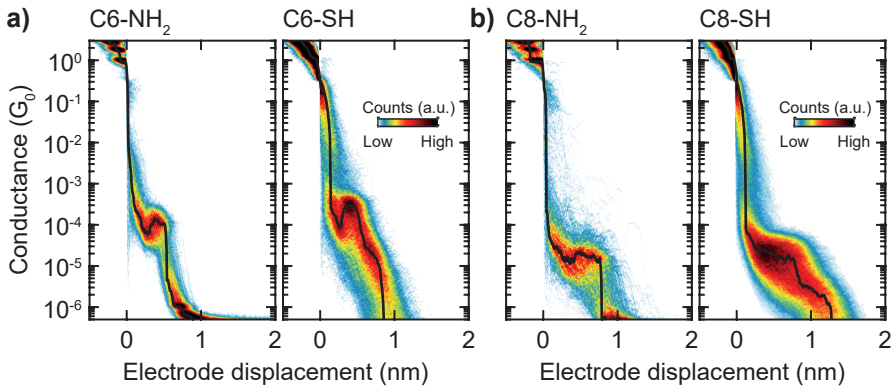

Figure 4.7: Two-dimensional conductance displacement histograms built using only switching traces of a) C6-NH_2 (left) and C6-SH (right), and b) C8-NH_2 (left) and C8-SH (right). The master trace (black line) is superimposed on the corresponding histogram.

octane are relatively short molecules, it is possible that they do not spend enough time in the junction to spontaneously switch between different states, especially considering the measurement speed at which these measurements were carried out. It would be interesting to repeat such measurements with a low measurements speed to see if the presence of plateau switches increases.

Lastly, we analysed the length of the low-conductance segments for plateau switches in alkanes. We find that they show a distribution with one peak at 0.2 nm for all of them (only C6-SH shows a clear additional peak at 0.1 nm, Tab. 4.A4), differently from OPE3s. In terms of displacement, this can still be explained by the switch between different contact sites on the gold surface. However, gauche defects in alkanes are also expected to happen in a similar displacement range [72], making it difficult to disentangle the two phenomena.

4.4. CONCLUSIONS

In conclusion, we identify the presence of switching events in MCBJ measurements of OPE3, hexane, and octane, having different anchoring groups. For OPE3s, we find switching events with a probability ranging from 5% to 52%. However, in the case of OPE3-SAc the amount of switching events can be considered negligible. Additionally, we distinguish between two types of switching. "Tunnelling" switching happens after an exponential decay of conductance typical of empty traces, which suggests the possibility of junction formation after rupture of the gold bridge. "Plateau" switching happens while the trace is already showing a clear molecular plateau right after breaking of the gold contact. These can be related to the junction changing its configuration during the measurement, either to a junction with weaker coupling to the electrodes, or to a π-stacked dimer. This study highlights the necessity to carefully consider the anchoring groups when studying abrupt conductance changes in molecular switches. Acetate protected thiol (-SAc) is confirmed as a stable anchoring option showing no relevant amount of switching. Otherwise, coexis-

tence of contact-dependent mechanisms and chemically introduced backbone-related mechanisms thus requires either careful selection of anchoring groups or one-to-one comparison to reference compounds. Our study gives a perspective for what can be expected from some of the most studied reference molecules.

4.A. APPENDIX

4.A.1. SWITCH IDENTIFICATION ALGORITHM

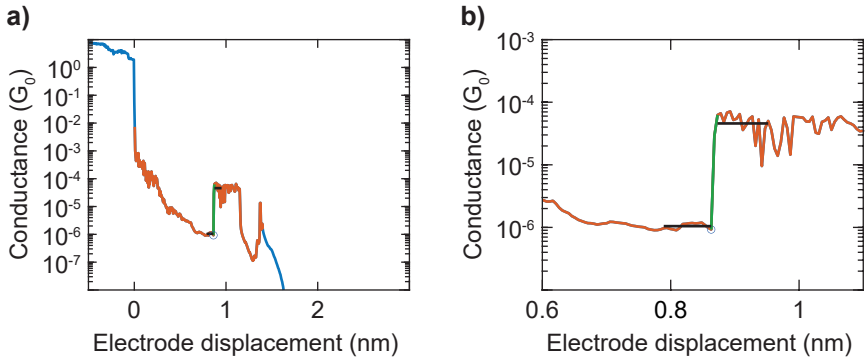

Figure 4.A1: a) Example trace with a conductance switch and b) zoom in of such trace in the region of interest, showing how the algorithm operates. The blue line represents the total trace, while the orange line is the portion of the trace that falls within the defined range. The dark blue open circle is the point that the algorithm identifies as the switch, and the green line is the corresponding conductance switch. The black lines are the average conductance values before and after the switch, extended for the interval that the algorithm is considering to compute them.

The algorithm developed to identify switching events works as follows. First, it defines a region of interest in the trace. This corresponds to a specified range of conductance and displacement (orange line in Fig. 4.A1a). Then, it computes the derivative of the trace in that segment. The low-conductance limit for this region was set as $2 \cdot 10^{-6}$ G_0 for all molecules. The upper conductance limit was set as $1 \cdot 10^{-2}$ G_0 for OPE3s, $2 \cdot 10^{-4}$ G_0 for hexanes, and $2 \cdot 10^{-5}$ G_0 for octanes. The displacement range was 0 nm to 1.7 nm for OPE3s, and 0.2 nm to 1.0 nm for alkanes.

Considering that the highest conductance increases are likely due to a switch, points at which the derivative spikes are considered to be possible switching events, and they are analysed in order of decreasing intensity. Thus, the algorithm considers the position of the highest peak (dark blue circle, in Fig. 4.A1b), and it considers only the section of the trace just before and just after the peak (with a width of around 0.07 nm for OPE3s and 0.025 nm for alkanes), to compute the average conductance of these sections (see black lines in in Fig. 4.A1b).

If the ratio of these conductance values is above a set ratio (5 for OPE3-Pyr, 10 for other OPE3s, and 2 for alkanes), the point is labelled as a switch. This step is necessary to avoid noise spikes being detected as switching events. If the most intense derivative peak fails any of the aforementioned checks, the algorithm iterates through the next peaks until either a switch is found, or a maximum number of iterations is reached (10 iterations). In the latter case, the trace is labelled as "no switch". If a switch is found (green line in Fig. 4.A1b), the algorithm saves the displacement at which it happens, as well as the conductance computed just before and just after the jump.

4.A.2. SWITCHING IDENTIFICATION SUMMARY TABLES

This appendix reports the results for the switching identification algorithms for all the measurements in this study. Notice that, the switching yield is calculated as the number of switching traces with respect to the number of molecular traces. Additionally, for OPE3-Pyr, it was necessary to filter out empty traces to get a reliable estimation of the conductance value. This was done by using an unsupervised learning algorithm as described in Sec 2.2.1. The results obtained in this way are reported in the tables with the label "OPE3-Pyr clustered".

Table 4.A1: Overview of the measurements of all compounds in this study. The measurement number is indicated in the first column by N.

Molecule	N	Number of traces	Piezo speed (V/s)	Electrode speed (nm s^{-1})	Molecular yield (%)	Switching yield (%)	Concentration (μM)
OPE3-NH_2	1	10000	50	1	88	52	100
	2	10000	200	4	40	46	100
	3	10000	50	1	64	16	100
	4	9384	200	5	27	13	100
	5	10000	50	1	55	22	100
	6	10000	50	1	92	18	100
OPE3-SMe	1	10000	50	1	94	18	100
	2	10000	200	4	93	11	100
	3	5000	50	1	93	18	100
	4	5000	200	4	95	11	100
	5	10000	50	1	98	21	10
	6	10000	200	4	84	21	10
	7	10000	50	1	87	8	1
	8	10000	200	3	85	5	1
OPE3-Pyr	1	10000	50	1	58	41	100
OPE3-SAc deprotected	1	10000	50	2	50	1	100
OPE3-SAc protected	1	10000	50	1	24	5	100
C6-NH_2	1	20000	200	5	67	10	1
C6-SH	1	100000	200	5	19	25	1
C8-NH_2	1	20000	200	4	13	27	1
C8-SH	1	100000	200	4	19	44	1

Table 4.A2: Conductance of the measurements of all the compounds in this chapter. The measurement number is indicated in the first column by N.

Molecule	N	Raw Data (G/G_0)	Switching traces (G/G_0)	Non-switching traces (G/G_0)
OPE3-NH_2	1	$8.1\cdot10^{-5}$	$7.5\cdot10^{-5}$	$9.6\cdot10^{-5}$
	2	$4.9\cdot10^{-5}$	$4.6\cdot10^{-5}$	$4.3\cdot10^{-5}$
	3	$4.1\cdot10^{-5}$	$3.2\cdot10^{-5}$	$4.6\cdot10^{-5}$
	4	$2.9\cdot10^{-5}$	$3.2\cdot10^{-5}$	$2.6\cdot10^{-5}$
	5	$4.5\cdot10^{-5}$	$3.9\cdot10^{-5}$	$4.5\cdot10^{-5}$
	6	$8.6\cdot10^{-5}$	$6.9\cdot10^{-5}$	$9.2\cdot10^{-5}$
OPE3-SMe	1	$9.1\cdot10^{-5}$	$6.3\cdot10^{-5}$	$1.0\cdot10^{-4}$
	2	$5.8\cdot10^{-5}$	$3.9\cdot10^{-5}$	$6.3\cdot10^{-5}$
	3	$6.6\cdot10^{-5}$	$4.7\cdot10^{-5}$	$7.1\cdot10^{-5}$
	4	$5.1\cdot10^{-5}$	$3.4\cdot10^{-5}$	$5.4\cdot10^{-5}$
	5	$4.7\cdot10^{-5}$	$3.4\cdot10^{-5}$	$5.3\cdot10^{-5}$
	6	$2.9\cdot10^{-5}$	$2.4\cdot10^{-5}$	$3.1\cdot10^{-5}$
	7	$5.9\cdot10^{-5}$	$3.3\cdot10^{-5}$	$6.4\cdot10^{-5}$
	8	$4.6\cdot10^{-5}$	$2.9\cdot10^{-5}$	$4.6\cdot10^{-5}$
OPE3-Pyr	1	$4.7\cdot10^{-6}$	$5.7\cdot10^{-6}$	$5.3\cdot10^{-6}$
OPE3-Pyr clustered	1	-	-	$7.2\cdot10^{-6}$
OPE3-SAc de-protected	1	$1.6\cdot10^{-4}$	$1.2\cdot10^{-4}$	$1.6\cdot10^{-4}$
C6-NH_2	1	$9.1\cdot10^{-5}$	$1.1\cdot10^{-4}$	$9.2\cdot10^{-5}$
C6-SH	1	$2.3\cdot10^{-4}$	$2.6\cdot10^{-4}$	$2.0\cdot10^{-4}$
C8-NH_2	1	$1.8\cdot10^{-5}$	$1.7\cdot10^{-5}$	$1.9\cdot10^{-5}$
C8-SH	1	$2.2\cdot10^{-5}$	$1.8\cdot10^{-5}$	$2.5\cdot10^{-5}$

4.A.3. TUNNELLING AND PLATEAU SWITCHING CLASSIFICATION SUMMARY TABLES

In this section the results of the analysis done by splitting the switching traces based on the slope of the trace before the switch are presented. Traces whose slope is lower than the threshold (-3 decades nm^{-1}) are labelled as "Tunnelling switch", while the ones that follow a less steep behaviour are labelled as "Plateau switch".

Fig. 4.A2 shows the effect of changing the threshold value for OPE3-SMe as an example. Too small values overestimates the presence of plateau switching, vice versa greater value overestimates the presence of tunnelling switches. The ideal tunnelling switch 2D histogram has the cloud of counts after the switch perfectly isolated from the tunnelling that precedes it. In the ideal tunnelling switch 2D histogram the counts below the main

Table 4.A3: Results of the classification of switching traces in tunnelling and switching events in OPE3-NH_2, OPE3-SMe, C6-NH_2, C6-SH, C8-NH_2, C8-SH. The measurement number is indicated in the first column by N.

Molecule	N	Tunnelling switch G/G_0	Tunnelling switch displacement (nm)	Tunnelling Switch yield (%)	Plateau switch G/G_0
OPE3-NH_2	1	$3.9 \cdot 10^{-5}$	0.77	59	$5.6 \cdot 10^{-5}$
	2	$3.4 \cdot 10^{-5}$	0.80	64	$3.4 \cdot 10^{-5}$
	3	$1.9 \cdot 10^{-5}$	0.74	57	$2.8 \cdot 10^{-5}$
	4	$2.6 \cdot 10^{-5}$	0.63	51	$2.2 \cdot 10^{-5}$
	5	$3.1 \cdot 10^{-5}$	0.81	59	$3.6 \cdot 10^{-5}$
	6	$4.1 \cdot 10^{-5}$	0.65	48	$4.9 \cdot 10^{-5}$
OPE3-SMe	1	$4.4 \cdot 10^{-5}$	0.76	60	$4.6 \cdot 10^{-5}$
	2	$3.3 \cdot 10^{-5}$	0.80	51	$3.4 \cdot 10^{-5}$
	3	$3.2 \cdot 10^{-5}$	0.76	60	$3.5 \cdot 10^{-5}$
	4	$3.1 \cdot 10^{-5}$	0.74	57	$3.3 \cdot 10^{-5}$
	5	$2.5 \cdot 10^{-5}$	0.74	62	$3.0 \cdot 10^{-5}$
	6	$2.3 \cdot 10^{-5}$	0.87	63	$2.7 \cdot 10^{-5}$
	7	$2.8 \cdot 10^{-5}$	0.72	59	$3.1 \cdot 10^{-5}$
	8	$2.9 \cdot 10^{-5}$	0.67	62	$3.5 \cdot 10^{-5}$
C6-NH_2	1	$1.3 \cdot 10^{-4}$	0.36	76	$1.4 \cdot 10^{-4}$
C6-SH	1	$1.2 \cdot 10^{-4}$	0.39	71	$2.0 \cdot 10^{-4}$
C8-NH_2	1	$1.9 \cdot 10^{-5}$	0.49	39	$2.1 \cdot 10^{-5}$
C8-SH	1	$2.7 \cdot 10^{-5}$	0.56	72	$3.0 \cdot 10^{-5}$

plateau would be uniform for all displacements. In our case, the best compromise is obtained with a threshold of -3 decades nm^{-1} (Fig. 4.A2 c).

Alkanes mostly show tunnelling switches, and their separation in plateau vs. tunnelling is not as clear as in the case of OPE3, because of the presence of short plateaus at different conductance levels. Changing the threshold slope does not help in extracting plateau switches (Fig 4.A3). For comparison, we report the results of the classification with a threshold slope of -3 decades nm^{-1}. Notice that also the presence of large conductance spikes after breaking of the 1 G_0 plateau make the classification more difficult. For example, the blue traces of C6-NH_2 in Fig. 4.A3 show these spike, while the yellow traces of C8-SH in the same figure do not.

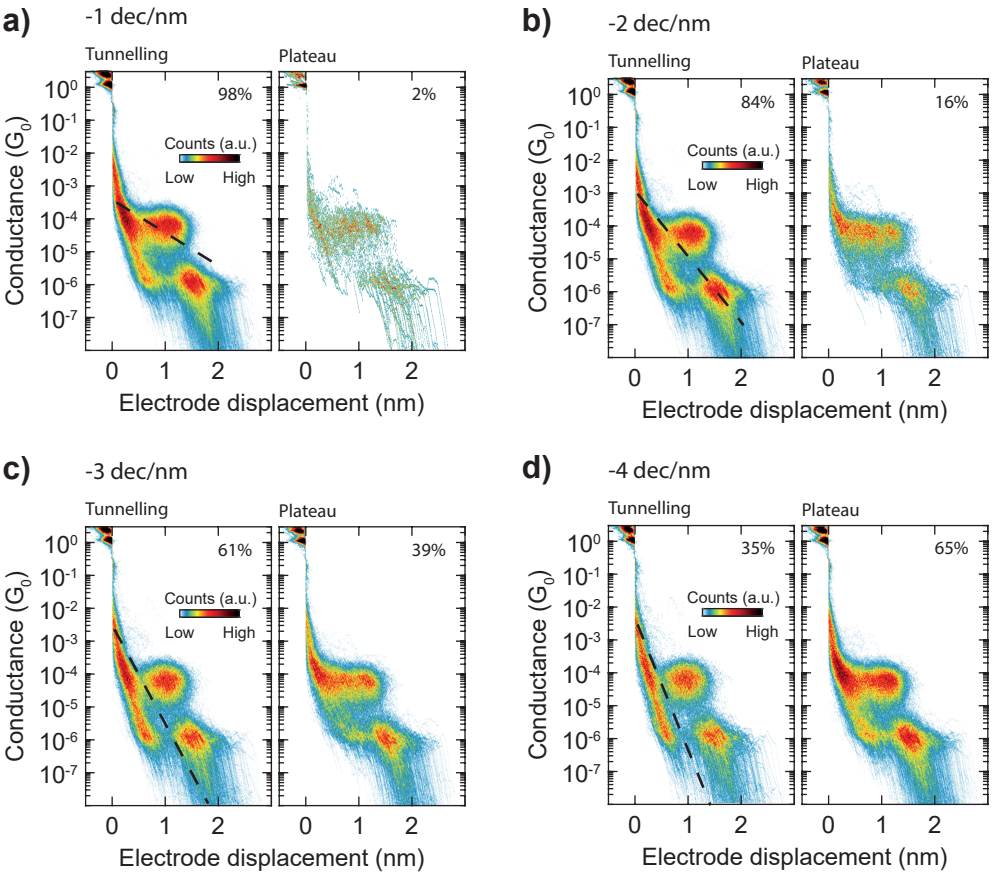

Figure 4.A2: Two-dimensional conductance-displacement of traces with tunnelling switches (left) and with plateau switches (right) from an OPE3-SMe measurement, obtained using different threshold slopes: a) -1 decade/nm, b) -2 decades/nm, c) -3 decades/nm, d) -4 decades/nm. The black dashed line is an eye-guide with the threshold slope used for splitting the two types of traces. The percentages correspond to the yield of tunnelling or plateau switches with respect to the total number of switching traces.

4.A.4. LENGTH OF LOW-CONDUCTANCE SEGMENTS

We further analyse plateau switching by computing the length of the segment of the trace in the low-conductance state. More precisely, we first identify the switching point at which the conductance increases, as described in Sec. 4.A.1. Then we scan the trace backwards, and identify the point at which the conductance increases again (in an analogous way to the downwards shift). Lastly, we compute the difference between the displacements at which the upwards and downwards switch are found. This value corresponds to the length of the low-conductance segment in the trace. Figure 4.A4a displays an example of an histogram built from the values computed in this way for OPE3-NH_2, and Fig. 4.A4b shows the same histogram for C8-SH. For the histograms built from all measurements, we refer to the Supporting Information of the publication this chapter is based on [185].

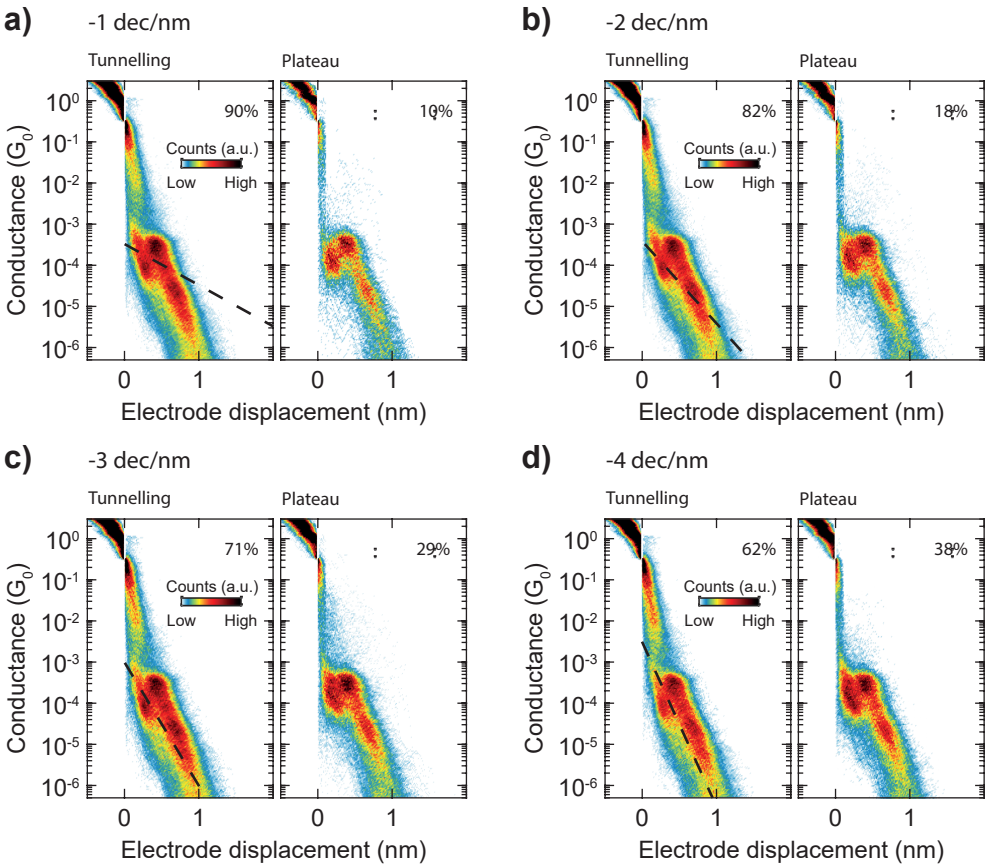

Figure 4.A3: Two-dimensional conductance-displacement of traces with tunnelling switches (left) and with plateau switches (right) from the C6-SH measurement, obtained using different threshold slopes: a) -1 decade/nm, b) -2 decades/nm, c) -3 decades/nm, d) -4 decades/nm. The black dashed line is a eye-guide with the threshold slope used for splitting the two types of traces. The percentages correspond to the yield of tunnelling or plateau switches with respect to the total number of switching traces.

Table 4.A4 lists the centre of the peaks obtained by fitting the histograms with Gaussian distributions. Notice that for the alkanes, segments with length smaller than 0.041 nm were excluded. This allows to avoid the inclusion of conductance spikes happening just after the gold wire ruptures.

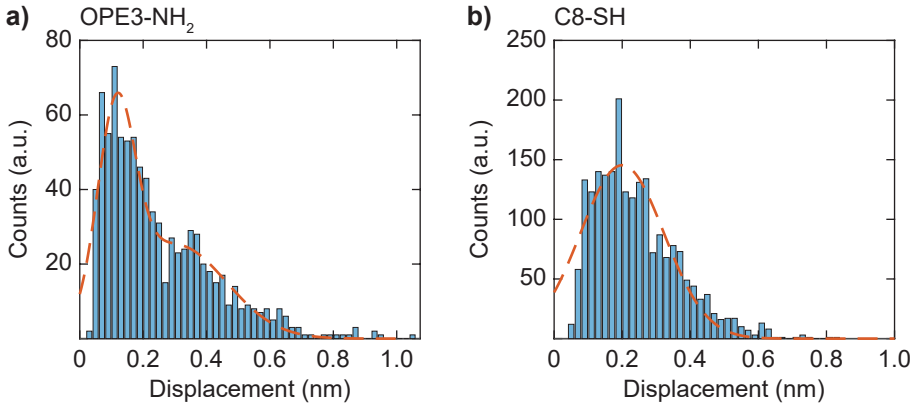

Figure 4.A4: Histograms of the length of the low-conductance segments extracted from a measurement of a) OPE3-NH_2 and b) C8-SAc. The dashes orange line corresponds to a Gaussian fit to the histogram.

Table 4.A4: Fitted length values for the low-conductance segments for OPE3-NH_2, OPE3-SMe, C6-NH_2, C6-SH, C8-NH_2, C8-SH. The measurement number is indicated in the first column by N.

Molecule	N	Peak 1 (nm)	Peak 2 (nm)
OPE3-NH_2	1	0.09	0.26
	2	0.14	0.40
	3	0.14	0.36
	4	-	0.35
	5	0.11	0.21
	6	0.11	0.30
OPE3-SMe	1	0.10	0.34
	2	0.17	0.30
	3	0.09	-
	4	0.18	0.31
	5	0.08	0.22
	6	0.15	0.32
	7	0.06	-
	8	0.11	-
C6-SH	1	0.07	0.22
C8-SH	1	-	0.20
C6-NH_2	1	-	0.19
C8-NH_2	1	-	0.24

5

SIDE-GROUP SUBSTITUTION AND TORSIONAL EFFECTS IN TOLANES

One of the main challenges in molecular electronics is controlling the molecular conductance at the nanoscale. In this chapter, we will explore two approaches based on chemical design that allow to engineer the charge transport in nanoscale molecular junctions. First, the effect of electron-donating and electron-withdrawing side-groups is analysed. Second, we will study the effect of torsion of the molecular backbone. The results shown in this chapter show how structural modification to the molecule can affect charge transport at the nanoscale, but the measured effects are not straightforward to predict.

Parts of this chapter have been published The Journal of Physical Chemistry Letters **13**, 9156-9164 (2022). Some of the measurements were performed by M. Parmeggiani, J. Kamer and C. Bolhuis. The chemical synthesis and characterization was performed by D. Vogel and M. Mayor (Univerity of Basel). STMBJ conductance and thermopower measurements were performed by P. Bastante and N. Agraït (Universidad Autónoma de Madrid). Theoretical calculations were done by A. Daaoub, S. Sangtarash and H. Sadeghi (University of Warwick).

5.1. INTRODUCTION

One of the main challenges of molecular-scale electronics is to engineer and control the charge transport properties at the nanoscale. This is an essential step in reaching the objective of implementing molecules as electronic components [40, 41, 186]. In Ch. 3 we have shown that a possible way to control the conduction is to increase the π-conjugation of the molecule, albeit at the cost of increasing the intermolecular interactions. However, there are additional ways through which the molecular properties can be tuned through molecular design [187], such as by using substituents, or by altering the planarity of the molecular backbone. In this chapter, we will explore these two approaches. First, we will study the effect of electron-withdrawing and -donating side groups (Sec. 5.2 to 5.4). Second, we will analyse the effect of twisting the molecular backbone (Sec. 5.5).

Substituents are key design elements in molecular materials, widely applied in organic semiconductors, photovoltaic, and light-emitting diodes [188]. However, in break-junction based measurements, the role of side groups was often only limited to increase the solubility of the molecule [103, 146, 189]. Thus, side groups are employed that do not have an effect on the molecular conductance. For example, the addition of two methoxy, hexyloxy, alkyl, alkoxy, fluoride or *tert*-butyl groups has no significant effect on the conductance compared to the unsubstituted OPE3 [59, 103, 105, 189, 190]. Although inert with respect to the measured conductance, methoxy side groups have an effect on the Seebeck coefficient, increasing it by $\approx 3\ \mu V\ K^{-1}$ [190]. Side groups can, on the other hand, influence the conductance indirectly, by affecting the conformation of the molecule [191, 192], or by modifying their quantum interference pattern [20, 21, 193, 194]. Lastly, only small variations in conductance were reported for a series of monosubstituted benzene- 1,4- diamines with either electron-donating or electron-withdrawing anchoring groups [195].

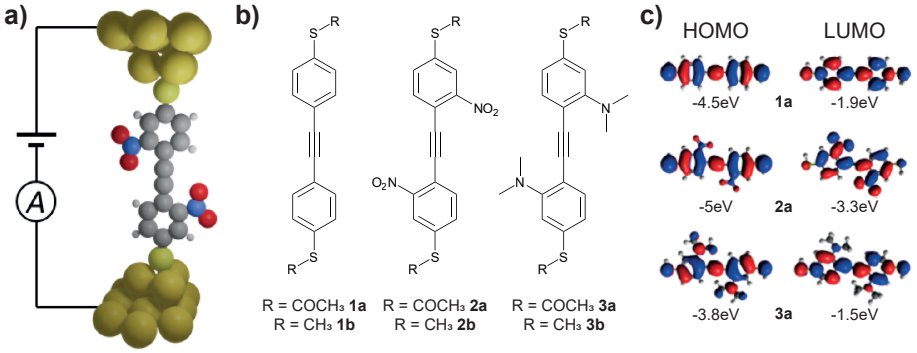

Figure 5.1: a) Scheme of a tolane molecule with a nitro substituent and thiol anchor connected to two gold electrodes. b) Molecular structure of the series **1-3** of tolane model compounds with acetyl (**a**) and methyl (**b**) masked thiol anchor groups. c) Frontier molecular orbitals of **1a**, **2a**, **3a**.

In the following, we will examine the effect of electron-withdrawing and electron-donating substituents in nanoscale molecular junctions, both theoretically and experimentally (Fig. 5.1). For this investigation, the tolane backbone was chosen. It is the smallest structural variant of OPE derivatives (Fig. 5.1a,b), and it is highly conjugated

(Fig. 5.1c), chemically versatile, and it is known to be well behaved in break-junction measurements [196]. For the connection to the gold electrodes, the backbone was terminated with either thiol- (series **a** in Fig. 5.1b) or methylsulfide- (series **b** in Fig. 5.1b) anchoring groups. These two terminations differ in gold-sulfur bond strength (covalent for the former, coordinative for the latter), and in the electronic coupling [57, 197].

To tune the energy level position of the tolane structure (**1**), it was decorated either with electron-withdrawing nitro groups (**2**), or electron-donating dimethylamino groups (**3**), as shown in Fig. 5.1b. The detailed synthetic procedures for obtaining these compounds can be found in the Supporting Information of [198]. Then, we investigate the effect of the substituents on charge transport measurement with the mechanically controllable break junction (MCBJ) and the scanning tunnelling microscope break junction (STMBJ) techniques, as well as in Seebeck coefficient measurements (with the STMBJ). Lastly, a novel statistical approach to model quantum transport is proposed. This allows to predict the trends from the measurement. Furthermore, the method does not treat the electrodes' Fermi energy as a free parameter, avoiding its arbitrary choice in the prediction of conductance values.

5.2. EFFECT OF SIDE-GROUP SUBSTITUTION ON ENERGY LEVEL POSITION

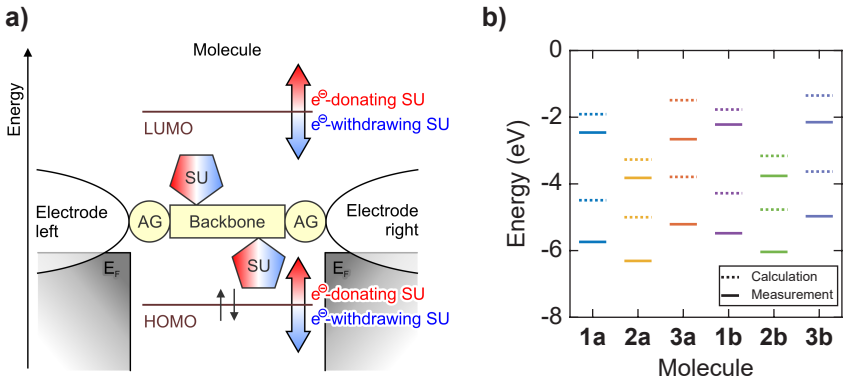

Figure 5.2: a) A simplified scheme of a molecular junction where the molecule's backbone is linked over anchor groups (AG) to the adjacent electrodes. The parent molecule may be decorated by additional substituents (SU), e.g., electron-donating or -withdrawing groups. b) Energy level diagram with HOMO/LUMO levels of the tolanes **1a**, **2a**, **3a**, **1b**, **2b**, **3b**. The solid (dashed) lines show the levels determined by CV (calculations using first principle methods).

The substitution with electron-withdrawing groups, such as nitro (-NO_2), moves the position of both frontier orbitals down in energy [6, 188, 199]. On the other hand, electron-donating substituents, such as dimethylamino [-$N(CH3)_2$], shifts both HOMO and LUMO upwards. We refer to this practice as "frontier orbital engineering" (FOE). The effect is schematically represented for a molecule contacted by gold electrodes in Fig. 5.2a. Both experimental cyclic voltammetry (CV) and first-principle density functional theory (DFT) calculations verify the effect of FOE (Fig. 5.2b), showing the shifts in energy often

exceeding 1 eV. However, there is an offset between the measured and calculated data, which is due to the well-known underestimation of the band-gap by DFT [200]. For the details on the CV and DFT measurements we refer to the Supporting Information of the publication linked to this chapter [198].

5.3. EFFECT OF SIDE-GROUP SUBSTITUTION ON CHARGE TRANSPORT EXPERIMENTS

The charge transport properties of the tolane series were characterised with the MCBJ and STMBJ experiments. The detailed methodologies used for both techniques can be found in Ref. [198]. Briefly, MCBJ measurements were performed as described in Sec. 2.1, after drop-cast of around 5 μL of a 0.1 mM solution of the target compound in dichloromethane (DCM). STMBJ measurements were performed after depositing the molecules from a 1 mM solution in DCM on a preannealed gold surface. A bias voltage of 0.1 V was used for both techniques. The data is then analysed as follows. From the raw dataset, first we remove the empty traces. The methodology to do so in the MCBJ measurement has been described in Sec. 2.2. Then, we apply the *k-means* based clustering procedure (see Sec. 2.2.1) to isolate the different molecular classes in the measurements. The feature space used for analysing these molecules consists of the $30x40$ bins 2D histogram, with limits set as 0 to 1.5 nm in displacement, and -1 to -6 $\log(G/G_0)$ in conductance. The 1D histogram of the trace with 100 bins and limits -1 to -6.5 $\log(G/G_0)$ was also appended to the previous vector, for a total of 1300 dimensions. These parameters were used to cluster both MCBJ and STMBJ traces.

Table 5.1: Average of the most probable conductance values across all the measurements for each molecule, in units of $G_0 \approx 77.5$ μS, for both MCBJ and STMBJ experiments. The columns correspond to the values extracted by fitting the high-conductance (HC) class, and the two low-conductance classes (LC1 and LC2).

Molecule	HC G/G_0		LC1 G/G_0		LC2 G/G_0	
	MCBJ	STMBJ	MCBJ	STMBJ	MCBJ	STMBJ
1a	$1.2\cdot10^{-3}$	$2.3\cdot10^{-3}$	$1.5\cdot10^{-5}$	$3.1\cdot10^{-5}$	$2.3\cdot10^{-6}$	$3.3\cdot10^{-6}$
2a	$1.5\cdot10^{-3}$	$2.2\cdot10^{-3}$	$2.5\cdot10^{-4}$ $3.2\cdot10^{-5}$	$1.6\cdot10^{-4}$ $1.9\cdot10^{-5}$	//	//
3a	$2.2\cdot10^{-3}$	$2.5\cdot10^{-3}$	$6.0\cdot10^{-5}$	$1.6\cdot10^{-4}$	$2.0\cdot10^{-6}$	$2.4\cdot10^{-6}$
1b	$5.9\cdot10^{-4}$	$5.6\cdot10^{-4}$	$1.3\cdot10^{-5}$	$8.3\cdot10^{-6}$	//	//
2b	$7.0\cdot10^{-4}$	$8.4\cdot10^{-4}$	$1.8\cdot10^{-5}$	$3.5\cdot10^{-5}$	//	//
3b	$7.3\cdot10^{-4}$	$8.2\cdot10^{-4}$	$1.1\cdot10^{-5}$	$9.2\cdot10^{-6}$	//	//

The measurements show the presence of high-conductance (HC) and low-conductance (LC) plateaus in all molecules, both in MCBJ and STMBJ measurements. Focusing first on the HC ones, the **a** series shows a most probable conductance above $1\cdot10^{-3}$ G_0, while **b** one have around a factor 2 lower conductance (Tab. 5.1). This decrease is expected due to the weaker electronic coupling to the gold of -SMe compared to -SAc [57]. The HC plateau follows the trend **2a** $\approx$ **1a** $<$ **3a** for -SAc anchoring (Fig. 5.3a,b top left panel), while for -SMe all compounds are within margin of error from each other: **1b** $\approx$ **2b** $\approx$ **3b** (Tab. 5.1,

and Fig. 5.3a,b bottom left panel). We note that a first analysis of the raw data of **2a** did not reveal the high-conductance plateau. This is mainly due to the low percentage of HC traces with respect to LC ones. However, clustering allows to systematically isolate the HC class in all measurements of **2a** (see the Supporting Information of [198], in particular Fig. S2.2, S2.3, S3.3).

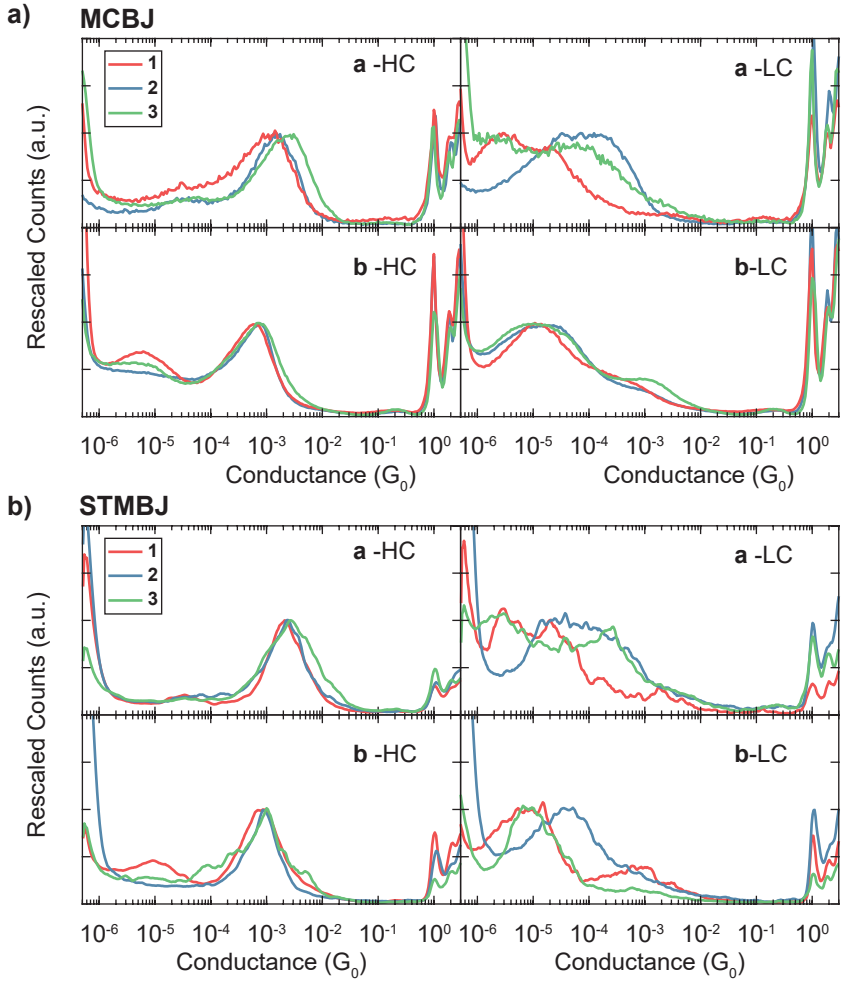

Figure 5.3: a) 1D-conductance histograms for a) MCBJ and b) STMBJ measurements of the HC (left) and LC (right) peaks as obtained from clustering, separated by anchoring group (top: **a**, -SAc, bottom: **b**, -SMe). The measurements have been rescaled by peak height to make the peak position and shape directly comparable across the different molecules.

The low-conductance features show a more diverse behaviour than the HC plateau. Considering the -SAc terminated compounds, they follow the trend **2a** > **3a** > **1a** (top right panel of Fig. 5.3a,b). Further analysis reveals the presence of two types of low-conductance features for the **a** series, as illustrated in Fig. 5.4a: slanted plateaus falling

in the 10^{-5} G_0 range (LC1), and long, flat plateaus in the 10^{-5} G_0 range (LC2). An LC1 feature was measured for all compounds, while LC2 plateaus were measured only in **1a** and **3a**. For **2a**, we observe two types of slanted features, as shown in Fig. 5.4b. One falls in the 10^{-5} G_0 range ($LC1^L$), similarly to the other compounds. The other one has a higher conductance, around 10^{-4} G_0 ($LC1^H$), and slightly shorter traces. As for the **b** tolanes, they all show only LC1 low-conductance features. In MCBJ measurements, all three compounds exhibit very similar conductance (Fig. 5.3a, bottom right panel). However, in STMBJ **2b** has roughly a factor 4 higher conductance than **1b** and **3b** (Tab. 5.1 and Fig. 5.3b, bottom right panel).

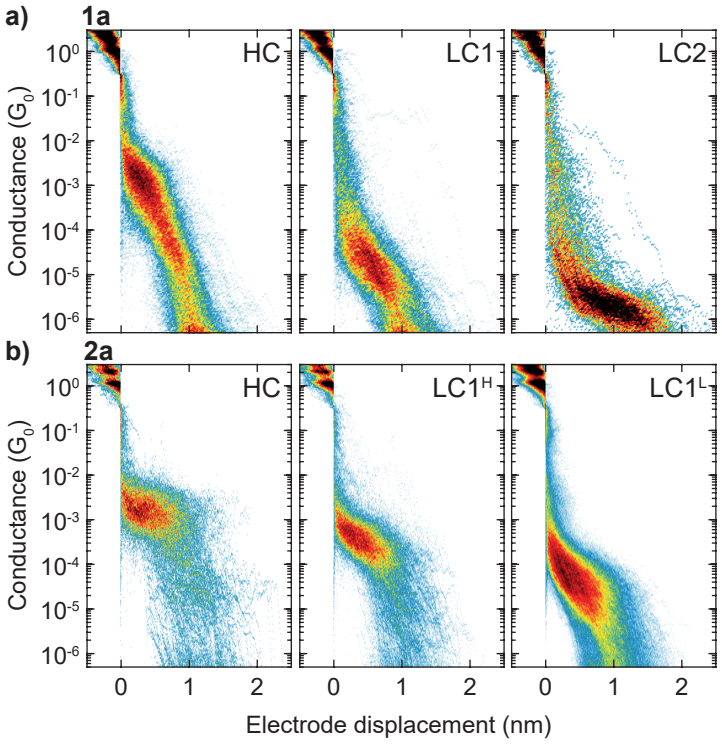

Figure 5.4: Two-dimensional conductance-displacement histograms of molecular classes found through clustering in MCBJ measurements for a) **1a** and b) **2a**. While both show a HC plateau at roughly the same conductance value, they have different LC features.

5.4. DFT CALCULATIONS AND THERMOPOWER MEASUREMENTS

To further comprehend the relation between charge transport measurements and the synthetic addition of substituents, we performed DFT combined with quantum transport calculations [201] using the methodology described in [198]. In this way, the transmission function T(E) for molecules **1**-**3** is obtained. Then, the low-bias conductance is calculated from T(E) through the Landauer formula. Multiple gold-molecule contact configurations

were included in the theoretical analysis, considering that the molecule can bind to the surface by connecting to one, two, or three gold atoms (as shown in Fig. 5.5a).

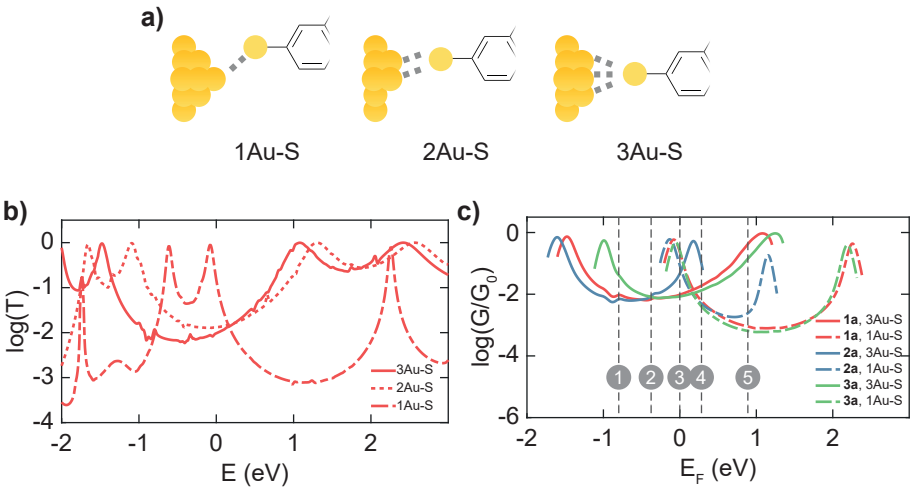

Figure 5.5: a) Molecule/gold contact through one, two, and three gold atoms. b) Example of the transmission coefficient for the molecule **1a** with different contacting conformations to the electrodes. c) Example of the conductance (G) for molecule **1a**, **2a**, and **3a** with different contacting conformations to the electrodes. For clarity, G is shown for the E_F between HOMO and LUMO resonances only. E = 0 eV corresponds to the DFT Fermi energy. The gray dashed lines (marked by 1-5) show examples of the choice of the Fermi energy.

Figure 5.5b shows T(E) for **1a**, in the three contacting modalities. The two and three atom contacts have relatively similar transmission, with a slight shift to more negative energies for the latter. However, the one-atom contact exhibits significant deviations: the position of the resonance peaks is at more positive energy than for the other two contacts, and the minimum of T(E) in the HOMO-LUMO gap is lower. Figure 5.5c compares the calculated conductance for **1a**, **2a**, and **3a**. For the 3-atom configuration, the curve shifts similarly to what is expected from the CV experiments and DFT calculations for the isolated molecules: **3a** moves to higher energy with respect to **1a**, while **2a** changes to lower energy. However, the 1-atom contacted molecule displays almost overlapping conductance curves for **1a** and **3a**, while **2a** shows a deviation close to the LUMO. This suggests that the conductance trend in the measurements might differ depending on the contact configuration. In addition, the predicted substituent effect strongly depends on the choice of the Fermi level. To illustrate this, let us consider a few possible choices, marked by dashed lines in Fig. 5.5c. At the energy marked by 1, we find the trend **2a** ≈ **1a** < **3a**. At the point marked by 2, all three compounds have the same conductance, while around energy 3 we find **2a** < **1a** ≈ **3a**. These differences make prediction of molecular conductance a difficult task [73, 202, 203].

In the following, a new analysis method for quantum transport calculation is proposed. This procedures allows to minimize the ambiguity in the Fermi energy choice. Furthermore, it allows to predict the small experimentally observed variations in electrical conductance caused by nitro and dimethylamino substitution (Tab. 5.1). The first step

is to calculate the electrical conductance for a wide variety of electrode conformations, obtained by increasing the molecule-electrode distance. The resulting calculations are shown in Fig. 5.6, for all compounds. Then, conductance histograms are created using the calculated conductance curves, by considering a wide range of E_F within the HOMO-LUMO gap. The peaks in the conductance histogram are fitted with a log-normal distribution, and their centre is the most-probable calculated conductance. The goal of the first step is to incorporate in the conductance prediction conformations that are accessed during the measurements due to the dynamic nature of the traces in break-junction measurements. The second step has a double-fold objective. First, it takes into account fluctuations in the alignment of the molecule's energy levels with the Fermi energy [204–206]. Second, it groups the data in a single plot, analogously to how the experimental data is used to compile 1D-conductance histograms. The restriction to the energy range delimited by the HOMO and the LUMO is based on the assumption of non-resonant charge transport.

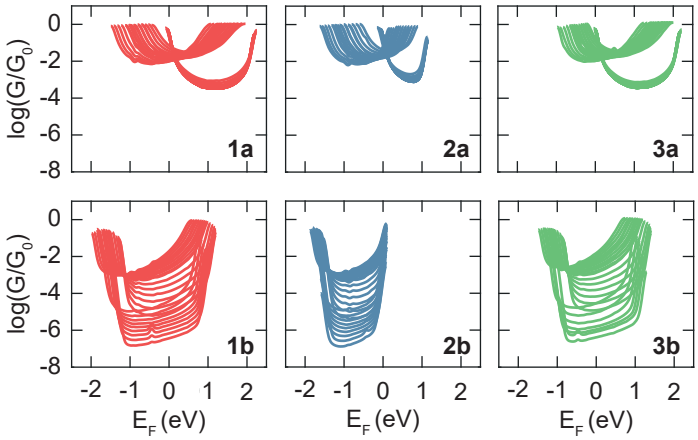

Figure 5.6: Calculated conductance for molecules **1**, **2**, and **3** with different anchor groups and contacting conformation to the electrodes. G is shown for the E_F between HOMO and LUMO resonances only.

The histograms calculated through the theoretical analysis are shown in Fig. 5.7a,b. The conductance of -SAc terminated compounds is higher than the -SMe terminated counterparts, in agreement with the experiments. Additionally, there are multiple conductance peaks in the computed histograms: the low-conductance ones originate from molecules contacting the electrodes through a single gold atom, while the high-conductance ones correspond to contacts formed with more than one gold atom. The former is compatible with the LC1 features in the experiments, while the latter is consistent with the HC peak in the experimental 1D-histograms (Tab 5.1 and Fig. 5.3a,b). Importantly, notice how for the **a** series the high-conductance peaks overlap for both the calculations and experiments, with compound **3a** having a moderately higher conductance than the other two. Also, the low-conductance peak of **2a** in Fig. 5.3a is slightly higher than for **1a** and **3a**, in agreement with the experiments.

An additional explanation for the low-conductance features is the presence of π-

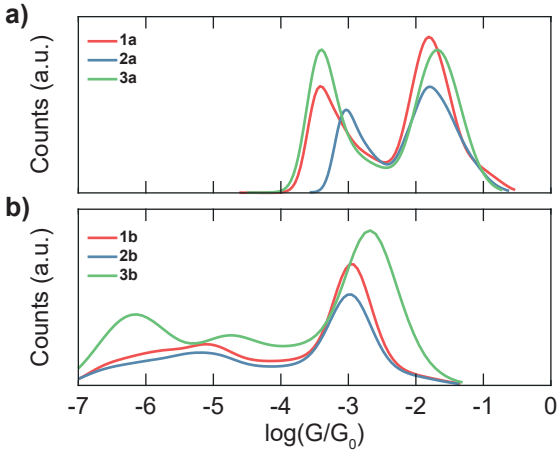

Figure 5.7: Conductance histograms based on the conductance in 5.6 for a wide range of Fermi energies within the HOMO-LUMO gap for a) **1a**, **2a**, and **3a** and b) for **1b**, **2b**, and **3b**.

stacked molecules in the junction [81, 82, 103]. These effects are not included in the calculations shown in Fig. 5.3. According to first-principle calculations (see Fig. S4.3 of [198]), the conductance of π-stacked dimers is even lower than the LC peak in Fig. 5.3, and it would give rise to an additional peak in the histogram. Additionally, traces corresponding to π-stacked dimers are expected to be longer than those of non-interacting molecules. Thus, this explanation fits well the LC2 features measured for **1a** and **3a** (Tab. 5.1 and Fig. 5.4). However, we note that such features were not observed in **2a**. Notice, Fig. 5.7b has one discrepancy with the measurements: the peaks for **3c** have higher conductance for than **3a** and **3b**. Interestingly, the more conductive electrode conformations that give rise to this shift are all at long displacements, i.e., when the junction is very stretched. However, it is possible to reasonably assume that such conformations do not arise in the measurements, since the weak bonding of -SMe group would rupture before. If such conformations are removed in the construction of the theoretical histograms (see Fig. S4.7 of [198]), the three compounds are predicted to have similar conductance.

Lastly, let us explore further the effect of NO_2 substitution. Figure 5.2b and Fig. 5.6 indicate that, when this substituent is used, the LUMO of the molecule substantially decreases with respect to the parent tolane. This effect arises from the introduction of a new energy level in the molecule because of the presence of the substituents. The level for NO_2 falls within the HOMO-LUMO gap of the unsubstituted compound [198, 207]. The additional resonance caused by it is visible in the transmission of both **2a** and **2b**, and when considering either the single Au atom contact, or the multiple atom contacts (Fig. 5.5c and Fig. 5.6). However, when considering the multiple electrode conformations and the wide range of Fermi energies, the potential conductance increase is lost for **2b**, while for **2a** it only survives for the one-atom contact (Fig. 5.6). As a result, the histograms of **2a** and **2b** in Fig. 5.7 overlap with those of **1a** and **1b** respectively, with the exception of the low-conductance peak in **2a**.

However, the significantly shifted LUMO is expected to have still have an effect on

transport properties, in the form of a negative shift of the Seebeck coefficient. In fact, this quantity is proportional to the additive inverse of the derivative of the transmission function at the Fermi energy [208]. To verify this hypothesis, Seebeck coefficient measurements were performed with the STMBJ technique (experimental details can be found in [198]). The resulting Seebeck coefficient for each class is reported in Tab. 5.2. Overall, -SAc terminated molecules show more positive Seebeck than their -SMe counterpart. More importantly, compound **2a** shows a negative Seebeck coefficient while **1a** and **3a** have a positive coefficient. Similarly, **2b** exhibits a more negative Seebeck coefficient than **1b** and **3b**.

Table 5.2: Average Seebeck coefficient with the corresponding standard deviation in all thermopower measurements for each molecule.

Molecule	Total Seebeck (μV K^{-1})	HC Seebeck (μV K^{-1})	LC1 Seebeck (μV K^{-1})
1a	+1.7 ± 0.1	+1.6 ± 0.2	+2.8 ± 0.4
2a	-1.4 ± 0.1	-0.8 ± 0.1	-1.6 ± 0.1 -2.6 ± 0.1
3a	+1.7 ± 0.1	+2.1 ± 0.2	-0.1 ± 0.2
1b	-0.4 ± 0.1	-0.4 ± 0.1	-0.7 ± 0.2
2b	-5.2 ± 0.1	-4.3 ± 0.1	-6.2 ± 0.1
3b	-0.2 ± 0.1	-0.5 ± 0.1	+0.4 ± 0.2

5.5. EFFECT OF THE TORSION ANGLE ON CONDUCTANCE OF TOLANES

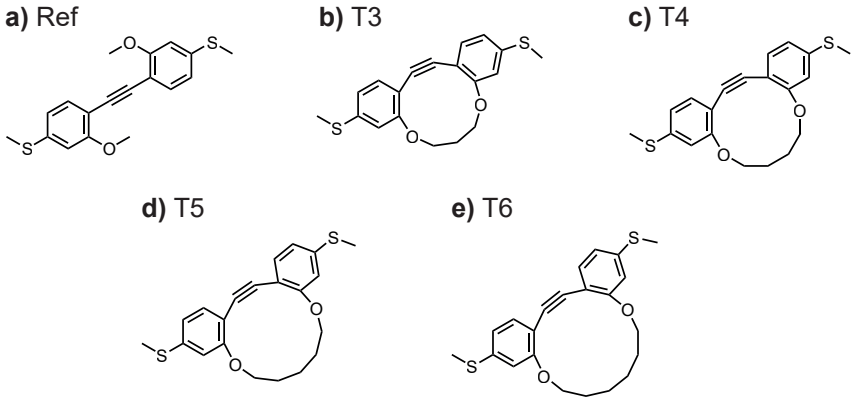

Figure 5.8: Chemical structure of the twisted tolane derivatives. a) Reference compound (Ref, no forced twisting), and b-e) tolanes with alkane linkers with a length ranging from 3 (T3) to 6 (T6) CH_2 segments.

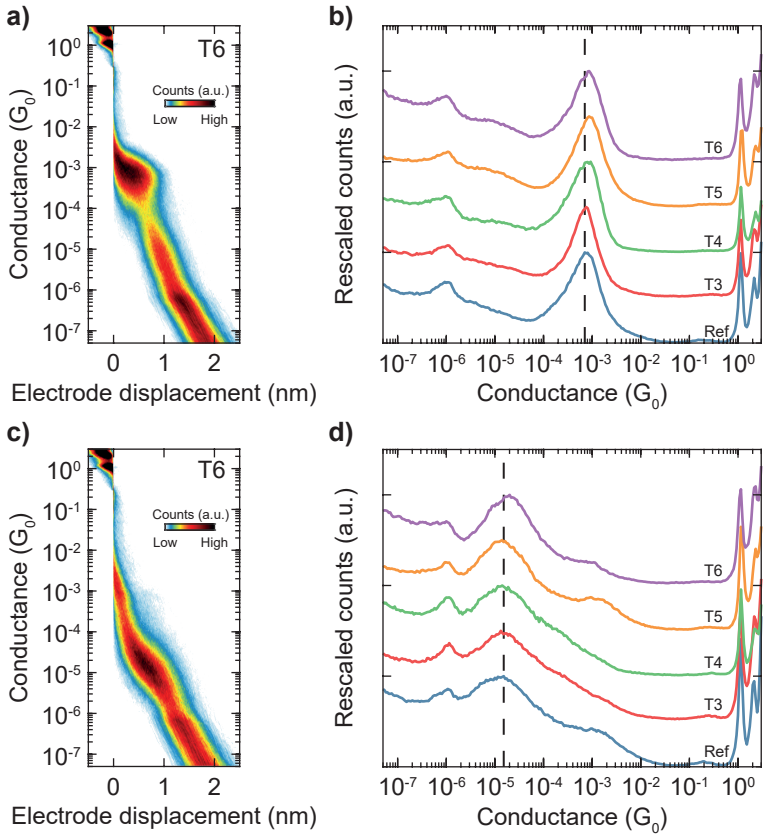

Figure 5.9: a) 2D-histogram of the high-conductance class built from all T6 measurements. b) 1D-histograms of the high-conductance class for all the twisted compounds and the reference, built using all the measurement of each. Counts have been rescaled by peak height to make the peak position and shape more comparable across the different molecules and measurements; the histograms have been displaced vertically for clarity. c) 2D-histogram of the low-conductance class built from all T6 measurements. d) 1D-histograms of the low-conductance class for all the twisted compound and the reference, built using all the measurement of each. Counts have been rescaled by peak height; the histograms have been displaced vertically for clarity. The dashed black lines are eye-guides centered at the conductance value of the reference compound. The small peak at around 10^{-6} G_0 is an artefact from the amplifier (see Sec. 2.3.1).

The effect of torsion angle (ϕ) on molecular conductance has been widely studied in literature as a strategy to tune the molecular conductance by acting on the conjugation of the backbone. Venkataraman *et al.* [179] first reported that in bipyridine derivatives, the molecular conductance is linearly dependent on $cos^2\phi$. They link the explanation of this dependence to the decrease of the conjugation between the two aromatic rings as the angle between them is increased. Later, Mishchenko *et al.* [191] demonstrated that the same dependence is obtained in biphenyl derivatives, and that the $cos^2\phi$ law can be reproduced in a double level model in which a state lies on each benzene ring, with electrons tunnelling from one side to the other. A similar localization has been shown to

tune the conductance in longer aromatic molecular wires [209]. Additionally, Hendon *et al.* [210] calculated that the π-orbitals of allene and oligoyne based wires form helices upon torsion of their termination. The calculated transmittion consequently depends on torsion angle [211]: oligoynes show a dependence that is similar to that of biphenyl, while cumulenes markedly differ from it. Considering these results, it is to be expected that tolanes, upon torsion, would show a linear decrease in conductance with the squared cosine of the torsion angle. To investigate this approach, a series of five tolane derivatives was synthetised[1], using alkoxy chains of increasing length in the attemp to increase the angle between the two aromatic rings (Fig. 5.8). A similar approach was show to induce twisting in tolanes without thiomethyl anchoring [212, 213].

We characterized the charge transport properties of the series of twisted tolanes using the MCBJ technique, analogously to what described in Sec. 2.1. The concentration of the molecular solution used in these measurements was 50 μM, lower than the one for the substituted tolanes. This was done to reduce the yield of molecular traces in the measurement, as the measurements of the **b** series compound in Sec. 5.3 all show yields above 50% (see S2.1 of [198]). After clustering, we found that all the compounds of Fig. 5.8 show high-conductance (HC) and low-conductance (LC) plateaus, analogously to the **b** series of substituted tolanes presented earlier in this chapter. As an examples, Fig. 5.9a,c shows the 2D-histograms of the classes obtained for T6. The 2D-histrograms for all compounds are shown in the appendix (Fig. 5.A1 and Fig. 5.A2). Notice, that these histograms are built by using all the measurements of T6 together. To avoid glitches in the histograms due to differences in attenuation factors between the different measurements, the traces have been interpolated with 1000 points in the displacement interval -1 nm to 2.5 nm. This procedure ensures that all measurements have the same number of points per nm.

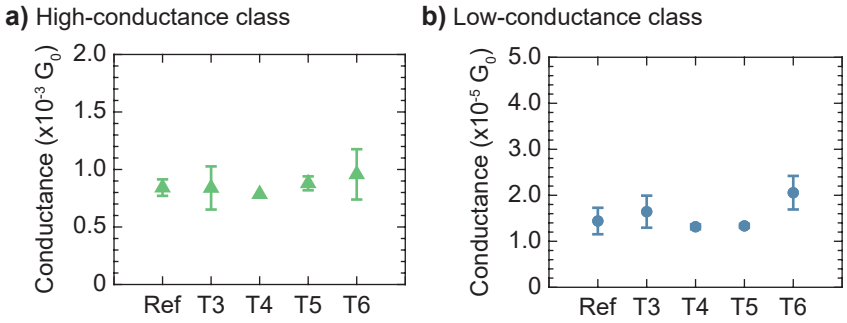

Figure 5.10: Average conductance value and its standard deviation (error bar) for the a) high- and b) low-conductance classes. Notice that a linear scale is used for these plots.

For the reference compound, we identify a most probable conductance of $8.4 \cdot 10^{-4}$ G_0 for the HC class, and $1.4 \cdot 10^{-5}$ G_0 for the LC one. These values are similar to the ones obtained for the substituted compounds **2b** and **3b** in Tab. 5.1, highlighting a slight electronic effect of the side groups. However, the twisted derivatives T3 to T6 do all show

[1] Chemical synthesis by D. Vogel and M. Mayor (University of Basel).

almost identical histograms for both the high- and low-conductance classes, as shown in Fig. 5.9b,d respectively. Even when plotting the conductance values on a linear scale, as in Fig. 5.10, no significant trend can be observed. In fact, not only there is no defined trend across the series, but the conductance values are within error of each other, indicating no effect of the increasing length of the side groups.

This phenomenon could have two explanations. On one side, it could be that the torsion angle has no effect on the conductance of tolanes, in contrast with biphenyl and bipyridine [179, 191] measurements, and despite the prediction that oligoynes should show the same dependence as them [211]. On the other side, it is possible that the twisted tolanes do not have the hypothesized torsion angle. This explanation is consistent with the observations of Menning *et al.* [212], who reported no difference in absorption and emission spectra of similar twisted tolanes, in solution at room temperature, when connecting the two aromatic rings with a simple alkoxy chain compared to the planar compounds. This similarity was measured despite the crystallographic structures of the compounds showed clear difference in torsion angle. Additionally, they found that the difference expected from the solid-state structures is retrieved at low temperature. This hints that tolanes can easily rearrange their torsion when enough thermal energy is provided. The same mechanism could be at play for MCBJ measurements, where the identical conductance of the series T3-T6 might indicate that all the compounds have similar torsion angle because of thermal activated reconfigurations of the molecule. Undoubtedly, theoretical calculations and further experiments, involving for instance temperature dependence of the conductance, could further shed light on the nature of the observed trend.

5.6. CONCLUSIONS

In summary, we studied the effect of electron-donating and electron-withdrawing side groups on the conductance and Seebeck coefficient of nanoscale gold-molecule-gold junctions formed by tolane derivatives. Additionally, a new data analysis procedure for theoretical calculation has been proposed and applied to explain the experimental data. We found that (1) the measured conductance values are in good agreement between the two break-junction techniques; (2) the proposed theoretical methodology is able to predict the measured experimental trends, while minimizing the arbitrary choice of the Fermi energy; (3) electron-donating and electron-withdrawing groups can be used to tune the conductance of a molecule, although the effect can be small and not straightforward to interpret; (4) the addition of nitro groups introduces a resonance in the HOMO-LUMO gap of the parent tolane, leading to a negative shift of the Seebeck coefficient, while the dimethylamino group has no measurable effect on it.

Lastly, we tackled the possibility of tuning the conductance of tolanes through twisting of the molecular backbone. Contrary to previous reports on bipyridine and biphenyl molecules, we did not find any trend of the conductance by using longer side chains to force a twist of the aromatic rings relative to each other. A possible explanation of this observation is that the tolanes all show similar torsion angle due to thermally activated reconfigurations of the molecule. However, further studies are needed to fully understand this phenomenon.

5.A. APPENDIX - 2D-HISTOGRAMS OF TWISTED TOLANES

This section reports the 2D-histograms of the high- and low-conductance classes for the twisted tolanes, and the reference. Analogously to the 1D-histograms in Fig. 5.9b,d, the 2D-histograms do not show clear differences among the measured compounds.

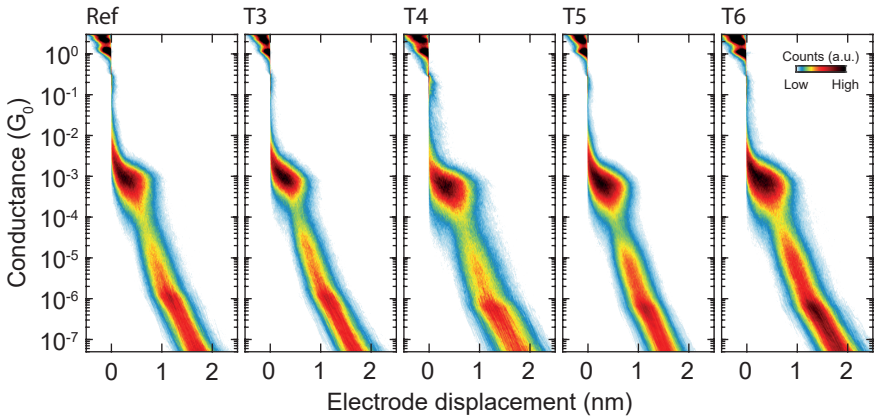

Figure 5.A1: 2D-histogram of the high-conductance class built from all measurements of the reference compound, and of the series of twisted tolanes T3-T6.

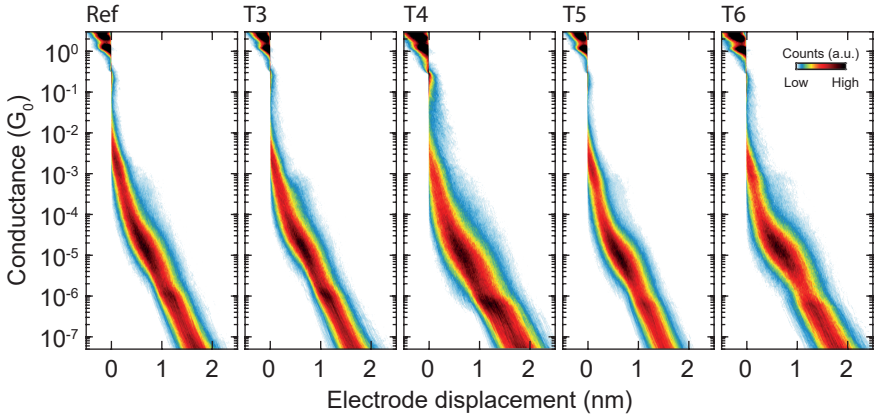

Figure 5.A2: 2D-histogram of the low-conductance class built from all measurements of the reference compound, and of the series of twisted tolanes T3-T6.

6

HIGH-BIAS BEHAVIOUR OF NANOSCALE MOLECULAR JUNCTIONS

Break-junction measurements are often performed at low bias. However, applying larger voltages to a molecular junction allows to access a wider range of the transmission of the molecule, and it enables voltage-driven switching mechanisms. In this chapter, we report how voltage can be exploited to obtain more information on the charge transport of macrocyclic molecule. Then, we characterize two molecular systems that are expected to exhibit voltage-induced switching.

Parts of this chapter have been published in The Journal of Physical Chemistry C **126**, 8801–8806 (2022).

6.1. INTRODUCTION

The characterization of break-junctions is typically performed at low bias, so that the molecule's energy levels lie well outside the bias window. So far in this dissertation, the measurements were performed at 0.1 V bias, complying with this rule. However, there are several physical effects that become visible at higher bias. First, applying a larger voltage allows to explore a wider range of the transmission function of the molecule, possibly reaching resonance with one of the frontier energy levels. This is critical when performing current-voltage characteristics, and for transition voltage spectroscopy [55, 56, 214–216]. Second, it enables to exploit voltage driven switching effects [23, 217–221]. In this chapter, we will explore the charge transport properties of different classes of molecules, by exploiting conductance measurements at voltages higher than 0.1 V. In Sec. 6.2 we will analyse macrocyclic molecules that are expected to show destructive quantum interference. Then, in Sec. 6.3 and 6.4 we will evaluate the voltage induced switching of two classes of compounds: a hydroxyphenalenone based three-state molecular switch and a Norbornadiene–Quadricyclane based compound. The results shown in this chapter are from ongoing studies, and thus do not show definitive conclusions at the current stage.

6.1.1. METHODOLOGY

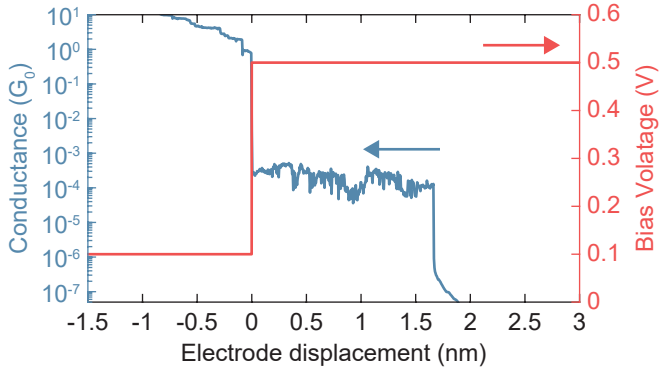

Figure 6.1: Breaking trace (blue line) recorded during the high-bias measurement protocol. The bias voltage for each point is shown in red.

Applying a bias up to around 0.3 V would be possible with the standard measurement procedure. However, when increasing the voltage further, it is possible to induce electromigration of the gold contact [222]. Such a breaking mechanism is undesirable while performing MCBJ experiments and usually leads to junctions uncontrollably breaking to the noise floor. To avoid this effect, it is possible to break and make the junction using a smaller voltage (0.1 V), and to only apply the larger one while measuring the open gap. This process is illustrated in Fig. 6.1. The cycle starts with the junction fully made, while measuring at a small bias (0.1 V). Then, the junction is stretched as in the standard measurment procedure. After the conductance drops below a threshold of 0.3 G_0, i.e., the gold atomic point contact is fully broken, the bias is ramped to a higher value (0.5 V in this example), while keeping the electrodes stationary. Then, the stretching

process is continued until full extension of the gap. Lastly, the bias is ramped down to the initial value (0.1 V), before making the junction again. Using the 0.1 V bias during the the high-conductance part of the breaking cycle (and for the making cycle) has an additional benefit. It allows to use the calibration of the amplifier described in Sec. 2.3.1 for resistances <1 kΩ, which is only valid at 0.1 V bias.

6.2. OPE-BASED MACROCYCLES

6.2.1. INTRODUCTION

Quantum interference effects are one of the most effective strategies to tune charge transport. They arise from the interference of electron waves travelling through different pathways [223]. The most simple molecular system that exhibits this effects is a single benzene ring, when connected to metal electrodes through conjugated chains [224, 225]. The two pathways correspond to two molecular energy levels. When the aromatic ring is connected in *para* configuration, the wave functions corresponding to the frontier energy levels are in phase, resulting in constructive interference. On the contrary, when the connection is through the *meta* (or the *orto*) configuration, these two energy levels are out-of-phase, leading to a characteristic dip in the transmission as a function of energy, and in the suppression of the current flowing through the molecule [30–32, 226, 227].

Controlling the quantum interference pattern in molecules has thus become one of the main objectives of molecular electronics. Several strategies can be found in literature. For example, cross-conjugated molecules have been shown to exhibit quantum interference phenomena [163, 228–230], which can be controlled by reduction/oxidation of the compound [20, 21, 231]. Another approach consists in using heteroatoms in aromatic structures and controlling their position [232–235]. It is also possible to tune the quantum interference of a molecule in a continuous manner: through electrochemical gating [132, 236], or by mechanical manipulation of the molecule [82, 172, 237].

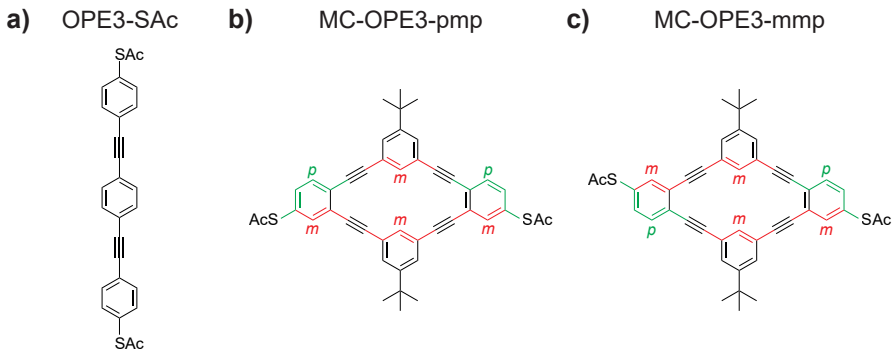

Figure 6.2: Chemical structure of a) OPE3-SAc, b) the macrocycle with *para-meta-para* connections (MC-OPE3-pmp), and c) the macrocycle with *meta-meta-para* connections (MC-OPE3-mmp). The *meta* connections are indicate in red (*m*), the *para* ones in green (*p*).

A different approach to introducing quantum interference in a molecule consists in using multi-branched molecules, in which each branch introduces additional pathways

that can interfere with each other [58, 238]. This concept has been experimentally demonstrated in short cyclic molecules [239–241]. However, it has only been marginally explored in conjugated macrocyclic molecules [242, 243].

In this section, we will analyse the charge transport properties of OPE3-based macrocycles. The chemical structures of the compounds[1] are shown in Fig. 6.2. For reference, we will first report the high-bias behaviour of the well-known OPE3-SAc molecule with all *para* connections (Fig. 6.2a), which is not expected to have any destructive interference phenomena [234, 244].

The macrocycles consists of two branches, each one having a *meta* connected benzene. The connection to the electrodes is then realised in two different ways. In one case (Fig. 6.2b), the top-branch has *para* connections on both sides of the molecule. The bottom-branch has *meta* connections, as indicated in Fig. 6.2b. The second molecule (Fig. 6.2c) has the top-branch connected with the *meta* configuration to one electrode, and *para* to the other. We will refer to the compounds based on the connections that the top-branch presents (MC-OPE3-pmp and MC-OPE3-mmp respectively). In this case, the bottom-branch has the same connectivity, although in reverse order. The combination of the presence of two branches, in addition to the different connectivity to the electrodes, is expected to give different interference patterns for each of the macrocycles.

6.2.2. EXPERIMENTAL RESULTS

We characterized the charge transport properties of the two macrocycles using the MCBJ technique. The resulting measurements were classified using the clustering technique described in Sec. 2.2.1, using the parameters reported in Sec 6.A.1.

We first used the standard 0.1 V bias setting. The 2D-histograms resulting from these measurements are shown in Fig. 6.3. Both molecules show two classes: one having a well defined low-conductance plateau (Class 1), and one with traces spanning a wide range of conductance (Class 2). In this analysis, we will focus on the first class. Notice, that MC-OPE3-pmp exhibits a flat plateau, while MC-OPE3-mmp has a more slanted one. We opted to avoid dividing Class 2 further, since this class already has low yield, and further subsets of it are likely to be statistically unimportant. More details on the measurements can be found in Tab. 6.A1.

Figure 6.4a shows the 1D-histograms for the two macrocycles, with the corresponding log-normal fit. MC-OPE3-pmp has a conductance value of $2.1{\cdot}10^{-6}$ G_0, and a plateau length of around 1.2 nm. Although this conductance value is much smaller than the one of *para*-OPE3 ($\approx 1{\cdot}10^{-4}$ G_0, see Ch. 3, Fig. 6.4b, Tab. 6.A1, and Ref. [57, 148, 223, 234]), it is comparable with values of *meta*-OPE3 found in literature [234]. MC-OPE3-mmp has a conductance value of $4.6{\cdot}10^{-7}$ G_0, a factor 2 lower than the pmp-compound, indicating that the position of the anchoring group has an influence on charge transport in these molecules.

To better highlight the role of quantum interference in these compounds, we investigated the voltage dependence of the conductance. As a reference, we performed measurements of OPE3-SAc at 0.1, 0.5, and 1.0 V bias. The 2D-histograms of these measurements are shown in Fig. 6.A2 while the corresponding 1D-histograms are compared

[1] Chemical synthesis of the macrocycles by A. Gallego and of OPE3-SAc by P. Zwick, both in the group of M. Mayor (University of Basel).

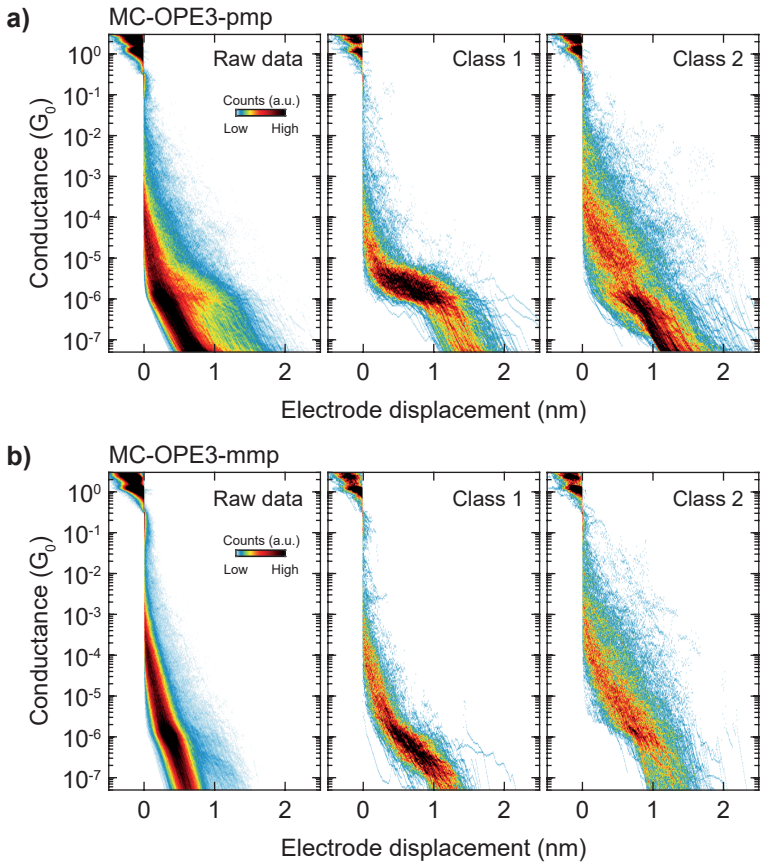

Figure 6.3: Two-dimensional conductance-displacement histograms of the raw data and the molecular classes constructed from a) 5000 traces of MC-OPE3-pmp, and b) 10000 traces of MC-OPE3-mmp

in Fig. 6.4b (bottom panel). Starting at $1.5{\cdot}10^{-4}$ G_0 at 0.1 V, the conductance value of OPE3-SAc hardly changes when increasing the bias to 0.5 V ($1.7{\cdot}10^{-4}$ G_0, within experimental error). At 1.0 V, the conductance value of OPE3-SAc increases to $2.2{\cdot}10^{-4}$ G_0, higher than the value at the lowest bias by a factor 1.46. This small increase reflect the flatness of the transmission function for OPE3-SAc in the middle of the HOMO-LUMO gap (see Fig. 3.7 and Ref. [223, 234]). MC-OPE3-pmp exhibits a more pronounced increase in conductance when increasing the bias. At 0.5 V, the conductance value is $5.2{\cdot}10^{-6}$ G_0, almost 2.5 times higher than at 0.1 V. This is a clear indication that the transmission function for this compound is steeper than the one of OPE3-SAc, possibly reflecting the presence of a quantum interference dip. Additionally, a class with traces having a conductance in the 10^{-7} G_0 range can also be identified when using the higher bias, as reported in Fig. 6.A3, although it is not very clear due to its proximity to the noise floor.

However, it is still unclear whether the quantum interference pattern in the molecule is affected by the presence of two branches, or if the conduction in the macrocycle

effectively ignores one of them and behaves in the same way as *meta*-OPE3. Since *meta*-OPE3 is know to have a destructive quantum interference dip [234], the bias dependence measured for MC-OPE3-pmp is not enough to answer this question. Measuring the bias dependence of conductance for *meta*-OPE3 and comparing it to the macrocycles would allow to explore the effect of the multiple pathways in more detail. However, at the current state, we did not perform any measurement of *meta*-OPE3.

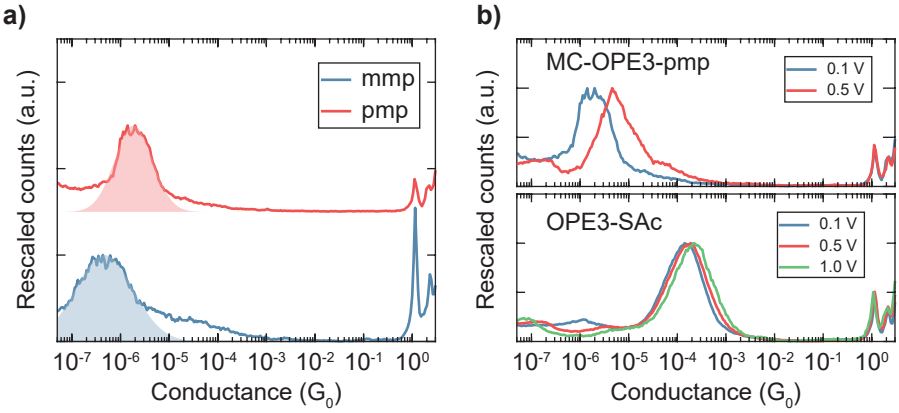

Figure 6.4: a) One-dimensional histograms of MC-OPE3-mmp (blue) and MC-OPE3-pmp (red) corresponding to the measurements shown in Fig. 6.3. The colored areas are the log-normal fit to the corresponding histogram. b) One-dimensional histograms of MC-OPE3-pmp and OPE3-SAc at different bias voltage. Counts have been rescaled by peak height to better compare peak position and shape. The corresponding two-dimensional histograms can be found in Fig. 6.A3 and Fig. 6.A2.

As a final note, it is worth mentioning that the measurement of these macrocycles has proven to be particularly challenging. First, the low conductance of the compounds required to improve the detection limit of the setup, which was only possible thanks to the amplifier discussed in Sec. 2.3. Second, it was critical to optimize the concentration of the molecular solution. Using a concentration of 100 μM would lead to unstable measurements (only able to measure few hundreds of consecutive traces), while already halving it would result in only empty junctions. For this reason, a concentration of 75 μM was employed. Even so, it was difficult to obtain reasonable yields for MC-OPE3-mmp.

To summarize, changing the position of one anchoring group from MC-OPE3-pmp to MC-OPE3-mmp lowers the conductance of the compound by a factor 2. Additionally, the measurements presented in this section show a large bias dependence of the conductance for MC-OPE3-pmp, which could be related to the presence of a quantum interference dip in the transmission of the molecule. However, theoretical calculations and more measurements (in particular of the non-macrocyclic *meta*-OPE3) are necessary to corroborate this hypothesis and to evaluate the effect of the additional branch.

6.3. 2,5-DIARYL 6-HYDROXYPHENALENONES SWITCH

6.3.1. INTRODUCTION

A molecular switch is one of the most basic functional devices that can be realized with molecules. It relies on the reversible change of conductance between two (or more) relatively stable states upon application of an external stimulus [39, 42]. The event can be triggered by different actions: light [17–19, 24], electrochemical reactions [20–22, 245], electric field [23, 217–221], or strain [34, 246–248].

Most molecular switches that have been characterized in break-junction techniques are only able two change their conductance between two levels; only few examples of three-state switching have been reported [22]. The compound studied in the latter reference inspired the chemical design of a molecular switch based on 6-hydroxyphenalenone derivatives[2]. In this section, we will characterize the charge transport properties of a 6-hydroxyphenalenone based switch[3], whose structure is depicted in Fig. 6.5a. The chemical synthesis and characterization of the compound is explained in detail in Ref. [139]. The compound exhibits switching to two different forms: an anion and a radical, as illustrated in Fig. 6.5b. The radical form can be obtained by oxidation of the compound, but is not stable in air for long periods of time. The anionic form can be obtained either through reduction of the 6-hydroxyphenalenone, or by deprotonation of the molecule. Both switched forms induce a significant change in the conjugation of the molecule which is possibly reflected in a change of conductance of a metal-molecule-metal junction. Currently it is unclear whether the anion and the radical would feature different conductance values, or if their behaviour would be different.

Additionally, the radical form, having an unpaired electron, is expected to exhibit magnetic properties [249]. However, cryogenic temperatures and external magnetic fields are necessary to characterize those. Considering also the low stability of the compound in this form, we will not characterize it in this study. In this section we will aim to identify the switching of the molecule to its anion by break-junction conductance measurements, while inducing the change either through protonating or deprotonating additives, or by increasing the bias voltage to induce the required electrochemical process.

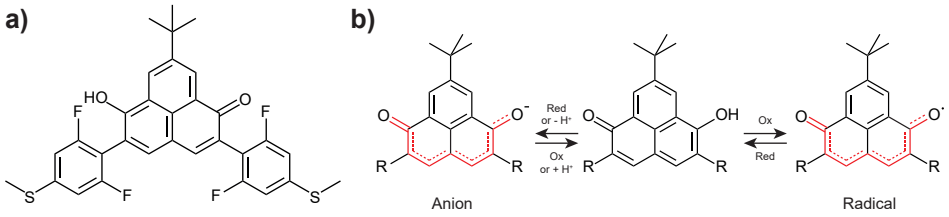

Figure 6.5: a) Chemical structure of the 2,5-Diaryl 6-hydroxyphenalenones molecular switch. b) Chemical structures of the 6-hydroxyphenalenones core (centre), its anionic form (left), and its radical form (right).

[2] Chemical design and synthesis by D. Vogel in the group of M. Mayor (Univeristy of Basel).
[3] Parts of this section have been published in The Journal of Physical Chemistry C **126**, 8801–8806 (2022).

6.3.2. MCBJ MEASUREMENTS

The first characterization of the compound was performed using 1 or 0.1 mM solutions in methanol (waiting for evaporation of the solvent after dropcast). The 2D- and 1D-histograms built using the measurements performed in this conditions are shown in Fig. 6.6a. Notice, in this figure all the measurements are collected together in one plot, interpolating with 1000 points in the interval -1 to 2.5 nm before building histograms, which is necessary to avoid errors in the histograms due to different attenuation factors. Information on the individual measurements can be found in Tab. 6.B1 and in the Supporting Information of Ref. [139], Fig. S243 to S245. Using clustering analysis, it is possible to clearly identify one molecular class, with a conductance value of $2.6{\cdot}10^{-6}$ G_0, and a length of 1 nm. The plateau length matches well the sulfur-to-sulfur distance obtained in the crystal structure of the compound [139], after adding ≈0.5 nm snapback distance of the electrodes [250].

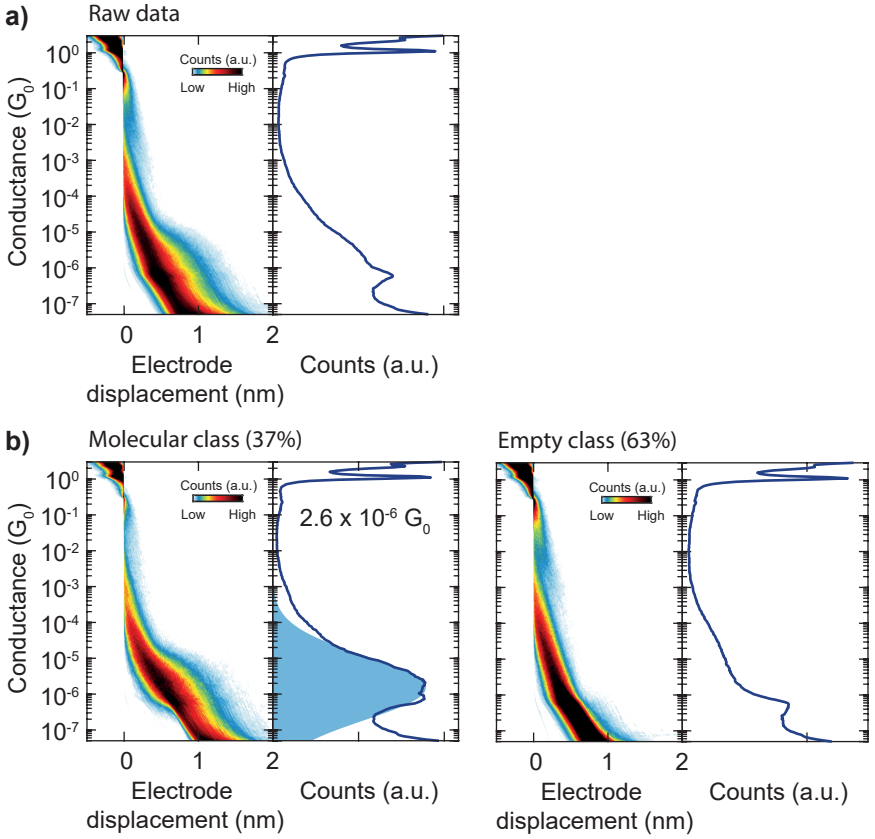

Figure 6.6: Two-dimensional (left) and one-dimensional (right) histograms of the 6-hydroxyphenalenone based compound dropcasted from a methanol solution constructed using a) 21927 breaking traces without classification and b) molecular and empty classes obtained through clustering. The molecular and empty class together form the raw data presented in a). The light blue areas correspond to the log-normal fits to the peak in the 1D-histogram.

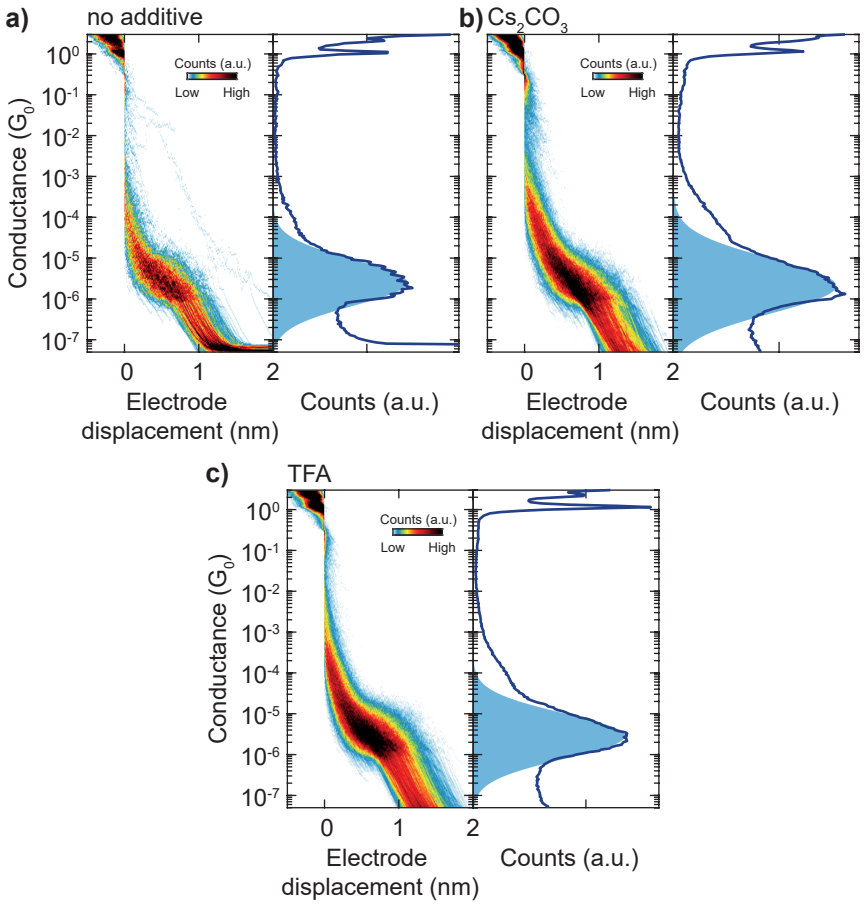

Figure 6.7: Two-dimensional (left) and one-dimensional (right) histograms of the molecular class measured a) with no additive, b) adding Cs_2CO_3 and c) adding trifluoroacetic acid (TFA), all using THF as solvent. Histograms of the raw data of these measurements can be found in Fig. 6.B1 to 6.B3. The light blue areas correspond to the log-normal fits to the peak in the 1D-histogram.

Next, we characterized the compound after adding substances able to increase (cesium carbonate, Cs_2CO_3) or to lower (trifluoroacetc acid, TFA) the pH of the solution. In solution, the former additive switches the molecule to the deprotonated form, while in the latter case, the lower pH ensures that the compound is protonated [139]. For these measurements, we switched the solvent to tetrahydrofuran (THF). Figure 6.7 displays the 2D- and 1D- histograms of the molecular class resulting from the measurements. First, changing the solvent does not have a relevant effect on the measured conductance (Fig. 6.7a and Tab. 6.B1). Second, introducing either of the two additives also does not affect the measured conductance significantly (Fig. 6.7b,c and Tab. 6.B1). This hints that the molecule is in the same protonation state independently on the additive. It would be useful to repeat these experiments in solution, to evaluate whether the lack of conductance changes arises just from the evaporation of the solvent, or if it is induced by the

bonding to the gold surface.

Lastly, we explored the influence of bias on the conductance of the molecule. First, we measured the compound at 0.05 V, lower than the voltage used in the previous measurements (0.1 V). From the results reported in Tab. 6.B1, it is clear that the conductance between 0.05 V and 0.1 V does not significantly change (both when having TFA or Cs_2CO_3 as additive). We also performed measurements at higher bias. Using the compound with Cs_2CO_3, we increased the bias to 0.5 V, and then to 1.0 V, all on the same junction. The 1D-histograms resulting from these measurements are shown in Fig. 6.8a, and the corresponding 2D-histograms can be found in Fig. 6.B3. At 0.5 V bias, we report a conductance value of $3.5 \cdot 10^{-6}$ G_0, only marginally higher than the low-bias measurement ($2.1 \cdot 10^{-6}$ G_0). For the largest bias, we find a conductance of $7.0 \cdot 10^{-6}$ G_0, twice as high as for a bias of 0.5 V. However, the increase only marginally higher than what we reported for OPE3 in Sec. 6.2, which hints that this change is due to the convex shape of the transmission function, rather than because of a switching process. Lastly, we repeated the experiment using the molecule with no additive (to avoid any effect that the additional compound could have on the measurement), and increasing the bias up to 1.5 V. The 1D-histograms are displayed in Fig. 6.8b, with the corresponding 2D-histograms in Fig. 6.B2. At 1.0 V, we retrieve a conductance value of $7.9 \cdot 10^{-6}$ G_0, comparable with the previous experiment. Interestingly, when increasing the bias at 1.5 V, we observe a sharp increase in conductance to $5.4 \cdot 10^{-5}$ G_0, which is an indication that a switching process could have happened. This would be related to the change of the molecule's structure from its neutral form to the anion, as depicted in Fig. 6.5b. This explanation is also supported by the redshift observed in the absorption and emission spectra of the compound upon deprotonation (see Table 1 in Ref. [139]), which indicates a decrease of the HOMO-LUMO gap. However, without proper first-principle calculations, it is difficult to assess whether the change in conductance is related to the change of the molecule to the anionic for. Additional experiments, such as current-voltage characteristics or time-domain response to square voltage steps could also help in defining an explanation for the supposed switching mechanism.

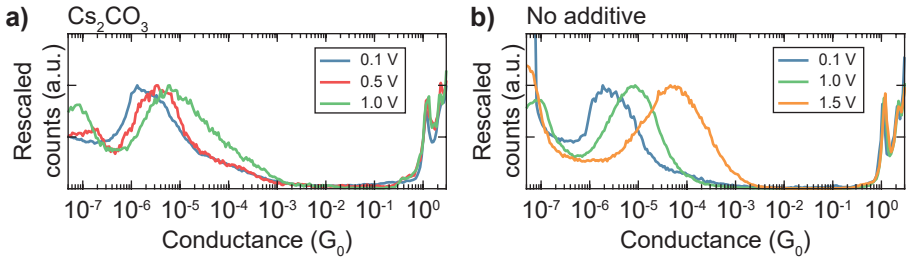

Figure 6.8: One-dimensional histograms of the high-bias measurements of the compound with a) Cs_2CO_3 additive and b) with no additive. Counts have been rescaled by peak height.

There are a few consideration that have to be made before drawing any conclusion. When using the higher bias levels, many long traces (>1.5 nm) are present in the measurements, whose origin is unclear at the moment. These are evident in Fig. 6.B3c and Fig. 6.B2c. Notably, the clustering approach used for the analysis, using only 2 clusters, mostly separates these traces and the empty ones (Class 2) from a shorter group of traces

(Class 1), as shown in Fig. 6.B1 to 6.B3. The latter has a length comparable to the plateau measured at low bias, and thus we focused on this class in the comparison shown in Fig. 6.8. Additionally, at the end of these high-bias measurements, the junction is not able to merge back to the conductance threshold we usually consider as a fully made junction (30 G_0). Because of this, we could not repeat a measurement at 0.1 V at the end of the high bias one, which leaves unclear whether the process affects the molecule in a reversible manner or not. Even more importantly, at the moment of writing this dissertation, the measurement at 1.5 V has not been repeated yet. Thus, the reported behaviour, however interesting, must be evaluated with care.

In summary, we characterize the charge transport properties of a 2,5- diaryl 6- hydroxyphenalenones molecular switch using different solvents and additives to prepare the solution. We find that, when measuring the compound in dry conditions, there is no significant change in the measured conductance value. It would be useful to perform the experiments in liquid conditions, to assess whether the lack of the expected change is due to the solvent evaporation process. Additionally, we perform high-bias measurements of the compound. We observe that the conductance of the system only marginally increases up to 1.0 V bias. A preliminary measurement at 1.5 V shows a promising conductance increase, but more experiments need to be performed to draw appropriate conclusions.

6.4. NORBORNADIENE–QUADRICYCLANE SWITCH

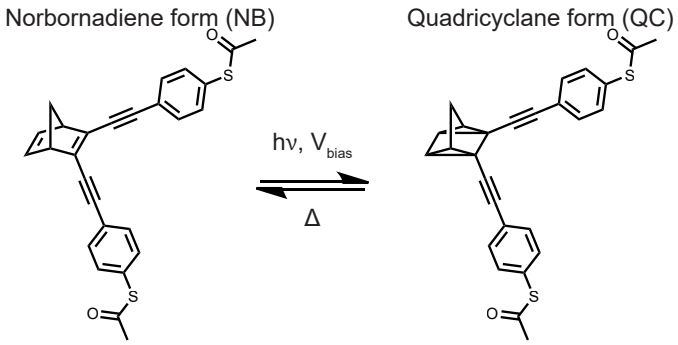

Figure 6.9: Chemical structure of the NB-QC switch analysed in this section. The molecule starts in the NB form, and can be switched to the QC one upon illumination or application of a large voltage bias. The backwards reaction happens via thermal relaxation.

In this section, we report MCBJ measurements of a Norbornadiene (NB) – Quadricyclane (QC) molecular switch, based on a modification of an already published design [24, 218]. The molecule is synthesized in the NB form[4], and it can be switched to the QC form by irradiating with UV-light, or by applying a large enough voltage bias. During this process, the central unit changes its hybridization from sp^2 to sp^3, breaking the conjugation path along the molecule. For this reason, the conductance of NB is higher than the one of QC and the two could exhibit different mechanoresistive behaviour [24]. The backwards switch happens spontaneously by thermal relaxation. The design characterized in this

[4] Synthesis by S. Ghasemi, in the group of K. Moth-Pulsen (Chalmers University of Technology).

section (Fig. 6.9) presents a shorter (phenylene ethynylene) arm for connection to the electrodes than the previously reported compound, and is thus expected to have a higher overall conductance. In the following, we will present the standard characterization of the molecule at low bias. At the time of writing, measurements of the high-bias switching of the molecule are ongoing, and measurements using different anchoring groups have been scheduled.

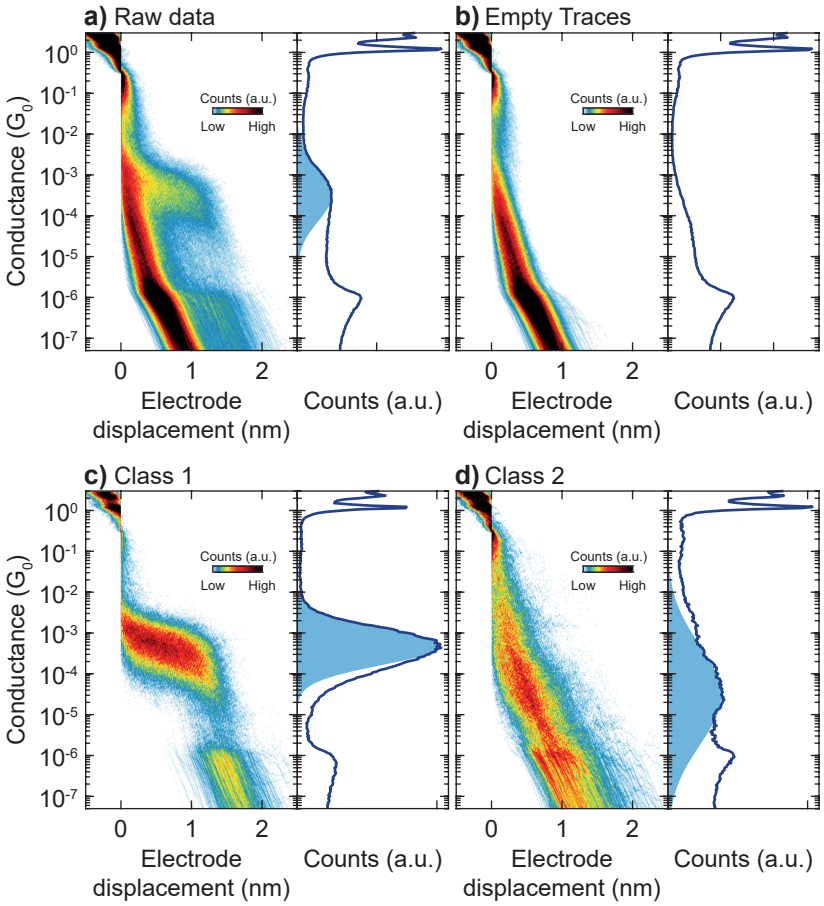

Figure 6.10: Two-dimensional (left) and one-dimensional (right) histograms of a) the raw data of an NB measurement, b) the empty traces removed from it, c) Class 1 obtained by clustering the molecular traces, and d) Class 2 resulting from the same analysis. The light blue areas correspond to the log-normal fits to the peak in the 1D-histogram.

The 2D-histogram in Fig. 6.10a presents a clear plateau. We further process the data by first removing the empty traces using the neural network procedure reported in Sec. 2.2.2 (histograms of the traces classified as empty are shown in Fig. 6.10b). Then, we perform the clustering analysis on the remaining molecular traces (using the parameters described in Sec. 6.C), obtaining the two classes shown in Fig. 6.10c,d. The molecule

shows a clear plateau at $4 \cdot 10^{-4}$ G_0, which is higher than the value reported in literature for the compound with longer arms ($1 \cdot 10^{-4}$ G_0). The plateau has a length of around 1.2 nm. With the commonly used approach of adding a snapback distance of about 0.5 nm [250], this yields a length of the molecule of around 1.7 nm. Surprisingly, this value is significantly longer than the length of the molecule (estimated[5] to be approximately 1.1 nm). The same plateau, with the same length, is present in a second measurement (shown in Fig. 6.C1 and Fig. 6.C2). The molecular yield in this additional measurement is much lower than the previous one, hinting that the reason for the long plateaus could be different than the formations of π-stacked dimers or chains of molecules [81, 82, 85, 86]. At the moment, we do not have an explanation for this observation. We can speculate that, starting from the V-shaped structure of Fig. 6.9, the molecule stretches until reaching an almost-linear conformation due to the strain applied during the breaking trace. As for Class 2 (Fig. 6.10b), it shows a broad conductance peak in the 10^{-5} G_0 range, rather than a clear plateau. This behaviour is reminiscent of the QC-state reported in Ref. [24]. However, more control experiments are needed to properly assign this second class present in our measurements.

Lastly, we observe that the measurement presents a decay in the probability of showing a molecular plateau over time. To illustrate this, for each trace we define an interval that spans 100 traces to the left and 100 to the right (we exclude the first and last 100 traces, for which the complete interval cannot be defined), corresponding to roughly 25 minutes of measurement. For each of these intervals, we compute the probability of measuring Class 1, Class 2, or an empty trace.Figure 6.11a plots the result of this analysis for NB. It is clear that the probability of measuring the molecular plateau (Class 1) decreases over time, and it is vanishing after around 5000 traces. For comparison, Fig 6.11b shows the same analysis performed on the measurement of OPE3-SAc in Sec. 6.2. In this case, the probability of measuring the high-conductance plateau (Class 1) increases in the first 1000 traces, and quickly stabilizes around 0.4 until the end of the measurement (and probably longer, since the two measurements performed afterwards on the same junction have similar yield than the one plotted here, see Tab. 6.A1). A likely reason for the decay in the NB measurement is a degradation of the compound when in contact with oxygen. Measurements in vacuum will be performed to attempt to improve the stability of the molecule.

To summarize, the NB-QC molecular switch in the NB form shows a well defined plateau at $4 \cdot 10^{-4}$ G_0, with a length of around 1.2 nm, and the probability of encountering this feature decreases with time. Further measurements are needed to give concrete explanations to the features of this plateau, and to characterize the switching behaviour as a function of bias voltage or under illumination.

[5] Estimated with Chem3D 20.0 MM2 optimization.

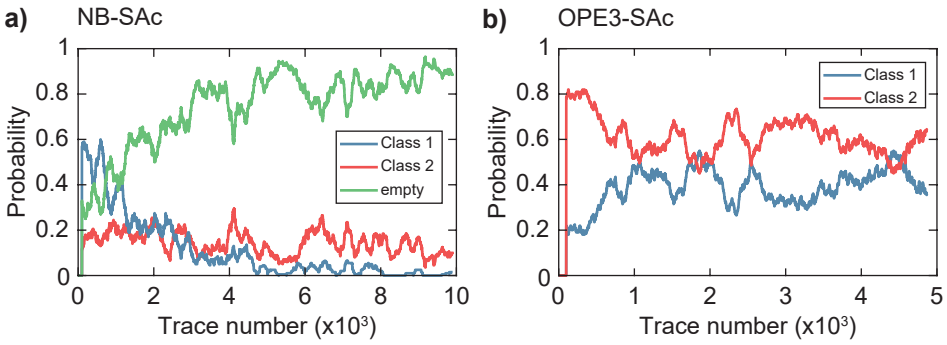

Figure 6.11: a) Evolution of the probability of obtaining Class 1 (blue), Class 2 (red), or an empty trace (green) in an interval of 200 traces in the measurement of NB shown in Fig. 6.10. b) Evolution of the probability of obtaining Class 1 or Class 2 in an interval of 200 traces in the measurement of OPE3-SAc shown in Fig. 6.4b and Fig. 6.A2a. The total measurement time is around 21 hours for panel a) and 12 hours 20 minutes for panel b).

6.A. APPENDIX A - ADDITIONAL INFORMATION ON OPE-BASED MACROCYCLES

6.A.1. CLUSTERING PARAMETERS

For the clustering analysis of the data, a combination of the 2D- and 1D-histograms was used. For the macrocycles, the 2D-histogram of the trace is computed in the range 0 to 2 nm in displacement and -0.5 to -7 $\log(G/G_0)$ in conductance, using a 30×30 bins grid. The 1D-histograms is calculated using 100 bins and -0.5 to -7 $\log(G/G_0)$ limits. To simplify the clustering procedure for these molecules the tunnelling traces were filtered out beforehand. As the conductance of these molecules lies below the minimum value used to train the neural network described in Sec. 2.2.2, we had to use another method. Thus, we employed the less-refined classification based on the number of counts. The number of counts in the range -0.5 to -7 $\log(G/G_0)$ was computed for each trace. Then, a histogram of the number of the counts is built and fitted to a Gaussian distribution. All traces having counts lower than the center of the distribution plus its width are considered empty. This strategy was sufficient to effectively filter out the tunnelling traces in the measurements of the macrocycles, although it might not be accurate in all cases. The 2D-histograms of the empty traces for the measurements shown in this chapter are reported in Fig. 6.A1.

For OPE3-SAc, the 2D-histogram of the trace is computed in the range 0 to 3 nm in displacement and -0.5 to -8 $\log(G/G_0)$ in conductance, using a 30×30 bins grid. The 1D-histograms is calculated using 100 bins and -0.5 to -8 $\log(G/G_0)$ limits. No pre-filtering of the tunnelling traces was performed in this case as the high-conductance plateau was easily separated from the raw data. In this chapter, we do not analyse the low-conductance features of this molecule.

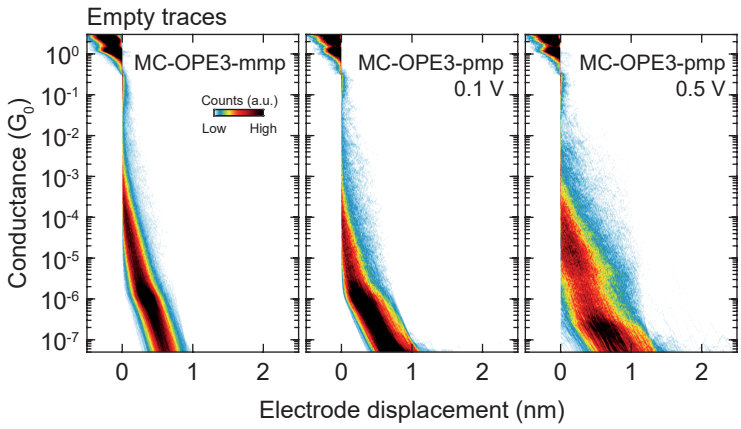

Figure 6.A1: Two-dimensional histogram of the empty traces excluded before clustering for MC-OPE3-mmp (N = 1.1 in Tab. 6.A1), MC-OPE3-pmp at 0.1 V bias (N = 1.1), and MC-OPE3-pmp at 0.5 V bias (N = 1.2).

6.A.2. ADDITIONAL PLOTS AND TABLES SUMMARIZING EXPERIMENTAL RESULTS

This section reports additional figures and a summary table supporting the discussion in Sec. 6.2.

Table 6.A1: Conductance values extracted from fitting the class 1 for each measurement of OPE3-SAc and the two macrocycles. N is the measurement number, reported as x.y (x = sample number, y= measurement number) and n traces is the total number of traces measured. The yield is the percentage of traces classified in each class with respect to the total number of traces. *Measurement shown in Fig. 6.3 and Fig. 6.4a. $^{+}$Measurement shown in Fig. 6.4b (top panel) and in Fig. 6.A3. † Measurement shown in Fig. 6.4b (bottom panel) and Fig. 6.A2.

Molecule	N	Bias (V)	n traces	Class 1 (G/G_0)	Class 1 Yield (%)	Class 2 Yield (%)	Class 3 Yield (%)
MC-OPE3-pmp	1.1*	0.1	5000	$1.9\cdot10^{-6}$	9	15	-
	1.2^{+}	0.5	5000	$5.3\cdot10^{-6}$	11	15	11
	2.1	0.1	10000	$2.2\cdot10^{-6}$	5	2	-
	3.1	0.1	2000	$1.2\cdot10^{-6}$	7	10	-
	3.2	0.5	2000	$5.1\cdot10^{-6}$	4	7	6
MC-OPE3-mmp	1.1*	0.1	10000	$4.6\cdot10^{-7}$	4	3	-
OPE3-SAc	1.1†	0.1	5000	$1.5\cdot10^{-4}$	38	62	-
OPE3-SAc	1.2†	0.5	5000	$1.7\cdot10^{-4}$	41	59	-
OPE3-SAc	1.3†	1.0	1858	$2.2\cdot10^{-4}$	31	69	-

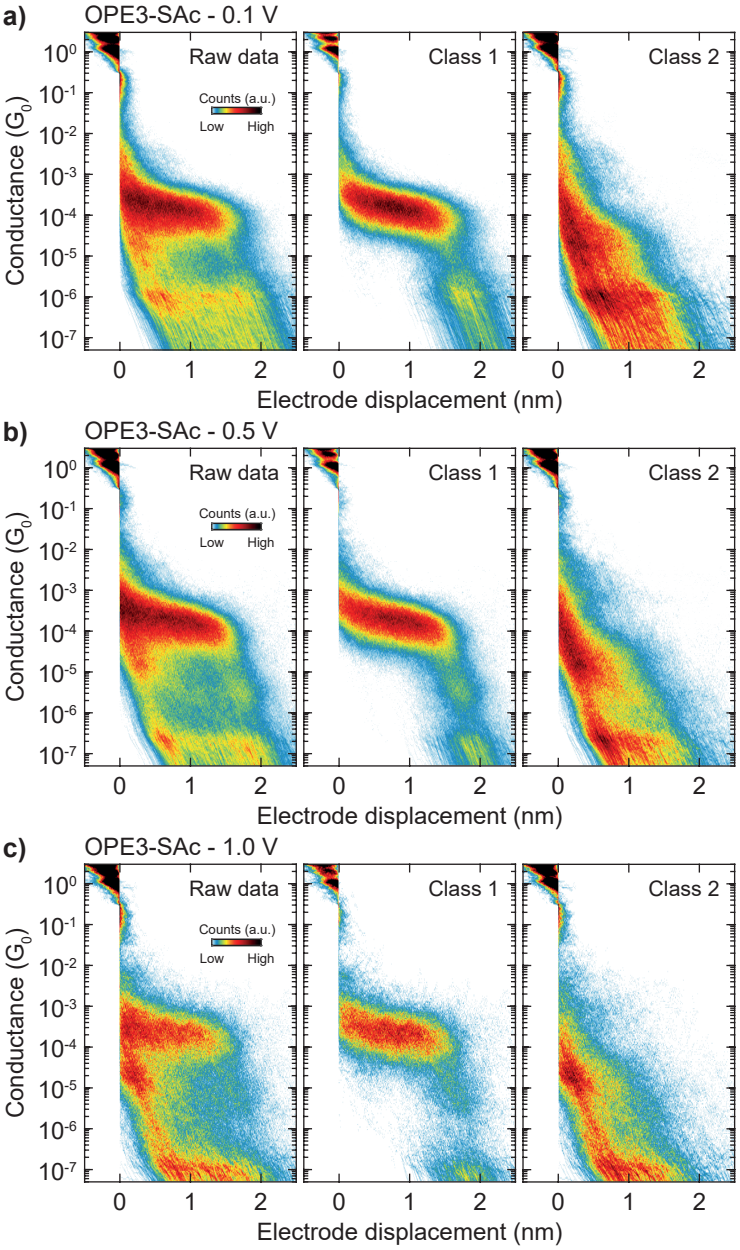

Figure 6.A2: Two-dimensional histogram for the raw data and the two classes measured for OPE3-SAc at a) 0.1 V, b) 0.5 V and c) 1.0 V bias. The one-dimensional histograms corresponding to Class 1 of these measurements are shown in Fig. 6.4b (bottom panel).

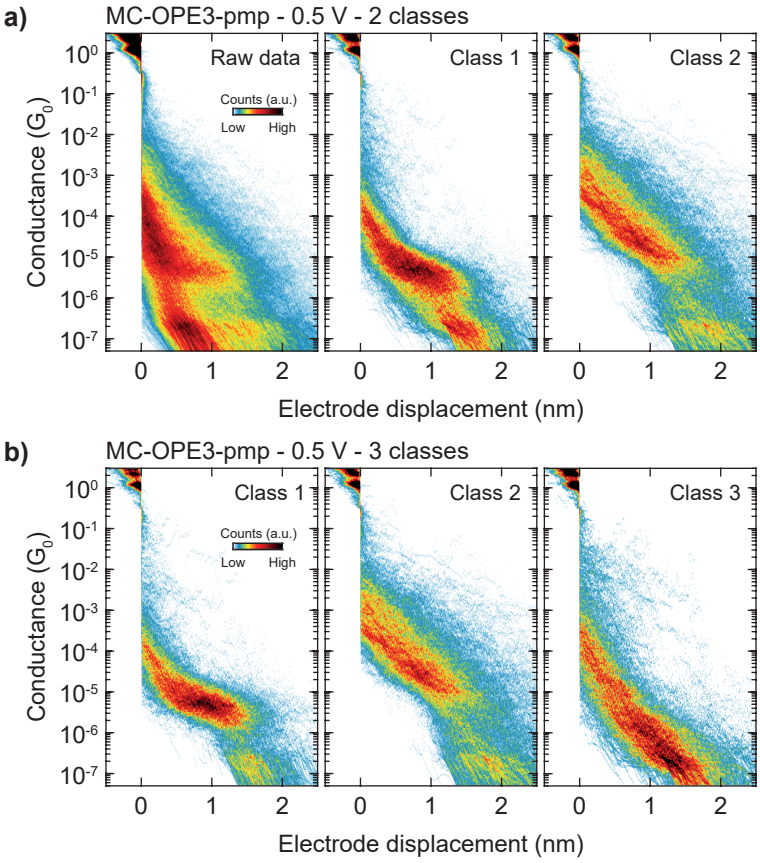

Figure 6.A3: Two-dimensional histogram for the 0.5 V bias measurement of MC-OPE3-pmp: a) raw data and classes obtained when splitting it in 2 clusters (after removing the empty traces); b) classes obtained when dividing the data in 3 clusters (this corresponds to N=1.2 in Tab. 6.A1, and the one-dimensional histogram of Class 1 is shown in Fig. 6.4b top panel).

6.B. APPENDIX B: ADDITIONAL INFORMATION ON 6-HYDROXYPHENALENONE SWITCH

This section reports additional figures and a summary table supporting the discussion in Sec. 6.3. For the clustering analysis, a combination of the 2D- and 1D-histograms was used. The 2D-histogram is computed in the range 0 to 2 nm in displacement and -0.5 to -7 $\log(G/G_0)$ in conductance, using a 30×30 bins grid. The 1D-histograms is calculated using 100 bins and -0.5 to -7 $\log(G/G_0)$ limits.

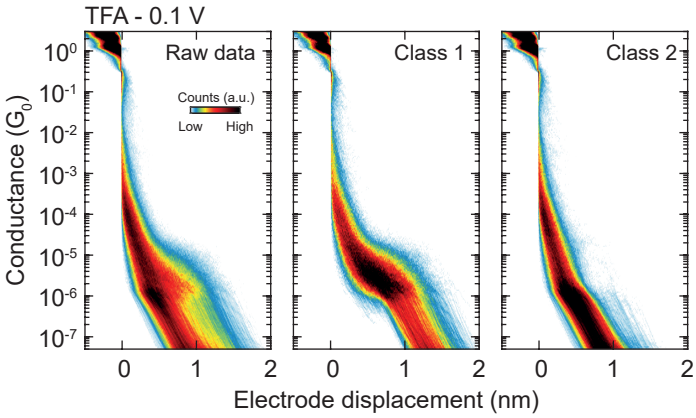

Figure 6.B1: Two-dimensional histograms for the raw data and the classes obtained for the measurements with TFA in THF, using a voltage bias of 0.1 V (N = 2.2 in Tab. 6.B1).

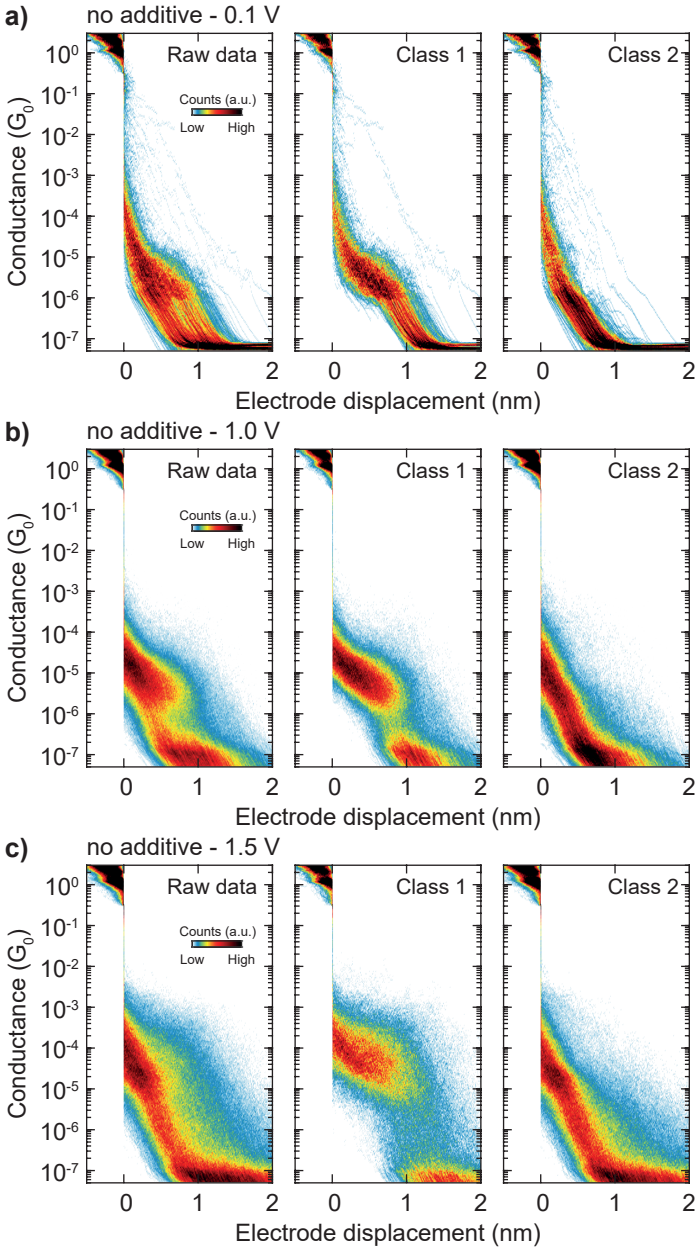

Figure 6.B2: Two-dimensional histograms for the raw data and the classes obtained for the measurements with no additive in THF, using a voltage bias of a) 0.1 V (N = 4.1 in Tab. 6.B1), b) 1.0 V (N = 4.2) and c) 1.5 V (N = 4.3). The 1D-histograms of Class 1 of these measurements are shown in Fig. 6.8b.

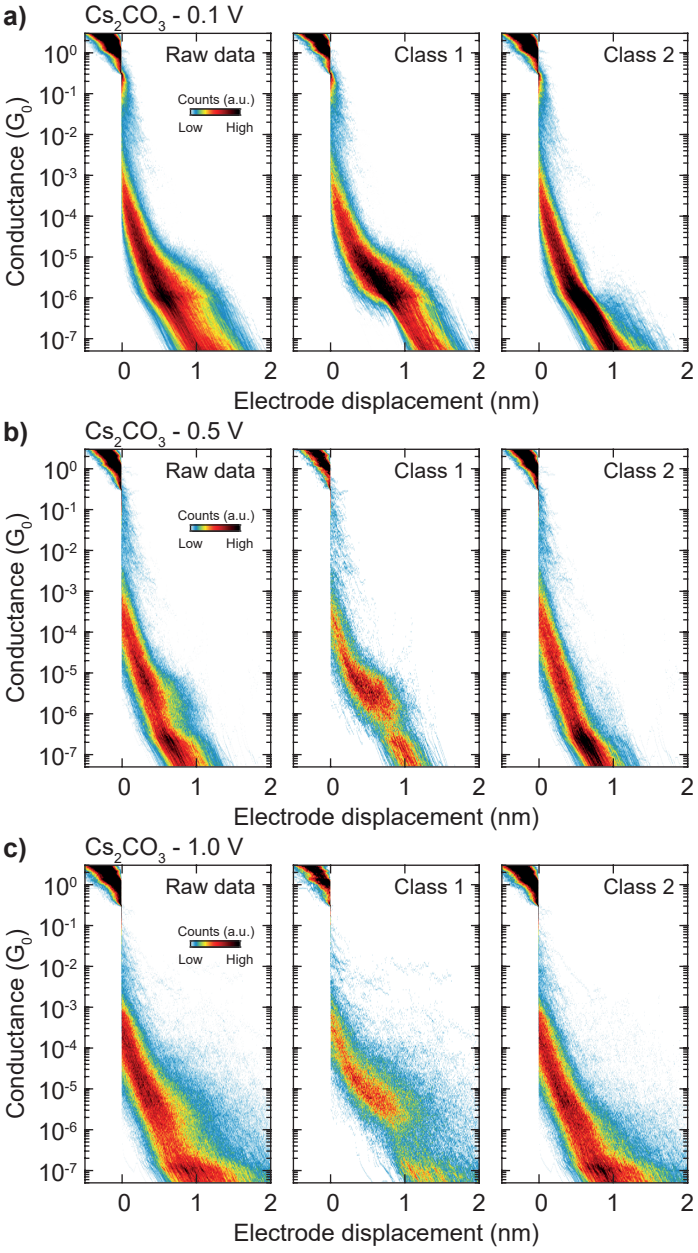

Figure 6.B3: Two-dimensional histograms for the raw data and the classes obtained for the measurements with Cs_2CO_3 additive in THF, using a voltage bias of a) 0.1 V (N = 3.2 in Tab. 6.B1), b) 0.5 V (N = 3.3) and c) 1.0 V (N = 3.4). The 1D-histograms of Class 1 of these measurements are shown in Fig. 6.8a.

Table 6.B1: Conductance values and details on the measurements discussed in Sec. 6.3. N is the measurement number, reported as x.y (x = sample number, y= measurement number) and n traces is the total number of traces measured. The yield is the percentage of traces classified in the molecular class with respect to the total number of traces of the measurement when separating the data in 2 clusters. *Measurement shown in Fig. 6.6 and published in Ref. [139]. $^{+}$Measurement shown in Fig. 6.7. † Measurement shown in Fig. 6.8

Additive	N	Solvent	Concentration (mM)	Bias (V)	n traces	Class 1 (G/G_0)	Molecular Yield (%)
None	1.1*	methanol	1	0.1	10000	$1.7 \cdot 10^{-6}$	14
	2.1*	methanol	1	0.1	2761	$3.0 \cdot 10^{-6}$	71
	2.2*	methanol	1	0.1	3945	$2.7 \cdot 10^{-6}$	63
	3.1*	methanol	0.1	0.1	1976	$2.2 \cdot 10^{-6}$	37
	3.2*	methanol	0.1	0.1	3245	$2.9 \cdot 10^{-6}$	52
	$4.1^{+\dagger}$	THF	0.1	0.1	1000	$2.6 \cdot 10^{-6}$	47
	$4.2^{\dagger}$	THF	0.1	1.0	5000	$7.9 \cdot 10^{-6}$	43
	$4.3^{\dagger}$	THF	0.1	1.5	3870	$5.4 \cdot 10^{-5}$	27
TFA	1.1	THF	0.1	0.05	3615	$2.4 \cdot 10^{-6}$	38
	1.2	THF	0.1	0.1	1653	$1.5 \cdot 10^{-6}$	37
	2.1	THF	0.1	0.05	1000	$2.8 \cdot 10^{-6}$	12
	2.2^{+}	THF	0.1	0.1	10000	$2.8 \cdot 10^{-6}$	32
Cs_2CO_3	1.1	methanol	0.1	0.1	10000	$1.6 \cdot 10^{-6}$	51
	2.1	THF	0.1	0.1	2200	$1.5 \cdot 10^{-6}$	50
	2.2	THF	0.1	0.1	2000	$1.2 \cdot 10^{-6}$	46
	2.3	THF	0.1	0.5	2000	$2.9 \cdot 10^{-6}$	42
	3.1	THF	0.1	0.05	10000	$3.2 \cdot 10^{-6}$	43
	$3.2^{+\dagger}$	THF	0.1	0.1	5000	$2.1 \cdot 10^{-6}$	40
	$3.3^{\dagger}$	THF	0.1	0.5	2000	$3.5 \cdot 10^{-6}$	23
	$3.4^{\dagger}$	THF	0.1	1.0	2000	$7.0 \cdot 10^{-6}$	48

6.C. APPENDIX C: ADDITIONAL INFORMATION ON NB-QC MOLECULAR SWITCH

This appendix reports additional figures and a summary table for the measurements on the NB-QC molecular switch analysed in Sec. 6.4. The clustering parameters are analogous to Sec. 6.B: the 2D-histogram is computed in the range 0 to 2 nm in displacement and -0.5 to -7 $\log(G/G_0)$ in conductance, using a 30×30 bins grid. The 1D-histograms is calculated using 100 bins and -0.5 to -7 $\log(G/G_0)$ limits. Notice, that for measurement 2.1 of NB it was necessary to use 4 clusters (shown in Fig. 6.C2) to obtain two classes comparable to measurement 1.1 (see Fig. 6.10, for which 2 clusters were used). The two additional clusters contain slanted traces which were not classified as tunnelling (Fig. 6.C2c) and traces with high noise (Fig. 6.C2d), which can be considered outliers.

Table 6.C1: Conductance values and details on the measurements discussed in Sec. 6.4. N is the measurement number, reported as x.y (x = sample number, y= measurement number) and n traces is the total number of traces measured. The yield is the percentage of traces classified in the molecular class with respect to the total number of traces of the measurement when separating the data in 2 clusters. *Measurement shown in Fig. 6.10. $^+$Measurement shown in Fig. 6.C1 and Fig. 6.C2.

N	Concentration (μM)	Bias (V)	n traces	Class 1 (G/G_0)	Class 1 Yield (%)	Class 2 (G/G_0)	Class 2 Yield (%)
1.1*	1	0.1	10000	$4.7 \cdot 10^{-4}$	11	$3.0 \cdot 10^{-5}$	14
2.1$^+$	0.1	0.1	10000	$2.9 \cdot 10^{-4}$	0.4	$4.7 \cdot 10^{-5}$	2

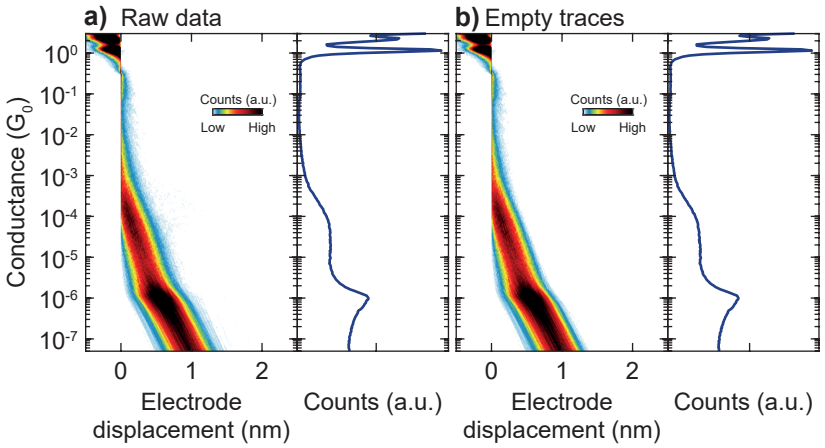

Figure 6.C1: Two-dimensional histograms (left) and one-dimensional histograms (right) of the a) raw data and b) the traces selected as empty through the neural network method for measurement 2.1 in Tab. 6.C1.

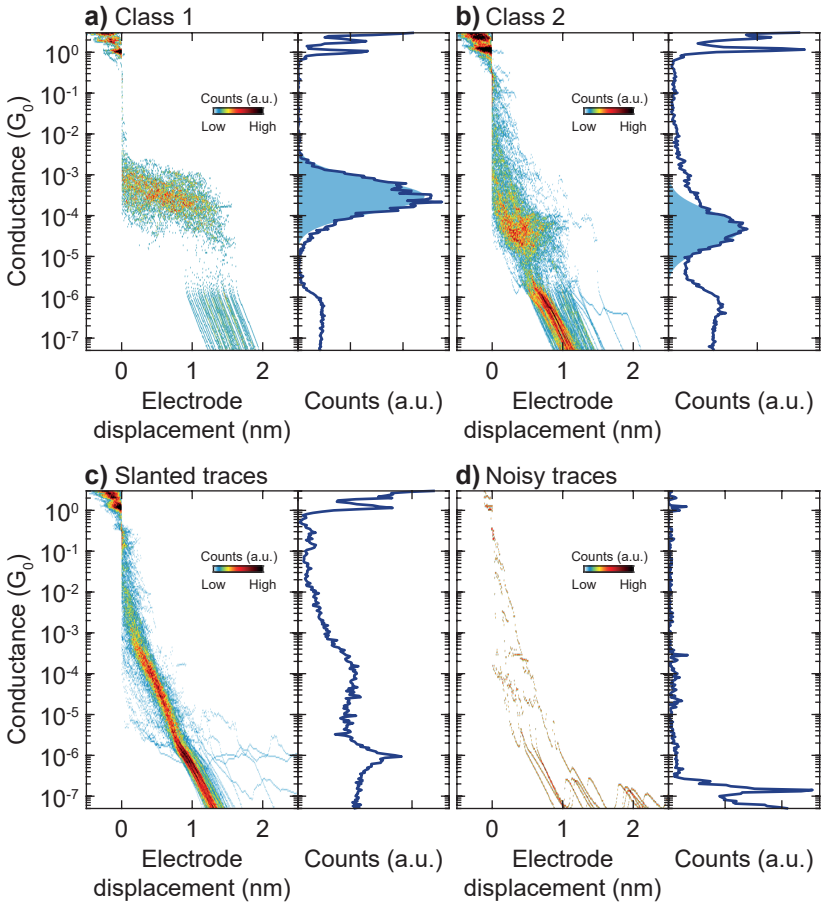

Figure 6.C2: Two-dimensional histograms (left) and one-dimensional histograms (right) of a) Class 1 (with a yield of 0.4 %), b) Class 2 (2 %), c) the slanted traces (2 %), and d) traces with high noise (0.05 %). The four plots were obtained by clustering in 4 clusters the traces selected as molecular from measurement 2.1 in Tab. 6.C1. The light blue areas correspond to the log-normal fit to the peak in the 1D-histogram.

7

CONCLUSION AND OUTLOOK

CONCLUSION

Metal-molecule-metal junctions are complex systems. In this dissertation, we addressed a few intricacies involved in the charge transport across them. We first analysed a series of acene-substituted OPE3s (Ch. 3), comparing their charge transport in nanoscale (with the MCBJ technique) and large-area junctions (with EGaIn measurements). We have shown that, in MCBJ experiments it is possible to discern between multiple peaks in conductance histograms. More specifically, we identified one reproducible plateau that corresponds to the sulfur-to-sulfur transport pathway across the molecule, separating it from the other possible junction configurations. On the other hand, ensemble measurements only probe the conductance averaged over a large number of different conformations. In particular, the ensemble conductance of pentacene substituted OPE3 (PC) was significantly lower than the one of the other compounds, while in MCBJ experiments the conductance followed the trend predicted by theory. However, MCBJ measurements of PC presented a significant fraction of long traces, contrary to the other compounds. We ascribed this finding to the presence of significant intermolecular interactions in PC, which leads to the formation of π-stacked dimers in MCBJ, and introduce higher low-conductance defects in SAMs. This study highlighted how the combination of MCBJ and EGaIn measurements is able to give more insight on the nature of charge transport, allowing to distinguish between scenarios where molecules show significant intermolecular interactions, and scenarios in which they do not.

Then, in Ch. 4 we turned our attention to events happening within a single breaking trace, rather than to the average conductance of the junction. More precisely, we studied the presence of switching events in molecular junctions, analysing the effect of anchoring groups and molecular backbone. We reported that, for several anchoring groups, a significant fraction of traces shows switching even when using a backbone for which this behaviour is not expected (OPE3). A notable exception was OPE3-SAc, for which switching is almost absent. We classified these events in two groups: "plateau" switches, in which the conductance switches between two semi-stable values, and "tunnelling"

ones, in which the junction first exhibits an exponential decay of the conductance, to then switch to a molecular plateau. We attributed the former type of event to junctions in which the binding geometry to the electrodes is changing, and we hinted that the latter originates from junctions forming after rupture of the atomic point contact. These results give a perspective on the intrinsic statistical switching in break-junction experiments, which should be taken into account when a switching functionality is introduced in the molecular backbone by chemical design.

Chapter 5 returned on the aspect of multiple peaks in conductance histograms, but under a different point of view. In the chapter, we analysed the effect of electron-donating and electron-withdrawing substituents. We observed that these have different, although small, effects on the conductance peaks in the histograms. Explaining the trends proved to be challenging. It was necessary to develop a theoretical method that includes different binding geometries, non-equilibrium junction conformations, and the possibility that the molecule energy levels position fluctuates with respect to the electrodes' Fermi level. These results illustrate how chemical design concepts are not easily translated to metal-molecule-metal junctions because of the intrinsic variance of the latter.

Lastly, in Ch. 6 we presented three studies that employ high-bias measurements of molecular junctions. We analysed the behaviour of macrocyclic molecules and of two molecular switches, exploring the possibilities that this additional tuning knob brings to molecular junctions. With the newly developed method, it is possible to measure current-voltage characteristics and conductance histograms up to $\pm$ 2 V bias.

OUTLOOK

7

In these last few paragraphs, I would like to present a few reflections and research directions that one can explore in molecular electronics. Similar points have been recently discussed, from a different perspective, by Mol J.A. in the *Roadmap to quantum technologies* [251].

The first point I would like to discuss is the question "are we measuring single-molecule contacts?". The general consensus in the community is that break-junction techniques like MCBJ or STMBJ (scanning tunnelling microscope break-junction) are able to do so. However, at the very least that is not *always* true. As I mentioned in Sec. 1.2, π-stacked dimers and chains of molecules can form in the junction. Thanks to machine learning based approaches, however, we are now able to discern these cases from the one in which hopefully "a single molecule" is present. There is one more complication though, as I mentioned in Ch. 4 [175]. It is possible that junctions composed of multiple molecules form after separation of the electrodes. The next question would be "is it possible to distinguish junctions with multiple molecules from junctions with a single one?". Here, machine learning is not (yet) of help, and the question is still unanswered. There is one more aspect to point out: switching. One can reasonably think that, if a junction exhibits plateau or tunnelling events (as described in Ch. 4), than it is composed of a single molecule. The reasoning is: if multiple molecules were present, than all of them would need to switch *at the same time* for the event to happen, which is highly unlikely. The conductance values reported in Ch. 4, as well as the observations of González *et al.* [175] point in this direction: the conductance extracted from switching traces is consistently lower than the one of non-switching traces. We can even bring the discussion one step

further. Would it be possible to identify in which configuration a junction is in a specific trace, at a certain displacement? Although far-fetched, being able to answer this question would enable to use break-junction techniques as spectroscopic tools, rather than simple conductance characterization methods. Being able to address the conductance variations in breaking traces is the first step in this direction.

The second point concerns the "application" side of molecular electronics. Both in Ch. 1 and Ch. 6 I mentioned a few functions that molecules can fulfill as electronic components. However, the studies published so far stop at the proof-of-concept stage. There are a few issues that quenched the realization of more concrete devices. First, the progress of silicon technology has put to rest the claim of using molecules as alternative building blocks for microprocessors. This required researchers to shift their attention to different functionalities, like switching, thermoelectricity, or sensing (perhaps the most promising one). Second, no reliable way of anchoring molecule to electrodes has been developed so far.

There are two side to this challenge: mechanical stability, and electrical variance. With mechanical stability I refer to the robustness of the chemical (or physical) connection to the electrodes. Depending on the technique, electrode material, and anchoring group, the metal-molecule-metal junction can last up to hours at room temperature. This is more than enough for scientific work, but viable devices would need to have consistent performance for *years*. In this sense, self-assembled monolayers are a more reliable way to anchor molecule to an electrode. Soft top-contacts (like the EGaIn method in Ch. 3) are consistent ways to realize connection to them, but due to the liquid phase of the material, their integration in devices is complex. There are other methods to fabricate top contacts based on traditional metals deposited, e.g., by physical or chemical vapour deposition. However, the field still faces challenges to embed them in smaller-scale circuits, and without introducing defects in the layers [49]. Electrical variance is the concept that was treated the most in this dissertation: the current flowing through a metal-molecule-metal junction can fluctuate by an order of magnitude due to their intrinsic conductance variations. These fluctuations have to be suppressed or at least accounted for when implementing molecules in more complex circuits. At the research level, we can now (partially) address this challenge with careful analysis of the measurement data. Whether this is possible in a device the should work "on its own" is sill up for debate. Perhaps, trying to suppress as many fluctuation mechanisms at the chemical design stage is a more desirable approach.

In this dissertation we explored different aspects of the complexity of charge transport in nanoscale molecular junctions. We explored the effects of intermolecular interaction, contact chemistry and geometry, and bias-voltage, combining the mechanically controllable break-junction technique with clustering based analysis. We have shown that it is possible to address the variance in these systems, and we gained further insight on their behaviour. The variability of metal-molecule-metal junctions is one of the main challenges that molecular electronics is facing, and one that has to be dealt with for the field to progress.

REFERENCES

[1] A. von Hippel, Science **123**, 315–317 (1956).

[2] A. Aviram and M. A. Ratner, Chemical Physics Letters **29**, 277–283 (1974).

[3] B. Mann and H. Kuhn, Journal of Applied Physics **42**, 4398–4405 (1971).

[4] C. Joachim, J. K. Gimzewski, R. R. Schlittler, and C. Chavy, Physical Review Letters **74**, 2102–2105 (1995).

[5] M. A. Reed, C. Zhou, C. J. Muller, T. P. Burgin, and J. M. Tour, Science **278**, 252–254 (1997).

[6] J. Chen, M. A. Reed, A. M. Rawlett, and J. M. Tour, Science **286**, 1550–1552 (1999).

[7] H. B. Akkerman, P. W. M. Blom, D. M. de Leeuw, and B. de Boer, Nature **441**, 69–72 (2006).

[8] M. A. Rampi and G. M. Whitesides, Chemical Physics **281**, 373–391 (2002).

[9] R. C. Chiechi, E. A. Weiss, M. D. Dickey, and G. M. Whitesides, Angewandte Chemie International Edition **47**, 142–144 (2008).

[10] H. Park, A. K. L. Lim, A. P. Alivisatos, J. Park, and P. L. McEuen, Applied Physics Letters **75**, 301–303 (1999).

[11] B. Xu and N. J. Tao, Science **301**, 1221–1223 (2003).

[12] M. Elbing, R. Ochs, M. Koentopp, M. Fischer, C. von Hänisch, F. Weigend, F. Evers, H. B. Weber, and M. Mayor, Proceedings of the National Academy of Sciences **102**, 8815–8820 (2005).

[13] I. Díez-Pérez, J. Hihath, Y. Lee, L. Yu, L. Adamska, M. A. Kozhushner, I. I. Oleynik, and N. Tao, Nature Chemistry **1**, 635–641 (2009).

[14] A. Batra, P. Darancet, Q. Chen, J. S. Meisner, J. R. Widawsky, J. B. Neaton, C. Nuckolls, and L. Venkataraman, Nano Letters **13**, 6233–6237 (2013).

[15] B. Capozzi, J. Xia, O. Adak, E. J. Dell, Z. F. Liu, J. C. Taylor, J. B. Neaton, L. M. Campos, and L. Venkataraman, Nature Nanotechnology **10**, 522–527 (2015).

[16] M. L. Perrin, E. Galán, R. Eelkema, J. M. Thijssen, F. Grozema, and H. S. J. van der Zant, Nanoscale **8**, 8919–8923 (2016).

[17] E. S. Tam, J. J. Parks, W. W. Shum, Y. W. Zhong, M. B. Santiago-Berríos, X. Zheng, W. Yang, G. K. Chan, H. D. Abruña, and D. C. Ralph, ACS Nano **5**, 5115–5123 (2011).

[18] D. Roldan, V. Kaliginedi, S. Cobo, V. Kolivoska, C. Bucher, W. Hong, G. Royal, and T. Wandlowski, Journal of the American Chemical Society **135**, 5974–5977 (2013).

[19] N. Darwish, A. C. Aragonès, T. Darwish, S. Ciampi, and I. Díez-Pérez, Nano Letters **14**, 7064–7070 (2014).

[20] N. Darwish, I. Díez-Pérez, P. Da Silva, N. Tao, J. J. Gooding, and Paddon-Row, Angewandte Chemie International Edition **51**, 3203–3206 (2012).

[21] M. Baghernejad, X. Zhao, K. Baruël Ørnsø, M. Füeg, P. Moreno-García, A. V. Rudnev, V. Kaliginedi, S. Vesztergom, C. Huang, W. Hong, P. Broekmann, T. Wandlowski, K. S. Thygesen, and M. R. Bryce, Journal of the American Chemical Society **136**, 17922–17925 (2014).

[22] Y. Li, M. Baghernejad, A.-G. Qusiy, D. Zsolt Manrique, G. Zhang, J. Hamill, Y. Fu, P. Broekmann, W. Hong, T. Wandlowski, D. Zhang, and C. Lambert, Angewandte Chemie **127**, 13790–13793 (2015).

[23] F. Schwarz, G. Kastlunger, F. Lissel, C. Egler-Lucas, S. N. Semenov, K. Venkatesan, H. Berke, R. Stadler, and E. Lörtscher, Nature Nanotechnology **11**, 170–176 (2016).

[24] B. E. Tebikachew, H. B. Li, A. Pirrotta, K. Börjesson, G. C. Solomon, J. Hihath, and K. Moth-Poulsen, Journal of Physical Chemistry C **121**, 7094–7100 (2017).

[25] M. Tsutsui, S. Rahong, Y. Iizumi, T. Okazaki, M. Taniguchi, and T. Kawai, Scientific Reports **1**, 46 (2011).

[26] G. Czap, P. J. Wagner, F. Xue, L. Gu, J. Li, J. Yao, R. Wu, and W. Ho, Science **364**, 670–673 (2019).

[27] Y. Hu, X. Zhuang, L. Lin, J. Liu, Z. Yao, Z. Xiao, J. Shi, B. Fang, and W. Hong, ACS Sensors **6**, 461–469 (2021).

[28] J. Park, A. N. Pasupathy, J. I. Goldsmith, C. Chang, Y. Yaish, J. R. Petta, M. Rinkoski, J. P. Sethna, H. D. Abruña, P. L. McEuen, and D. C. Ralph, Nature **417**, 722–725 (2002).

[29] S. Kubatkin, A. Danilov, M. Hjort, J. Cornil, J.-L. Brédas, N. Stuhr-Hansen, P. Hedegård, and T. Bjørnholm, Nature **425**, 698–701 (2003).

[30] M. Kiguchi, H. Nakamura, Y. Takahashi, T. Takahashi, and T. Ohto, Journal of Physical Chemistry C **114**, 22254–22261 (2010).

[31] C. M. Guédon, H. Valkenier, T. Markussen, K. S. Thygesen, J. C. Hummelen, and S. J. Van Der Molen, Nature Nanotechnology **7**, 305–309 (2012).

[32] C. R. Arroyo, R. Frisenda, K. Moth-Poulsen, J. S. Seldenthuis, T. Bjørnholm, and H. S. J. van der Zant, Nanoscale Research Letters **8**, 1–6 (2013).

[33] H. Jeong, A. M. Chang, and M. R. Melloch, Science **293**, 2221–2223 (2001).

[34] R. Frisenda, G. D. Harzmann, J. A. Celis Gil, J. M. Thijssen, M. Mayor, and H. S. J. Van Der Zant, Nano Letters **16**, 4733–4737 (2016).

[35] J. de Bruijckere, P. Gehring, M. Palacios-Corella, M. Clemente-León, E. Coronado, J. Paaske, P. Hedegård, and H. S. J. van der Zant, Physical Review Letters **122**, 197701 (2019).

[36] J. R. Widawsky, P. Darancet, J. B. Neaton, and L. Venkataraman, Nano Letters **12**, 354–358 (2012).

[37] C. Evangeli, K. Gillemot, E. Leary, M. T. González, G. Rubio-Bollinger, C. J. Lambert, and N. Agraït, Nano Letters **13**, 2141–2145 (2013).

[38] P. Gehring, J. K. Sowa, C. Hsu, J. de Bruijckere, M. van der Star, J. J. Le Roy, L. Bogani, E. M. Gauger, and H. S. J. van der Zant, Nature Nanotechnology **16**, 426–430 (2021).

[39] S. J. van der Molen and P. Liljeroth, Journal of Physics: Condensed Matter **22**, 133001 (2010).

[40] D. Xiang, X. Wang, C. Jia, T. Lee, and X. Guo, Chemical Reviews **116**, 4318–4440 (2016).

[41] P. Gehring, J. M. Thijssen, and H. S. J. van der Zant, Nature Reviews Physics **1**, 381–396 (2019).

[42] G. Ke, C. Duan, F. Huang, and X. Guo, InfoMat **2**, 92–112 (2020).

[43] H. Fu, X. Zhu, P. Li, M. Li, L. Yang, C. Jia, and X. Guo, Journal of Materials Chemistry C **10**, 2375–2389 (2022).

[44] J. C. Cuevas and E. Scheer, *Molecular electronics: an introduction to theory and experiment* (World Scientific, 2010).

[45] T. A. Su, M. Neupane, M. L. Steigerwald, L. Venkataraman, and C. Nuckolls, Nature Reviews Materials **1**, 16002 (2016).

[46] A. I. Yanson, G. Rubio Bollinger, H. E. Van Den Brom, N. Agraït, and J. M. van Ruitenbeek, Nature **395**, 783–785 (1998).

[47] C. A. Martin, D. Ding, H. S. J. van Der Zant, and J. M. van Ruitenbeek, New Journal of Physics **10**, 065008 (2008).

[48] H. Valkenier, E. H. Huisman, P. A. Van Hal, D. M. De Leeuw, R. C. Chiechi, and J. C. Hummelen, Journal of the American Chemical Society **133**, 4930–4939 (2011).

[49] E. Gorenskaia, K. L. Turner, S. Martín, P. Cea, and P. J. Low, Nanoscale **13**, 9055–9074 (2021).

[50] N. W. Ashcroft and N. D. Mermin, *Solid state physics* (Cengage Learning, 2022).

[51] B. I. Lundqvist, O. Gunnarsson, H. Hjelmberg, and J. K. Nørskov, Surface Science **89**, 196–225 (1979).

[52] R. Landauer, IBM Journal of Research and Development **1**, 223–231 (1957).

[53] Y. Imry and R. Landauer, Reviews of Modern Physics **71**, S306 (1999).

[54] J. Ferrer, C. J. Lambert, V. M. García-Suárez, D. Z. Manrique, D. Visontai, L. Oroszlany, R. Rodríguez-Ferradás, I. Grace, S. W. Bailey, K. Gillemot, H. Sadeghi, and L. A. Algharagholy, New Journal of Physics **16**, 093029 (2014).

[55] I. Bâldea, Journal of the American Chemical Society **134**, 7958–7962 (2012).

[56] I. Bâldea, Physical Review B - Condensed Matter and Materials Physics **85**, 035442 (2012).

[57] R. Frisenda, S. Tarkuç, E. Galán, M. L. Perrin, R. Eelkema, F. C. Grozema, and H. S. J. van der Zant, Beilstein Journal of Nanotechnology **6**, 1558–1567 (2015).

[58] C. J. Lambert, Chemical Society Reviews **44**, 875–888 (2015).

[59] R. Huber, M. T. González, S. Wu, M. Langer, S. Grunder, V. Horhoiu, M. Mayor, M. R. Bryce, C. Wang, R. Jitchati, C. Schönenberger, and M. Calame, Journal of the American Chemical Society **130**, 1080–1084 (2008).

[60] P. D. Williams and M. G. Reuter, Journal of Physical Chemistry C **117**, 5937–5942 (2013).

[61] R. Quan, C. S. Pitler, M. A. Ratner, and M. G. Reuter, ACS Nano **9**, 7704–7713 (2015).

[62] K. P. Hoxha and M. G. Reuter, Applied Physics Letters **117**, 136101 (2020).

[63] Z. J. Donhauser, B. A. Mantooth, K. F. Kelly, L. A. Bumm, J. D. Monnell, J. J. Stapleton, J. Price, A. M. Rawlett, D. L. Allara, J. M. Tour, and P. S. Weiss, Science **292**, 2303–2307 (2001).

[64] G. K. Ramachandran, T. J. Hopson, A. M. Rawtett, L. A. Nagahara, A. Primak, and S. M. Lindsay, Science **300**, 1413–1416 (2003).

[65] R. A. Wassel, R. R. Fuierer, N. Kim, and C. B. Gorman, Nano Letters **3**, 1617–1620 (2003).

[66] H. Basch, R. Cohen, and M. A. Ratner, Nano Letters **5**, 1668–1675 (2005).

[67] X. Li, J. He, J. Hihath, B. Xu, S. M. Lindsay, and N. Tao, Journal of the American Chemical Society **128**, 2135–2141 (2006).

[68] F. Chen, X. Li, J. Hihath, Z. Huang, and N. Tao, Journal of the American Chemical Society **128**, 15874–15881 (2006).

[69] J. Ulrich, D. Esrail, W. Pontius, L. Venkataraman, D. Millar, and L. H. Doerrer, Journal of Physical Chemistry B **110**, 2462–2466 (2006).

[70] E. Lörtscher, H. B. Weber, and H. Riel, Physical Review Letters **98**, 176807 (2007).

[71] C. Li, I. Pobelov, T. Wandlowski, A. Bagrets, A. Arnold, and F. Evers, Journal of the American Chemical Society **130**, 318–326 (2008).

[72] M. Paulsson, C. Krag, T. Frederiksen, and M. Brandbyge, Nano Letters **9**, 117–121 (2009).

[73] W. Hong, D. Z. Manrique, P. Moreno-García, M. Gulcur, A. Mishchenko, C. J. Lambert, M. R. Bryce, and T. Wandlowski, Journal of the American Chemical Society **134**, 2292–2304 (2012).

[74] P. Moreno-García, M. Gulcur, D. Z. Manrique, T. Pope, W. Hong, V. Kaliginedi, C. Huang, A. S. Batsanov, M. R. Bryce, C. Lambert, and T. Wandlowski, Journal of the American Chemical Society **135**, 12228–12240 (2013).

[75] W. R. French, C. R. Iacovella, and P. T. Cummings, ACS Nano **6**, 2779–2789 (2012).

[76] W. R. French, C. R. Iacovella, I. Rungger, A. M. Souza, S. Sanvito, and P. T. Cummings, The Journal of Physical Chemistry Letters **4**, 887–891 (2013).

[77] H. Wang and Y. Leng, The Journal of Physical Chemistry C **119**, 15216–15223 (2015).

[78] L. Mejía, N. Renaud, and I. Franco, The Journal of Physical Chemistry Letters **9**, 745–750 (2018).

[79] Z. Li and I. Franco, The Journal of Physical Chemistry C **123**, 9693–9701 (2019).

[80] Z. Li, L. Mejía, J. Marrs, H. Jeong, J. Hihath, and I. Franco, Journal of Physical Chemistry C **125**, 3406–3414 (2021).

[81] S. Wu, M. T. González, R. Huber, S. Grunder, M. Mayor, C. Schönenberger, and M. Calame, Nature Nanotechnology **3**, 569–574 (2008).

[82] R. Frisenda, V. A. Janssen, F. C. Grozema, H. S. J. Van Der Zant, and N. Renaud, Nature Chemistry **8**, 1099–1104 (2016).

[83] Y. Tang, Y. Zhou, D. Zhou, Y. Chen, Z. Xiao, J. Shi, J. Liu, and W. Hong, Journal of the American Chemical Society **142**, 19101–19109 (2020).

[84] O. Adak, E. Rosenthal, J. Meisner, E. F. Andrade, A. N. Pasupathy, C. Nuckolls, M. S. Hybertsen, and L. Venkataraman, Nano Letters **15**, 4143–4149 (2015).

[85] E. Leary, L. A. Zotti, D. Miguel, I. R. Márquez, L. Palomino-Ruiz, J. M. Cuerva, G. Rubio-Bollinger, M. T. González, and N. Agrait, Journal of Physical Chemistry C **122**, 3211–3218 (2018).

[86] A. Vladyka, M. L. Perrin, J. Overbeck, R. R. Ferradás, V. García-Suárez, M. Gantenbein, J. Brunner, M. Mayor, J. Ferrer, and M. Calame, Nature Communications **10**, 262 (2019).

[87] M. Lemmer, M. S. Inkpen, K. Kornysheva, N. J. Long, and T. Albrecht, Nature Communications **7**, 12922 (2016).

[88] M. El Abbassi, J. Overbeck, O. Braun, M. Calame, H. S. J. van der Zant, and M. L. Perrin, Communications Physics **4**, 1–9 (2021).

[89] D. Cabosart, M. El Abbassi, D. Stefani, R. Frisenda, M. Calame, H. S. J. Van der Zant, and M. L. Perrin, Applied Physics Letters **114**, 143102 (2019).

[90] F. H. van Veen, L. Ornago, H. S. J. van der Zant, and M. El Abbassi, The Journal of Physical Chemistry C **126**, 8801–8806 (2022).

[91] J. M. van Ruitenbeek, A. Alvarez, I. Piñeyro, C. Grahmann, P. Joyez, M. H. Devoret, D. Esteve, and C. Urbina, Review of Scientific Instruments **67**, 108–111 (1996).

[92] T. M. Mohiuddin, A. Lombardo, R. R. Nair, A. Bonetti, G. Savini, R. Jalil, N. Bonini, D. M. Basko, C. Galiotis, N. Marzari, K. S. Novoselov, A. K. Geim, and A. C. Ferrari, Physical Review B - Condensed Matter and Materials Physics **79**, 205433 (2009).

[93] S. Caneva, P. Gehring, V. M. García-Suárez, A. García-Fuente, D. Stefani, I. J. Olavarria-Contreras, J. Ferrer, C. Dekker, and H. S. J. van der Zant, Nature Nanotechnology **13**, 1126–1131 (2018).

[94] L. Wang, S. Zihlmann, A. Baumgartner, J. Overbeck, K. Watanabe, T. Taniguchi, P. Makk, and C. Schönenberger, Nano Letters **19**, 4097–4102 (2019).

[95] C. A. Martin, R. H. Smit, R. V. Egmond, H. S. J. Van Der Zant, and J. M. Van Ruitenbeek, Review of Scientific Instruments **82**, 53907 (2011).

[96] C. A. Martin, "Charge transport through single molecules in two-and three-terminal mechanical break junctions", PhD thesis (2010).

[97] M. Perrin, "Charge Transport Through Single-Molecule Junctions: Experiments and Theory", PhD thesis (2015).

[98] R. Frisenda, "OPE3: A model system for single-molecule transport", PhD thesis (2016).

[99] C. Untiedt, M. J. Caturla, M. R. Calvo, J. J. Palacios, R. C. Segers, and J. M. van Ruitenbeek, Physical Review Letters **98**, 206801 (2007).

[100] M. L. Trouwborst, E. H. Huisman, F. L. Bakker, S. J. Van Der Molen, and B. J. Van Wees, Physical Review Letters **100**, 175502 (2008).

[101] J. G. Simmons, Journal of Applied Physics **34**, 1793–1803 (1963).

[102] I. J. Olavarria-Contreras, "Single – molecule conductance measurements Correlations between chemical design and electronic properties", PhD thesis (2018).

[103] S. Martín, I. Grace, M. R. Bryce, C. Wang, R. Jitchati, A. S. Batsanov, S. J. Higgins, C. J. Lambert, and R. J. Nichols, Journal of the American Chemical Society **132**, 9157–9164 (2010).

[104] V. Kaliginedi, P. Moreno-García, H. Valkenier, W. Hong, V. M. García-Suárez, P. Buiter, J. L. Otten, J. C. Hummelen, C. J. Lambert, and T. Wandlowski, Journal of the American Chemical Society **134**, 5262–5275 (2012).

[105] M. T. González, X. Zhao, D. Z. Manrique, D. Miguel, E. Leary, M. Gulcur, A. S. Batsanov, G. Rubio-Bollinger, C. J. Lambert, M. R. Bryce, and N. Agraït, The Journal of Physical Chemistry C **118**, 21655–21662 (2014).

[106] Y. Liu, L. Ornago, M. Carlotti, Y. Ai, M. El Abbassi, S. Soni, A. Asyuda, M. Zharnikov, H. S. J. Van Der Zant, and R. C. Chiechi, Journal of Physical Chemistry C **124**, 22776–22783 (2020).

[107] A. Glielmo, B. E. Husic, A. Rodriguez, C. Clementi, F. Noé, and A. Laio, Chemical Reviews **121**, 9722–9758 (2021).

[108] T. Fu, Y. Zang, Q. Zou, C. Nuckolls, and L. Venkataraman, Nano Letters **20**, 3320–3325 (2020).

[109] A. Saxena, M. Prasad, A. Gupta, N. Bharill, O. P. Patel, A. Tiwari, M. J. Er, W. Ding, and C. T. Lin, Neurocomputing **267**, 664–681 (2017).

[110] F. Huang, R. Li, G. Wang, J. Zheng, Y. Tang, J. Liu, Y. Yang, Y. Yao, J. Shi, and W. Hong, Physical Chemistry Chemical Physics **22**, 1674–1681 (2020).

[111] L. Lin, C. Tang, G. Dong, Z. Chen, Z. Pan, J. Liu, Y. Yang, J. Shi, R. Ji, and W. Hong, Journal of Physical Chemistry C **125**, 3623–3630 (2021).

[112] R. W. Hamming, Bell System Technical Journal **29**, 147–160 (1950).

[113] G. Hamerly and C. Elkan, in Proceeding of the international conference on information and knowledge management (2002), pp. 600–607.

[114] D. Lam and D. C. Wunsch, "Clustering", in *Academic press library in signal processing: volume 1: signal processing theory and machine learning*, Vol. 1 (Elsevier, Jan. 2014) Chap. 20, pp. 1115–1149.

[115] D. Arthur and S. Vassilvitskii, in Proceedings of the annual acm-siam symposium on discrete algorithms (2007), pp. 1027–1035.

[116] O. Arbelaitz, I. Gurrutxaga, J. Muguerza, J. M. Pérez, and I. Perona, Pattern Recognition **46**, 243–256 (2013).

[117] B. Gotsmann, H. Riel, and E. Lörtscher, Physical Review B - Condensed Matter and Materials Physics **84**, 205408 (2011).

[118] R. Frisenda, D. Stefani, and H. S. J. Van Der Zant, Accounts of Chemical Research **51**, 1359–1367 (2018).

[119] A. Magyarkuti, N. Balogh, Z. Balogh, L. Venkataraman, and A. Halbritter, Nanoscale **12**, 8355–8363 (2020).

[120] D. Lin, Z. Zhao, H. Pan, S. Li, Y. Wang, D. Wang, S. Sanvito, and S. Hou, ChemPhysChem **22**, 2107–2114 (2021).

[121] F. H. van Veen, "Machine Learning for Single- Molecule Experiments", MSc thesis (Delft University of Technology, 2021).

[122] P. Horowitz and H. Winfield, *The Art of Electronics*, Third Edit (Cambridge University Press, New York, 2015).

[123] G. Mészáros, C. Li, I. Pobelov, and T. Wandlowski, Nanotechnology **18**, 424004 (2007).

[124] H. Liu, Z. Zhao, X. Zhao, M. Wang, T. Zhao, and D. Xiang, AIP Advances **12**, 075307 (2022).

[125] Z. Huang, F. Chen, P. A. Bennett, and N. Tao, Journal of the American Chemical Society **129**, 13225–13231 (2007).

[126] M. Tsutsui, K. Shoji, K. Morimoto, M. Taniguchi, and T. Kawai, Applied Physics Letters **92**, 223110 (2008).

[127] V. Fatemi, M. Kamenetska, J. B. Neaton, and L. Venkataraman, Nano Letters **11**, 1988–1992 (2011).

[128] D. C. Milan, O. A. Al-Owaedi, M. C. Oerthel, S. Marqués-González, R. J. Brooke, M. R. Bryce, P. Cea, J. Ferrer, S. J. Higgins, C. J. Lambert, P. J. Low, D. Z. Manrique, S. Martin, R. J. Nichols, W. Schwarzacher, and V. M. García-Suárez, Journal of Physical Chemistry C **120**, 15666–15674 (2016).

[129] Z. Tang, S. Hou, Q. Wu, Z. Tan, J. Zheng, R. Li, J. Liu, Y. Yang, H. Sadeghi, J. Shi, I. Grace, C. J. Lambert, and W. Hong, Science Bulletin **65**, 944–950 (2020).

[130] M. Baghernejad, D. Zsolt Manrique, C. Li, T. Pope, U. Zhumaev, I. Pobelov, P. Moreno-García, V. Kaliginedi, C. Huang, W. Hong, C. Lambert, and T. Wandlowski, Chemical Communications **50**, 15975–15978 (2014).

[131] B. Huang, X. Liu, Y. Yuan, Z. W. Hong, J. F. Zheng, L. Q. Pei, Y. Shao, J. F. Li, X. S. Zhou, J. Z. Chen, S. Jin, and B. W. Mao, Journal of the American Chemical Society **140**, 17685–17690 (2018).

[132] J. Bai, A. Daaoub, S. Sangtarash, X. Li, Y. Tang, Q. Zou, H. Sadeghi, S. Liu, X. Huang, Z. Tan, J. Liu, Y. Yang, J. Shi, G. Mészáros, W. Chen, C. Lambert, and W. Hong, Nature Materials **18**, 364–369 (2019).

[133] I. V. Pobelov, Z. Li, and T. Wandlowski, Journal of the American Chemical Society **130**, 16045–16054 (2008).

[134] C. Li, V. Stepanenko, M. J. Lin, W. Hong, F. Würthner, and T. Wandlowski, Physica Status Solidi (B) Basic Research **250**, 2458–2467 (2013).

[135] N. Muthusubramanian, E. Galan, C. Maity, R. Eelkema, F. C. Grozema, and H. S. J. van der Zant, Applied Physics Letters **109**, 013102 (2016).

[136] S. Joshi, A. Savov, S. Shafqat, and R. Dekker, Materials Science in Semiconductor Processing **75**, 130–135 (2018).

[137] V. Lowalekar and S. Raghavan, Journal of Materials Research **19**, 1149–1156 (2004).

[138] P. Pedeferri, "Pourbaix Diagrams", in *Engineering materials* (Springer Science and Business Media B.V., 2018), pp. 57–72.

[139] D. Vogel, L. Ornago, C. Wegeberg, A. Prescimone, H. S. J. van der Zant, and M. Mayor, Organic Materials **4**, 102–126 (2022).

[140] C. Joachim, J. K. Gimzewski, and A. Aviram, Nature **408**, 541–548 (2000).

[141] A. Vilan, D. Aswal, and D. Cahen, Chemical Reviews **117**, 4248–4286 (2017).

[142] S. V. Aradhya and L. Venkataraman, Nature Nanotechnology **8**, 399–410 (2013).

[143] S. Casalini, C. A. Bortolotti, F. Leonardi, and F. Biscarini, Chemical Society Reviews **46**, 40–71 (2017).

[144] D. Deutsch, A. Natan, Y. Shapira, and L. Kronik, Journal of the American Chemical Society **129**, 2989–2997 (2007).

[145] Y. Selzer, L. Cai, M. A. Cabassi, Y. Yao, J. M. Tour, T. S. Mayer, and D. L. Allara, Nano Letters **5**, 61–65 (2005).

[146] Q. Lu, K. Liu, H. Zhang, Z. Du, X. Wang, and F. Wang, ACS Nano **3**, 3861–3868 (2009).

[147] C. J. Querebillo, A. Terfort, D. L. Allara, and M. Zharnikov, Journal of Physical Chemistry C **117**, 25556–25561 (2013).

[148] R. Frisenda, M. L. Perrin, H. Valkenier, J. C. Hummelen, and H. S. J. Van der Zant, Physica Status Solidi (B) Basic Research **250**, 2431–2436 (2013).

[149] M. Carlotti, A. Kovalchuk, T. Wächter, X. Qiu, M. Zharnikov, and R. C. Chiechi, Nature Communications **7**, 1–7 (2016).

[150] D. Fracasso, H. Valkenier, J. C. Hummelen, G. C. Solomon, and R. C. Chiechi, Journal of the American Chemical Society **133**, 9556–9563 (2011).

[151] L. Qiu, Y. Zhang, T. L. Krijger, X. Qiu, P. v. t. Hof, J. C. Hummelen, and R. C. Chiechi, Chemical Science **8**, 2365–2372 (2017).

[152] A. Nefedov and C. Wöll, Springer Series in Surface Sciences **51**, 277–303 (2013).

[153] F. Schreiber, Progress in Surface Science **65**, 151–257 (2000).

[154] F. Neese, Wiley Interdisciplinary Reviews: Computational Molecular Science **2**, 73–78 (2012).

[155] F. Neese, Wiley Interdisciplinary Reviews: Computational Molecular Science **8**, e1327 (2018).

[156] C. Herrmann, G. C. Solomon, J. E. Subotnik, V. Mujica, and M. A. Ratner, The Journal of Chemical Physics **132**, 024103 (2010).

[157] M. Deffner, L. Groß, T. Steenbock, B. A. Voigt, G. C. Solomon, C. Herrmann, *ARTAIOS — a code for postprocessing quantum chemical electronic structure calculations*, 2008-2017.

[158] N. Nijegorodov, V. Ramachandran, and D. P. Winkoun, Spectrochimica Acta - Part A: Molecular and Biomolecular Spectroscopy **53**, 1813–1824 (1997).

[159] B. Shen, J. Tatchen, E. Sanchez-Garcia, and H. F. Bettinger, Angewandte Chemie **130**, 10666–10669 (2018).

[160] N. Nerngchamnong, L. Yuan, D. C. Qi, J. Li, D. Thompson, and C. A. Nijhuis, Nature Nanotechnology **8**, 113–118 (2013).

[161] A. Kovalchuk, T. Abu-Husein, D. Fracasso, D. A. Egger, E. Zojer, M. Zharnikov, A. Terfort, and R. C. Chiechi, Chemical Science **7**, 781–787 (2015).

[162] T. Abu-Husein, S. Schuster, D. A. Egger, M. Kind, T. Santowski, A. Wiesner, R. Chiechi, E. Zojer, A. Terfort, and M. Zharnikov, Advanced Functional Materials **25**, 3943–3957 (2015).

[163] M. Carlotti, S. Soni, X. Qiu, E. Sauter, M. Zharnikov, and R. C. Chiechi, Nanoscale Advances **1**, 2018–2028 (2019).

[164] G. te Velde, F. M. Bickelhaupt, E. J. Baerends, C. Fonseca Guerra, S. J. A. van Gisbergen, J. G. Snijders, and T. Ziegler, Journal of Computational Chemistry **22**, 931–967 (2001).

[165] *ADF 2019.3, SCM, Theoretical Chemistry, Vrije Universiteit, Amsterdam, The Netherlands, http://www.scm.com*, 2019.

[166] G. Te Velde and E. J. Baerends, Physical Review B **44**, 7888–7903 (1991).

[167] *BAND 2019.3, SCM, Theoretical Chemistry, Vrije Universiteit, Amsterdam, The Netherlands, http://www.scm.com*, 2019.

[168] E. A. Weiss, R. C. Chiechi, G. K. Kaufman, J. K. Kriebel, Z. Li, M. Duati, M. A. Rampi, and G. M. Whitesides, Journal of the American Chemical Society **129**, 4336–4349 (2007).

[169] P. Pourhossein, R. K. Vijayaraghavan, S. C. Meskers, and R. C. Chiechi, Nature Communications **7**, 1–9 (2016).

[170] M. Carlotti, S. Soni, S. Kumar, Y. Ai, E. Sauter, M. Zharnikov, and R. C. Chiechi, Angewandte Chemie - International Edition **57**, 15681–15685 (2018).

[171] D. Xiang, H. Jeong, T. Lee, D. Mayer, D. Xiang, H. Jeong, T. Lee, and D. Mayer, Advanced Materials **25**, 4845–4867 (2013).

[172] D. Stefani, K. J. Weiland, M. Skripnik, C. Hsu, M. L. Perrin, M. Mayor, F. Pauly, and H. S. J. Van Der Zant, Nano Letters **18**, 5981–5988 (2018).

[173] I. L. Herrer, A. K. Ismael, D. C. Milán, A. Vezzoli, S. Martín, A. González-Orive, I. Grace, C. Lambert, J. L. Serrano, R. J. Nichols, and P. Cea, The Journal of Physical Chemistry Letters **9**, 5364–5372 (2018).

[174] K. Qu, P. Duan, J.-Y. Wang, B. Zhang, Q.-C. Zhang, W. Hong, and Z.-N. Chen, Nano Letters **21**, 9729–9735 (2021).

[175] M. T. González, A. Díaz, E. Leary, R. García, M. Á. Herranz, G. Rubio-Bollinger, N. Martín, and N. Agraït, Journal of the American Chemical Society **135**, 5420–5426 (2013).

[176] H. Chen, Y. Li, and S. Chang, Analytical Chemistry **92**, 6423–6429 (2020).

[177] M. Mayor, H. B. Weber, J. Reichert, M. Elbing, C. Von Hänisch, D. Beckmann, and M. Fischer, Angewandte Chemie - International Edition **42**, 5834–5838 (2003).

[178] M. T. González, E. Leary, R. García, P. Verma, M. Á. Herranz, G. Rubio-Bollinger, N. Martín, and N. Agraït, Journal of Physical Chemistry C **115**, 17973–17978 (2011).

[179] L. Venkataraman, J. E. Klare, I. W. Tam, C. Nuckolls, M. S. Hybertsen, and M. L. Steigerwald, Nano Letters **6**, 458–462 (2006).

[180] Y. S. Park, A. C. Whalley, M. Kamenetska, M. L. Steigerwald, M. S. Hybertsen, C. Nuckolls, and L. Venkataraman, Journal of the American Chemical Society **129**, 15768–15769 (2007).

[181] L. Bartels, G. Meyer, K.-H. Rieder, D. Velic, E. Knoesel, A. Hotzel, M. Wolf, and G. Ertl, Physical Review Letters **80**, 2004–2007 (1998).

[182] T. Fu, K. Frommer, C. Nuckolls, and L. Venkataraman, Journal of Physical Chemistry Letters **12**, 10802–10807 (2021).

[183] G. E. Poirier, Chemical Reviews **97**, 1117–1127 (1997).

[184] M. Tachibana, K. Yoshizawa, A. Ogawa, H. Fujimoto, and R. Hoffmann, Journal of Physical Chemistry B **106**, 12727–12736 (2002).

[185] L. Ornago, J. Kamer, M. El Abbassi, F. C. Grozema, and H. S. J. van der Zant, The Journal of Physical Chemistry C **126**, 19843–19848 (2022).

[186] N. Xin, J. Guan, C. Zhou, X. Chen, C. Gu, Y. Li, M. A. Ratner, A. Nitzan, J. F. Stoddart, and X. Guo, Nature Reviews Physics **1**, 211–230 (2019).

[187] J. Roncali, Macromolecular Rapid Communications **28**, 1761–1775 (2007).

[188] H. Bronstein, C. B. Nielsen, B. C. Schroeder, and I. McCulloch, Nature Reviews Chemistry **4**, 66–77 (2020).

[189] X. Zhao, C. Huang, M. Gulcur, A. S. Batsanov, M. Baghernejad, W. Hong, M. R. Bryce, and T. Wandlowski, Chemistry of Materials **25**, 4340–4347 (2013).

[190] H. Dekkiche, A. Gemma, F. Tabatabaei, A. S. Batsanov, T. Niehaus, B. Gotsmann, and M. R. Bryce, Nanoscale **12**, 18908–18917 (2020).

[191] A. Mishchenko, D. Vonlanthen, V. Meded, M. Bürkle, C. Li, I. V. Pobelov, A. Bagrets, J. K. Viljas, F. Pauly, F. Evers, M. Mayor, and T. Wandlowski, Nano Letters **10**, 156–163 (2010).

[192] W. Jiang, Z. Tan, R. Almughathawi, Q. Wu, Z. Liu, J. Liu, S. Hou, G. Zhang, C. J. Lambert, W. Hong, and D. Zhang, ChemPhysChem **22**, 2573–2578 (2021).

[193] J. Alqahtani, H. Sadeghi, S. Sangtarash, C. J. Lambert, J. Alqahtani, D. H. Sadeghi, D. Sangtarash, and P. C. rof J Lambert, Angewandte Chemie International Edition **57**, 15065–15069 (2018).

[194] C. Tang, L. Huang, S. Sangtarash, M. Noori, H. Sadeghi, H. Xia, and W. Hong, Journal of the American Chemical Society **143**, 9385–9392 (2021).

[195] L. Venkataraman, Y. S. Park, A. C. Whalley, C. Nuckolls, M. S. Hybertsen, and M. L. Steigerwald, Nano Letters **7**, 502–506 (2007).

[196] L. J. O'Driscoll and M. R. Bryce, Nanoscale **13**, 10668–10711 (2021).

[197] S. Sangtarash, A. Vezzoli, H. Sadeghi, N. Ferri, H. M. O'Brien, I. Grace, L. Bouffier, S. J. Higgins, R. J. Nichols, and C. J. Lambert, Nanoscale **10**, 3060–3067 (2018).

[198] A. Daaoub, L. Ornago, D. Vogel, P. Bastante, S. Sangtarash, M. Parmeggiani, J. Kamer, N. Agraït, M. Mayor, H. S. J. van der Zant, and H. Sadeghi, The Journal of Physical Chemistry Letters **13**, 9156–9164 (2022).

[199] J. M. Seminario, A. G. Zacarias, and J. M. Tour, Journal of the American Chemical Society **122**, 3015–3020 (2000).

[200] L. J. Sham and M. Schlüter, Physical Review Letters **51**, 1888–1891 (1983).

[201] H. Sadeghi, Nanotechnology **29**, 373001 (2018).

[202] I. S. Kristensen, D. J. Mowbray, K. S. Thygesen, and K. W. Jacobsen, Journal of Physics: Condensed Matter **20**, 374101 (2008).

[203] K. Yoshida, I. V. Pobelov, D. Z. Manrique, T. Pope, G. Mészáros, M. Gulcur, M. R. Bryce, C. J. Lambert, and T. Wandlowski, Scientific Reports **5**, 9002 (2015).

[204] V. B. Engelkes, J. M. Beebe, and C. D. Frisbie, Journal of Physical Chemistry B **109**, 16801–16810 (2005).

[205] S. Y. Jang, P. Reddy, A. Majumdar, and R. A. Segalman, Nano Letters **6**, 2362–2367 (2006).

[206] S. Y. Quek, L. Venkataraman, H. J. Choi, S. G. Louie, M. S. Hybertsen, and J. B. Neaton, Nano Letters **7**, 3477–3482 (2007).

[207] H. Sadeghi, Journal of Physical Chemistry C **123**, 12556–12562 (2019).

[208] L. Rincón-García, C. Evangeli, G. Rubio-Bollinger, and N. Agraït, Chemical Society Reviews **45**, 4285–4306 (2016).

[209] Z. Chen, L. Chen, J. Liu, R. Li, C. Tang, Y. Hua, L. Chen, J. Shi, Y. Yang, J. Liu, J. Zheng, L. Chen, J. Cao, H. Chen, H. Xia, and W. Hong, Journal of Physical Chemistry Letters, 3453–3458 (2019).

[210] C. H. Hendon, D. Tiana, A. T. Murray, D. R. Carbery, and A. Walsh, Chemical Science **4**, 4278–4284 (2013).

[211] M. H. Garner, W. Bro-Jørgensen, and G. C. Solomon, Journal of Physical Chemistry C **124**, 18968–18982 (2020).

[212] S. Menning, M. Krämer, A. Duckworth, F. Rominger, A. Beeby, A. Dreuw, and U. H. Bunz, Journal of Organic Chemistry **79**, 6571–6578 (2014).

[213] Y. Kozhemyakin, M. Krämer, F. Rominger, A. Dreuw, and U. H. Bunz, Chemistry – A European Journal **24**, 15219–15222 (2018).

[214] E. H. Huisman, C. M. Guédon, B. J. van Wees, and S. J. van Der Molen, Nano Letters **9**, 3909–3913 (2009).

[215] Y. Yang, J. Liu, S. Feng, H. Wen, J. Tian, J. Zheng, B. Schöllhorn, C. Amatore, Z. Chen, and Z. Tian, Nano Research **9**, 560–570 (2016).

[216] Z. Xie, I. Baldea, and C. D. Frisbie, Journal of the American Chemical Society **141**, 18182–18192 (2019).

[217] Y. Zang, Q. Zou, T. Fu, F. Ng, B. Fowler, J. Yang, H. Li, M. L. Steigerwald, C. Nuckolls, and L. Venkataraman, Nature Communications **10**, 4482 (2019).

[218] H. B. Li, B. E. Tebikachew, C. Wiberg, K. Moth-Poulsen, and J. Hihath, Angewandte Chemie - International Edition **59**, 11738–11743 (2020).

[219] Y. Zang, E. D. Fung, T. Fu, S. Ray, M. H. Garner, A. Borges, M. L. Steigerwald, S. Patil, G. Solomon, and L. Venkataraman, Nano Letters **21**, 673–679 (2021).

[220] T. Gao, Z. Pan, Z. Cai, J. Zheng, C. Tang, S. Yuan, S. qiang Zhao, H. Bai, Y. Yang, J. Shi, Z. Xiao, J. Liu, and W. Hong, Chemical Communications **57**, 7160–7163 (2021).

[221] H. Zhang, W. Xu, K. Song, T. Lu, G. Zhang, Y. Zang, W. Hong, and D. Zhang, Advanced Science **9**, 2105667 (2022).

[222] S. Kayashima, K. Takahashi, M. Motoyama, and J. I. Shirakashi, Japanese Journal of Applied Physics, Part 2: Letters **46**, L907 (2007).

[223] J. Liu, X. Huang, F. Wang, and W. Hong, Accounts of Chemical Research **52**, 151–160 (2019).

[224] P. Sautet and C. Joachim, Chemical Physics Letters **153**, 511–516 (1988).

[225] M. Magoga and C. Joachim, Physical Review B **59**, 16011 (1999).

[226] C. R. Arroyo, S. Tarkuc, R. Frisenda, J. S. Seldenthuis, C. H. Woerde, R. Eelkema, F. C. Grozema, and H. S. J. Van Der Zant, Angewandte Chemie - International Edition **52**, 3152–3155 (2013).

[227] G. Yang, H. Wu, J. Wei, J. Zheng, Z. Chen, J. Liu, J. Shi, Y. Yang, and W. Hong, Chinese Chemical Letters **29**, 147–150 (2018).

[228] T. Markussen, R. Stadler, and K. S. Thygesen, Nano Letters **10**, 4260–4265 (2010).

[229] W. Hong, H. Valkenier, G. Mészáros, D. Z. Manrique, A. Mishchenko, A. Putz, P. M. García, C. J. Lambert, J. C. Hummelen, and T. Wandlowski, Beilstein Journal of Nanotechnology 2:76 **2**, 699–713 (2011).

[230] H. Valkenier, C. M. Guédon, T. Markussen, K. S. Thygesen, S. J. van der Molen, and J. C. Hummelen, Phys. Chem. Chem. Phys. **16**, 653–662 (2014).

[231] M. Koole, J. M. Thijssen, H. Valkenier, J. C. Hummelen, and H. S. D. Zant, Nano Letters **15**, 5569–5573 (2015).

[232] W. Chen, H. Li, J. R. Widawsky, C. Appayee, L. Venkataraman, and R. Breslow, Journal of the American Chemical Society **136**, 918–920 (2014).

[233] D. Miguel, L. Álvarez De Cienfuegos, A. Martín-Lasanta, S. P. Morcillo, L. A. Zotti, E. Leary, M. Bürkle, Y. Asai, R. Jurado, D. J. Cárdenas, G. Rubio-Bollinger, N. Agraït, J. M. Cuerva, and M. T. González, Journal of the American Chemical Society **137**, 13818–13826 (2015).

[234] X. Liu, S. Sangtarash, D. Reber, D. Zhang, H. Sadeghi, J. Shi, Z. Y. Xiao, W. Hong, C. J. Lambert, and S. X. Liu, Angewandte Chemie - International Edition **56**, 173–176 (2017).

[235] F. Jiang, D. I. Trupp, N. Algethami, H. Zheng, W. He, A. Alqorashi, C. Zhu, C. Tang, R. Li, J. Liu, H. Sadeghi, J. Shi, R. Davidson, M. Korb, A. N. Sobolev, M. Naher, S. Sangtarash, P. J. Low, W. Hong, and C. J. Lambert, Angewandte Chemie International Edition **58**, 18987–18993 (2019).

[236] Y. Li, M. Buerkle, G. Li, A. Rostamian, H. Wang, Z. Wang, D. R. Bowler, T. Miyazaki, L. Xiang, Y. Asai, G. Zhou, and N. Tao, Nature Materials **18**, 357–363 (2019).

[237] K. Reznikova, C. Hsu, W. M. Schosser, A. Gallego, K. Beltako, F. Pauly, H. S. J. Van Der Zant, and M. Mayor, Journal of the American Chemical Society **143**, 13944–13951 (2021).

[238] H. Vazquez, R. Skouta, S. Schneebeli, M. Kamenetska, R. Breslow, L. Venkataraman, and M. S. Hybertsen, Nature Nanotechnology **7**, 663–667 (2012).

[239] H. Li, M. H. Garner, Z. Shangguan, Y. Chen, Q. Zheng, T. A. Su, M. Neupane, T. Liu, M. L. Steigerwald, F. Ng, C. Nuckolls, S. Xiao, G. C. Solomon, and L. Venkataraman, Journal of the American Chemical Society **140**, 15080–15088 (2018).

[240] B. Zhang, M. H. Garner, L. Li, L. M. Campos, G. C. Solomon, and L. Venkataraman, Chemical Science **12**, 10299–10305 (2021).

[241] P. Duan, Y. Wang, L. Chen, K. Qu, J. Liu, Q.-C. Zhang, Z.-N. Chen, W. Hong, P. Duan, Y. Wang, L. Chen, J. Liu, W. Hong, K. Qu, Q.-C. Zhang, and Z.-N. Chen, Small **18**, 2200361 (2022).

[242] H. Chen, S. Hou, Q. Wu, F. Jiang, P. Zhou, L. Zhang, Y. Jiao, B. Song, Q. H. Guo, X. Y. Chen, W. Hong, C. J. Lambert, and J. F. Stoddart, Matter **4**, 3662–3676 (2021).

[243] P. Duan, K. Qu, J. Y. Wang, B. Zeng, C. Tang, H. F. Su, Q. C. Zhang, W. Hong, and Z. N. Chen, Cell Reports Physical Science **2**, 100342 (2021).

[244] R. Miao, H. Xu, M. Skripnik, L. Cui, K. Wang, K. G. Pedersen, M. Leijnse, F. Pauly, K. Wärnmark, E. Meyhofer, P. Reddy, and H. Linke, Nano Letters **18**, 5666–5672 (2018).

[245] X. Yin, Y. Zang, L. Zhu, J. Z. Low, Z. F. Liu, J. Cui, J. B. Neaton, L. Venkataraman, and L. M. Campos, Science Advances **3**, `10.1126/sciadv.aao2615` (2017).

[246] S. Y. Quek, M. Kamenetska, M. L. Steigerwald, H. J. Choi, S. G. Louie, M. S. Hybertsen, J. B. Neaton, and L. Venkataraman, Nature Nanotechnology **4**, 230–234 (2009).

[247] T. A. Su, H. Li, M. L. Steigerwald, L. Venkataraman, and C. Nuckolls, Nature Chemistry 2015 7:3 **7**, 215–220 (2015).

[248] Y. Li, N. L. Haworth, L. Xiang, S. Ciampi, M. L. Coote, and N. Tao, Journal of the American Chemical Society **139**, 14699–14706 (2017).

[249] G. D. Scott and D. Natelson, ACS Nano **4**, 3560–3579 (2010).

[250] C. Huang, A. V. Rudnev, W. Hong, and T. Wandlowski, Chemical Society Reviews **44**, 889–901 (2015).

[251] A. Laucht, F. Hohls, N. Ubbelohde, M. Fernando Gonzalez-Zalba, D. J. Reilly, S. Stobbe, T. Schröder, P. Scarlino, J. V. Koski, A. Dzurak, C.-H. Yang, J. Yoneda, F. Kuemmeth, H. Bluhm, J. Pla, C. Hill, J. Salfi, A. Oiwa, J. T. Muhonen, E. Verhagen, M. D. LaHaye, H. H. Kim, A. W. Tsen, D. Culcer, A. Geresdi, J. A. Mol, V. Mohan, P. K. Jain, and J. Baugh, Nanotechnology **32**, 162003 (2021).

ACKNOWLEDGEMENTS

After this long scientific discussion, I would like to spend a few paragraphs to thank all the people that made this dissertation possible.

There is no doubt on the person I should thank first, **Herre**. As my promotor and supervisor you gave me the chance to start this PhD. There have been ups and downs in my quest to achieve the title of doctor. You have always been there, supporting and pushing me up the lows and cheering for each achievement (despite my tireless skill of ignoring them). You always gave me freedom in managing my time and my research, while giving me hints and ideas. I cannot believe I am writing this, but I will miss the crazy ideas and speculations you often had in the lab. Our view of the world and of science is almost opposite, and I could have not asked for anything better. Your continuous challenging my views and my statements, especially early in the PhD, helped me tremendously in growing as a researcher. For all of this, and more, I cannot thank you enough.

Next, I would like to thank my second promotor, **Ferdinand**. Your advice was crucial in some key moments of my PhD. At the end of my first year you pointed out how I was missing a "big picture" on my research plan. I treasured your advice: if this thesis has coherence and a thread flowing through it, it is also thanks to you. I would also like to thank the people that evaluated this dissertation: **Jos, Christian, Ismael, Kasper, Hatef** and **Yaroslav**. Thank you for being part of my PhD committee.

Sticking to the theme of people involved in the defence, I owe a great debt of gratitude to my paranymphs: **Damian** and **Serhii**. **Damian**, thank you for the long discussions on science, videogames and Formula 1 (and, of course, for checking the Dutch version of the abstract and the propositions). Your conceptual and heavily theoretical view of Physics is intriguing. I admire the progress you made in integrating it in the experimental world while progressing through your PhD. You are a thoughtful and careful researcher, and I wish you success in the last part of your PhD and for your work and life afterwards. **Serhii**, it was wonderful to share the office with you. You are a talented researcher, always thriving to get more and more exciting results, and never losing sight of the physical nuances. You had to face absurd challenges in addition to the PhD itself, but you managed to keep your kind heart, and I hope you will never lose it. Thank you for all the discussion, the tips, the jokes, and the occasional pool game. And thank you for being Chunwei's paranymph together with me. I hope you will be able to find serenity and satisfaction in your career and in your life. But most importantly: ask for a new SSD!

Maria and **Chunwei**, you are the closest people I had in the Netherlands, as colleagues, and as friends. **Chunwei**, I am grateful to have had you alongside me for most of the PhD. You have been the person I could always rely on for help, discussion, games, or "just" for a few words. I always admired the confidence with which you face new (research) challenges. I wish you the best in your path after the PhD and *please*, don't disappear. It does not take much effort to reply to a message every now and then. **Maria**, most of the research in this dissertation would have not been the same without your contribution.

Since the first moment I met you, you always tried to help me. As I discovered shortly thereafter, you always help everyone around you: you are one of the most altruistic people I have ever met, sometimes even too much (but I hope you now learned to care a bit more about yourself). You have been the heart and soul of the lab for the greater part of my PhD, and we all miss you since you left. Thank you for all the discussions, the coffee breaks, the social gatherings, and for keeping alive the *very important meetings*. **Alfredo**, the first member of the El Abbassi lab. It was a pleasure to meet you, to work with you and to hang out with you during the months you spent in Delft. I wish you can find all the happiness and success you deserve in the final stage of your PhD and in your life afterwards.

Many people joined and left the van der Zant lab during the time of my PhD, and I would like to thank them. **Davide**, I really appreciate you teaching me the ways of the MCBJ. I know you wish you did more, but that was already a lot of help. I gladly remember the time we spent together in and outside the lab, especially the many board games you so enthusiastically introduced me to. **Pascal**, thank you for all the scientific discussion and technical tips in the lab. I really appreciated the joyful atmosphere that you were able to create while getting a beer after work. **Joeri**, thank you for all the tips and reflections in how to start the PhD, and in what to do afterwards. **Matteo** thank you for helping me push the measurements in liquid. It didn't quite turn out at the end, but I really enjoyed the time we spent working on it together. Also, thank you for having me try climbing! **Sebastiaan**, I leave the MCBJs with you, knowing that they are in good hands. The path of molecular electronics is challenging, but I hope you will be able to navigate it without too much frustration. It was a pleasure to work together with you. I wish you the best for your future. **Jacqui**, good luck with the end of your PhD and for your projects after it. I enjoyed the occasional trips to Coffee Star. **Tristan**, I wish you success for the rest of your PhD and for your life afterwards. And good luck with the Attocube. **Maurits**, it was nice to hone our "conversational skills" together, I wish you the best for the end of your PhD, and good luck with the QN C&C. **Gabriele**, good luck with the start of your dream career. And best of luck for the final stages of the PhD to **Jasper** and **Thomas** too. **Josep**, you came to the group as a postdoc when we didn't have any. You brought refreshing new topics, that you were always eager to explain and discuss. You are a passionate and dedicated researcher, and I wish you can find the place you deserve in the scientific community. I also really appreciated your initiatives in organising the group's work. **Talieh**, thank you for the optimistic spirit you brought to the group, and for your countless attempts at building a bit of group cohesion. Your ability to establish collaborations and your hard-working spirit are admirable. Good luck with your next experience at Harvard! **Diana**, thank you for all the enthusiasm that you periodically bring to the group. I appreciated the tips and hits on how to work with the MCBJ, and all the suggestion for the measurements in liquid. Good luck with all the porphyrin projects! **Frederick**, although not under my direct supervision, it was a pleasure to have you around for your master project, the discussions with you were always exciting. You quickly mastered the ways of machine learning and developed tools that I would now consider essential for the analysis of MCBJ data. Good luck for your PhD, and don't let the Swiss get the best of you! **Michael**, your *chill* personality and mood was a windfall in the group during the months that you spent here for your master project. I wish you the best for your future and I hope our paths will meet again (You have an alternative phrasing of this last sentence, but I still find it too

awkward).

Next, I have to thank the students that I had the chance to follow during my PhD, whose work contributed to achieving this dissertation. **Jerry**, it was a pleasure to supervise you during your master end project. You are a hard working person, with admirable focus on self-improvement. Your project did not fully go as planned, for reasons outside of your control. However, you persevered and managed to obtain good results. I am sure your determination will guide you through the PhD path that you chose. I would also like to thank the Bachelor students I had the opportunity of supervising: **Tim** and **Charlotte**. You both worked very hard, and I wish you the best in the final years of your studies and beyond.

My experience at TU Delft would have not been the same without many of the people in the QN department. **Thierry**, I was lucky to have you as an office mate. Your cheerful, uplifting and inclusive spirit sweetened the harsh days at the university. Thank you for dragging me (sometimes almost literally) to Teepee or to a dinner, and for the long discussions on the most various topics. I will always remember the trip to Paris! **Ulderico**, the best meat griller in town (I still believe you lost the Euro pool on purpose to show your skills off), and the person to reveal me the truth about BCS. Thank you for bringing your jokes and your energy to QN! **Martin**, you are an unbelievably nice person. You worked incredibly hard (and for long hours too), and you always tried to help everyone. It's heartwarming to remember the moments we spent together, especially at those barbecues. I hope Germany will not scar you, and I wish you and **Sara** a great future. **Edouard**, you were my first office mate. I always appreciated the way you kept a religious silence while in the office. But outside of it, I soon discovered you were a great scientist and a very talkative person, always ready to discuss and share your opinion. I also need to thank the other people that have shared the office with me in these past few years, **Mattias** and **Patrick**. Lastly, I cannot forget the **QN C&C Committee: Sonakshi, Victoria, Maurits, Jean-Paul, Lizzy, Sonia, Gary, Maz**. Thank you for the many initiatives that you organized to lighten up the atmosphere at the department.

My research work would have not been possible without the support of the TU Delft staff. To start off, I want to thank the people at DEMO for their help with measurement electronics. In particular, I cannot understate how much **Hans** and **Berend** helped in the design and production of the PCB amplifier described in the dissertation. Next, I would like to thank the KN staff for all the help they gave me and the incredible work they do in maintaining the cleanroom: **Charles, Bas, Marco, Marc, Ewan, Roald, Eugene, Pauline, Lodi, Anja, Arnold, Hozanna and Marinus**. Special thanks to **Tino** for his help with maintaining the labs and for ordering chemicals, as well as for the occasional chat. Many thanks to **Heleen** for always being available to help with all kinds of administrative and other non-technical tasks.

During these years I received help from many people outside of the university. I would like to thank **Patrick, David** and **Marcel** at the University of Basel for all the interesting molecules they provided, and for the continuous and profound feedback that you always gave. **Shima** and **Kasper** from Chalmers University of Technology, thank you for the interesting project you brought to us, I hope it will bring many exciting results. I also need to thank the people that visited us from Madrid. **Pablo**, your many trips to Delft brought a bit of Spanish sunshine to our days. **Juan**, it was a joy to have you in Delft. Thank you

for sharing Spanish delicacies (and wine) with us!

Infine, vorrei ringraziare le tre persone che, anche se a distanza, mi hanno sempre incoraggiato durante questi quattro lunghi anni: **Mamma, Papà** e **Camilla**. Senza di voi non avrei mai completato questo manoscritto. Grazie per aver sopportato l'irritabilità, i silenzi, e i malumori a cui vi ho sottoposto durante il dottorato. E grazie per avermi dato il calore e l'amore di casa anche attraverso uno schermo. Vi voglio bene.

Curriculum Vitæ

Luca Ornago

11-04-1994 Born in Bergamo, Italy.

Education

2008-2013 High School
Istituto Superiore G. Natta
Bergamo, Italy

2013–2016 Bachelor in Materials Engineering and Nanotechnology (cum laude)
Politecnico di Milano
Milan, Italy

2016–2018 Master in Materials Engineering and Nanotechnology (cum laude)
Politecnico di Milano
Milan, Italy
Thesis: Synthesis of Tantalum-doped Titanium oxide thin films: a bridge to infrared plasmonics
Supervisor: Prof. Dr. A. Li Bassi

2019-2023 PhD in Applied Physics
Delft University of Technology
Delft, The Netherlands
Thesis: Complexity of Electron Transport in Nanoscale Molecular Junctions
Promotors: Prof. Dr. Ir. H. S. J. van der Zant
Prof. Dr. F. C. Grozema

LIST OF PUBLICATIONS

8. P. Zwick, **L. Ornago**, S. van der Poel, T. Brandl, M. El Abbassi, M. L. Perrin, D. Dulić, Herre S. J. van der Zant, and Marcel Mayor, "Alkyl Chains as Electrically Insulating Groups for Single-Molecule Junctions: A Double-Edged Sword", *in preparation*.

7. **L. Ornago**, J. Kamer, M. El Abbassi, F.C. Grozema, and H.S.J. van der Zant, "Switching in Nanoscale Molecular Junctions due to Contact Reconfiguration", The Journal of Physical Chemistry C **126**, 19843-19848 (2022).

6. A. Daaoub*, **L. Ornago***, D. Vogel*, P. Bastante*, S. Sangtarash, M. Parmeggiani, J. Kamer, N. Agraït, M. Mayor, H.S.J. van der Zant, and H. Sadeghi, "Engineering Transport Orbitals in Single-Molecule Junctions", The Journal of Physical Chemistry Letters **13**, 9156-9164 (2022).

5. D. Vogel, **L. Ornago**, C. Wegeberg, A. Prescimone, H.S.J. van der Zant, and M. Mayor, "2, 5-Diaryl 6-hydroxyphenalenones for Single-Molecule Junctions", Organic Materials **4**, 102-126 (2022).

4. F.H. van Veen, **L. Ornago**, H.S.J. van der Zant, and M. El Abbassi, "Benchmark Study of Alkane Molecular Chains", The Journal of Physical Chemistry C **126**, 8801–8806 (2022).

3. B.R. Bricchi, M. Sygletou, **L. Ornago**, G. Terraneo, F. Bisio, C. Mancarella, L. Stasi, F. Rusconi, E. Mogni, M. Ghidelli, P. Biagioni, and A. Li Bassi, "Optical and electronic properties of transparent conducting Ta:TiO_2 thin and ultra-thin films: the effect of doping and thickness", Materials Advances **2**, 7064-7076 (2021).

2. D. Stefani, C. Guo, **L. Ornago**, D. Cabosart, M. El Abbassi, M. Sheves, D. Cahen, and H.S.J. van der Zant, "Conformation-dependent charge transport through short peptides", Nanoscale **13**, 3002-3009 (2021).

1. Y. Liu, **L. Ornago**, M. Carlotti, Y. Ai, M. El Abbassi, S. Soni, A. Asyuda, M. Zharnikov, H.S.J. van der Zant, and R.C. Chiechi, "Intermolecular Effects on Tunneling through Acenes in Large-Area and Single-Molecule Junctions", The Journal of Physical Chemistry C **124**, 22776-22783 (2020).

*These authors contributed equally.